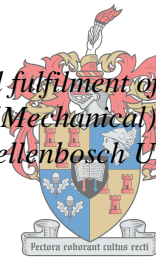


# The development, construction and testing of a piston expander for small-scale solar thermal power plants

by  
Bradley Da Silva

*Thesis presented in partial fulfilment of the requirements for the degree of Master of Engineering (Mechanical) in the Faculty of Engineering at Stellenbosch University*



UNIVERSITEIT  
iYUNIVESITHI  
STELLENBOSCH  
UNIVERSITY

100  
1918 · 2018

Supervisor: Prof Chris Meyer

March 2018

## **Declaration**

By submitting this thesis electronically, I declare that the entirety of the work contained therein is my own, original work, that I am the sole author thereof (save to the extent explicitly otherwise stated), that reproduction and publication thereof by Stellenbosch University will not infringe any third party rights and that I have not previously in its entirety or in part submitted it for obtaining any qualification.

March 2018

Copyright © 2018 Stellenbosch University

All rights reserved

## Abstract

The development of a prototype variable valve duration reciprocating steam expander was undertaken. A variable valve duration system was developed which could vary the cut-off ratio from 15 % to 90 %. An existing internal combustion engine was converted into the prototype reciprocating steam engine.

Thermodynamic models were developed to determine the theoretical power output and working fluid consumption of the manufactured prototype engine.

Proof of concept tests were performed on the engine. The engine was operated at 500 rpm where the output power and air consumption were measured. Tests were performed for various cut-off ratios to determine the influence on output power and air consumption. The experimental results showed a strong correlation to the theoretical effect of cut-off ratio on power output and air consumption.

The maximum experimental output achieved was 1.396 kW at an 80 % cut-off ratio. The experimental power output was lower than the theoretical results which neglected mechanical losses in the system. The thermodynamic model over predicted the air consumption due to the assumption of instantaneous valve events.

## Uittreksel

Die ontwikkeling van 'n prototipe veranderlike klep deur wederkerige stoom uitsitter is onderneem. 'n Veranderlike klep-duurstelsel is ontwikkel wat die afsnyverhouding van 15% tot 90% kan wissel. 'n Bestaande verbrandingsmotor was omskep as die bewys van konsep wederkerige stoom-enjin.

Termodinamiese modelle was ontwikkel om die teoretiese kraguitset en werkvloeistofverbruik van die vervaardigde prototipe-enjin te bepaal.

Bewys van konseptuële is op die enjin uitgevoer. Die enjin is teen 500 rpm bedryf en die uitlaatkrag en lugverbruik was gemeet. Toetse is uitgevoer vir verskillende afsnyverhoudings om die invloed op die uitsetkrag en lugverbruik te bepaal. Die eksperimentele resultate het 'n sterk verband getoon met die teoretiese effek van afsnyverhouding op kraguitset en lugverbruik.

Die maksimum eksperimentele uitset was 1.396 kW teen 'n afsnyverhouding van 80%. Die eksperimentele kraguitset was laer as die teoretiese resultate wat meganiese verliese in die stelsel nie in ag geneem het nie. Die termodinamiese model het die lugverbruik hoër voorspel in vergelyking met die eksperiment, weens die aanname van oombliklike klepgebeure.

# Acknowledgements

The author thanks Prof CJ Meyer for his supervision and guidance through the undertaken project. His passion and interest throughout the project was appreciated.

The author thanks Dr Tobias Louw for his guidance during the development of the thermodynamic models. His vast knowledge in the field of thermodynamics was greatly appreciated.

The author thanks Dr Van der Spuy and Mr Haines for their advice and guidance during the execution of the undertaken project.

The expert advice from Anton van den Berg during the design and manufacturing stage was highly appreciated. The author acknowledges Maurisha Galant and the rest of the MMW personnel for their contribution during the project.

# Table of Contents

	Page
<b>Abstract</b> .....	<b>ii</b>
<b>Uittreksel</b> .....	<b>iii</b>
<b>Acknowledgements</b> .....	<b>iv</b>
<b>Table of Contents</b> .....	<b>v</b>
<b>List of Figures</b> .....	<b>viii</b>
<b>List of Tables</b> .....	<b>xi</b>
<b>Nomenclature</b> .....	<b>xii</b>
<b>1 Introduction</b> .....	<b>1</b>
1.1 Background and Motivation.....	1
1.2 Objectives.....	2
<b>2 Literature Review</b> .....	<b>3</b>
2.1 Uniflow Steam Engine.....	3
2.1.1 Uniflow Steam Engine Cycle.....	5
2.1.2 Uniflow Piston Expander.....	7
2.2 Variable Valve Duration.....	9
2.2.1 Valve Gear Principles.....	9
2.2.2 The Caprotti Valve Gear.....	10
2.3 Valve Geometry.....	11
2.3.1 Bash Valves.....	11
2.3.2 Slide Valves.....	11
2.3.3 Piston Valves.....	12
2.3.4 Poppet Valves.....	13
<b>3 Thermodynamic Models</b> .....	<b>15</b>
3.1 Air Thermodynamic Model.....	15
3.2 Steam Thermodynamic Model.....	18
<b>4 Design Process</b> .....	<b>23</b>
4.1 Engine Conversion.....	23
4.1.1 Engine Modifications.....	23
4.1.2 Steam Chest.....	25

4.1.3	Inlet Valve Design .....	27
4.1.4	Valve Spring Design .....	35
4.2	Variable Valve Duration .....	39
4.2.1	Cam Design .....	39
4.2.2	Cam Follower Designs .....	45
4.2.3	Torsion Spring Design .....	48
4.2.4	Modified Caprotti Valve Gear Design .....	49
4.2.5	Manufactured Cams .....	53
4.2.6	Manufactured Rockers .....	55
4.2.7	Cam Phasing System .....	56
4.3	Engine Flywheel Redesign .....	59
<b>5</b>	<b>Engine Testing .....</b>	<b>61</b>
5.1	Test Bench Design .....	62
5.2	Air Test .....	65
5.2.1	Procedure .....	65
5.2.2	Results and Comparison to Model .....	66
<b>6</b>	<b>Conclusions .....</b>	<b>73</b>
6.1	Objectives .....	73
6.1.1	Develop a Thermodynamic Model of a Reciprocating Steam Engine Cycle: .....	73
6.1.2	Design and Manufacture a Proof of Concept Variable Valve Duration Reciprocating Piston Expander from an Existing ICE: .....	73
6.1.3	Perform Tests on the Developed Prototype Engine at Various Cut-Off Ratios to Determine the Effect on Power Output and Air Consumption: .....	73
6.1.4	Evaluate the Performance of the Constructed Engine and Compare to Thermodynamic Model: .....	74
6.2	Findings .....	74
6.3	Recommendations for Future Work .....	75
6.3.1	Design Recommendations .....	75
6.3.2	Thermodynamic Model Recommendations .....	75
6.3.3	Engine Testing Recommendations .....	75
6.3.4	Engine Testing on Steam Recommendations .....	76
<b>7</b>	<b>References .....</b>	<b>79</b>
<b>Appendix A : Pressure Vessel Report .....</b>		<b>81</b>
A.1	Introduction .....	81
A.2	SANS 347 Conformity .....	83
A.3	FEM Analysis .....	85

A.4 Bolt Analysis .....	89
A.5 Assembly Instructions .....	90
A.6 Engine Operation.....	91
A.7 Possible Failure Modes.....	92
A.8 SKF S19-F rod seal.....	93
A.9 JMP 6000 gasket.....	94
A.10 Cylinder head bolts.....	95
<b>Appendix B : Inlet Valve Matlab code .....</b>	<b>96</b>
B.1 ODE45 script.....	96
B.2 Flow Variables function.....	97
<b>Appendix C : Calculations .....</b>	<b>99</b>
C.1 Valve Spring Calculations .....	99
C.2 Cam Follower Calculations .....	100
C.3 Timing Belt Calculations .....	103
<b>Appendix D : Operating Manuals.....</b>	<b>104</b>
D.1 Briggs and Stratton 8HP Engine Manual .....	104
D.2 Festo MS6-SFE Hot-wire Flow Meter .....	105



# List of Figures

	<b>Page</b>
Figure 2.1: Stumpf's uniflow steam engine (Stumpf, 1922) .....	3
Figure 2.2: Uniflow steam engine schematic.....	4
Figure 2.3: Uniflow steam engine P-V diagram .....	6
Figure 2.4: Cut-off ratio effect on indicator diagram .....	7
Figure 2.5: Schematic of a Walschaert valve gear (Osborne, 2010).....	9
Figure 2.6: Caprotti valve gear (Caprotti, 1925) .....	10
Figure 2.7: The ANU reciprocating steam engine bash valve (Bannister, 1998) ...	11
Figure 2.8: Slide valve schematic .....	12
Figure 2.9: Piston valve schematic.....	12
Figure 2.10: Poppet valve diagram .....	13
Figure 3.1: Thermodynamic model solving order.....	15
Figure 3.2: Exhaust process schematic .....	19
Figure 4.1: Briggs and Stratton 319 cc ICE .....	23
Figure 4.2: CMM engine scan (left), engine CAD model (right).....	23
Figure 4.3: Machining of the exhaust port .....	24
Figure 4.4: Piston ring locating pin schematic (Jennings, 1987).....	25
Figure 4.5: Steam chest assembly.....	26
Figure 4.6: Inlet valve diagram .....	27
Figure 4.7: Pressure change within cylinder during filling for various engine speeds, 15 % CR, 2 mm valve lift .....	31
Figure 4.8: Pressure change within cylinder during filling for various engine speeds, 15 % CR, 3 mm valve lift .....	32
Figure 4.9: Pressure change within cylinder during filling for various engine speeds, 15 % CR, 4 mm valve lift .....	32
Figure 4.10: Mass of steam in cylinder during filling, 15 % CR, 500 rpm, 2 mm valve lift.....	33
Figure 4.11: Change in cylinder volume during filling, 15 % CR, 500 rpm, 2 mm valve lift.....	34

Figure 4.12: Steam temperature in cylinder during filling, 15 % CR, 500 rpm, 2 mm valve lift.....	34
Figure 4.13: Helical coil spring dimensional terminology (Elkon, 1987) .....	35
Figure 4.14: Helical coil end types (Elkon, 1987) .....	36
Figure 4.15: Stainless steel helical compression spring.....	38
Figure 4.16: Cam diagram .....	39
Figure 4.17: Constant velocity cam rise curve (Rothbart, 2004) .....	41
Figure 4.18: Simple harmonic cam rise curve (Rothbart, 2004) .....	42
Figure 4.19: Cam follower types (Rothbart, 2004) .....	45
Figure 4.20: Cam follower pressure angle .....	46
Figure 4.21: Radial vs offset oscillating roller follower.....	47
Figure 4.22: Double vs single bodied torsion springs (Elkon, 1987).....	48
Figure 4.23: Cam-follower assembly .....	50
Figure 4.24: Valve closed, both rockers not actuated .....	51
Figure 4.25: Valve closed, right rocker actuated .....	51
Figure 4.26: Valve opened, both rockers actuated .....	52
Figure 4.27: Valve closed, right rocker not actuated.....	52
Figure 4.28: Follower displacement curve during rise period .....	53
Figure 4.29: Follower velocity during rise period .....	54
Figure 4.30: Follower acceleration during rise period.....	54
Figure 4.31: Rocker assembly .....	55
Figure 4.32: Cam phasing system .....	57
Figure 4.33: Cam phasing system side view .....	58
Figure 5.1: Prototype uniflow steam engine assembly .....	61
Figure 5.2: Prototype engine test setup top view schematic.....	62
Figure 5.3: Torque measuring system .....	63
Figure 5.4: Prototype engine output torque versus cut-off ratio at 500 rpm.....	66
Figure 5.5: Prototype engine air consumption versus cut-off ratio at 500 rpm ...	67
Figure 5.6: Prototype engine speed versus cut-off ratio.....	67
Figure 5.7: Prototype engine power output versus cut-off ratio .....	69
Figure 5.8: Prototype engine experimental versus numerical power output.....	69

Figure 5.9: Prototype engine experimental versus numerical air consumption ...70

Figure 5.10: Valve lift schematic showing the effect of cut-off ratio on the overall percentage of opening and closing events .....71

# List of Tables

	<b>Page</b>
Table 1: Compression spring dimensional characteristic equations (Elkon, 1987) .....	36
Table 2: Measured exhaust air temperature versus the theoretical exhaust air temperature.....	68

# Nomenclature

Roman letters	Description	Units
$A$	Piston area . . . . .	$[m^2]$
$A_v$	Valve area . . . . .	$[m^2]$
$C$	Spring index . . . . .	$[-]$
$C_d$	Discharge coefficient . . . . .	$[-]$
$C_f$	Flow coefficient . . . . .	$[-]$
$c_v$	Constant volume specific heat. . . . .	$[kJ \cdot (kg \cdot K)^{-1}]$
$c_0$	Stagnation speed of sound . . . . .	$[m \cdot s^{-1}]$
$D$	Spring mean diameter . . . . .	$[m]$
$D_1$	Initial spring mean diameter . . . . .	$[m]$
$d$	Spring wire diameter . . . . .	$[m]$
$d_{valve}$	Valve diameter . . . . .	$[m]$
$E$	Modulus of elasticity . . . . .	$[Pa]$
$E_{flywheel}$	Flywheel kinetic energy . . . . .	$[kJ]$
$E_{mass,in}$	Mass flow energy entering system . . . . .	$[kJ]$
$E_{mass,out}$	Mass flow energy leaving system . . . . .	$[kJ]$
$\Delta E_{system}$	Change in energy within system . . . . .	$[kJ]$
$F_{spring}$	Compression spring force . . . . .	$[N]$
$f$	Frequency of engine cycles . . . . .	$[Hz]$
$G$	Modulus of rigidity . . . . .	$[Pa]$
$g$	Gravitational acceleration . . . . .	$[m \cdot s^{-2}]$
$h$	Cam rise height . . . . .	$[m]$
$h_e$	Exhaust steam enthalpy . . . . .	$[kJ \cdot kg^{-1}]$
$h_{in}$	Specific enthalpy of inlet steam . . . . .	$[kJ \cdot kg^{-1}]$
$h_j$	Steam enthalpy in cylinder at stage $j$ . . . . .	$[kJ \cdot kg^{-1}]$
$I$	Moment of inertia . . . . .	$[kg \cdot mm^2]$
$I.D$	Spring inner diameter . . . . .	$[m]$
$K_w$	Wahl stress correction factor . . . . .	$[-]$

$k$	Spring rate . . . . .	[N·m <sup>-1</sup> ]
$L_f$	Spring free length . . . . .	[m]
$L_j$	Torsion spring end lengths . . . . .	[m]
$L_s$	Spring solid length . . . . .	[m]
$L_{\text{torsion}}$	Length of torsion spring . . . . .	[m]
$l$	Valve lift . . . . .	[m]
$l_{\text{conrod}}$	Con rod length . . . . .	[m]
$l_{\text{def}}$	Spring deflection . . . . .	[m]
$m_{\text{cyl}}$	Steam mass in cylinder . . . . .	kg
$m_e$	Mass of steam exhausted . . . . .	kg
$m_j$	Mass in cylinder at stage $j$ . . . . .	kg
$\dot{m}$	Engine air/steam consumption . . . . .	[kg·s <sup>-1</sup> ]
$\dot{m}_{\text{in}}$	Steam mass flow rate into cylinder . . . . .	[kg·s <sup>-1</sup> ]
$N_a$	Number of active coils . . . . .	[-]
$N_b$	Number of body coils . . . . .	[-]
$N_e$	Number of equivalent coils . . . . .	[-]
$N_t$	Total number of coils . . . . .	[-]
$n$	Natural frequency . . . . .	[Hz]
$O. D$	Spring outer diameter . . . . .	[m]
$P_b$	Exhaust back pressure . . . . .	[Pa]
$P_{\text{comp}}$	Cylinder pressure during compression . . . . .	[Pa]
$P_{\text{down}}$	Steam pressure downstream of valve . . . . .	[Pa]
$P_{\text{exp}}$	Cylinder pressure during expansion . . . . .	[Pa]
$P_i$	Inlet pressure . . . . .	[Pa]
$P_j$	Pressure in cylinder at stage $j$ . . . . .	[Pa]
$P_{\text{out}}$	Power output . . . . .	[W]
$P_{\text{up}}$	Steam pressure upstream of valve . . . . .	[Pa]
$P_v$	Cylinder pressure . . . . .	[Pa]
$P_0$	Stagnation pressure . . . . .	[Pa]
$p$	Pitch . . . . .	[m]

$Q_{in}$	Heat energy entering system . . . . .	[kJ]
$Q_{out}$	Heat energy leaving system . . . . .	[kJ]
$R$	Specific gas constant . . . . .	[kJ·(kg·K) <sup>-1</sup> ]
$r$	Crank arm radius . . . . .	[m]
$S$	Stress in helical spring . . . . .	[Pa]
$s_j$	Steam specific entropy in cylinder at stage $j$ . . .	[kJ·(kg·K) <sup>-1</sup> ]
$T_{exh}$	Exhaust air temperature . . . . .	[K]
$T_j$	Temperature in cylinder at stage $j$ . . . . .	[K]
$T_0$	Stagnation temperature . . . . .	[K]
$\Delta T$	Change in cylinder steam temperature with respect to time . . . . .	[K]
$t$	Time . . . . .	[s]
$t_f$	Open valve duration . . . . .	[s]
$\Delta U$	Change in steam internal energy in cylinder . . .	[kJ]
$u_e$	Internal energy of steam exhausted . . . . .	[kJ·kg <sup>-1</sup> ]
$u_j$	Steam specific internal energy in cylinder at stage $j$ . . . . .	[kJ·kg <sup>-1</sup> ]
$V_{cs}$	Clearance space volume . . . . .	[m <sup>3</sup> ]
$V_e$	Cylinder volume just before exhaust . . . . .	[m <sup>3</sup> ]
$V_j$	Volume in cylinder at stage $j$ . . . . .	[m <sup>3</sup> ]
$V_s$	Cylinder volume at BDC . . . . .	[m <sup>3</sup> ]
$V_x$	Volume in cylinder at position $x$ . . . . .	[m <sup>3</sup> ]
$\Delta V$	Change in cylinder volume with respect to time	[m <sup>3</sup> ·s <sup>-1</sup> ]
$v_e$	Specific volume of steam exhausted . . . . .	[m <sup>3</sup> ·kg <sup>-1</sup> ]
$v_j$	Steam specific volume in cylinder at stage $j$ . . .	[m <sup>3</sup> ·kg <sup>-1</sup> ]
$W_{cycle}$	Work output per engine cycle . . . . .	[J·cycle <sup>-1</sup> ]
$W_{in}$	Work energy entering system . . . . .	[kJ]
$W_{out}$	Work energy leaving system . . . . .	[kJ]
$W_{spring}$	Spring weight . . . . .	[N]
$\Delta W_{1-2}$	Work performed during steam admission . . . . .	[kJ]
$\Delta W_{2-3}$	Work performed during steam expansion . . . . .	[kJ]

$\Delta W_{4-5}$	Work performed during steam compression . . .	[kJ]
$x$	Piston displacement . . . . .	[m]
$\dot{x}$	Piston velocity . . . . .	[m·s <sup>-1</sup> ]
$y$	Cam follower displacement . . . . .	[m]
$\dot{y}$	Cam follower velocity . . . . .	[m·s <sup>-1</sup> ]
$\ddot{y}$	Cam follower acceleration . . . . .	[m·s <sup>-2</sup> ]
$\ddot{\ddot{y}}$	Cam follower jerk . . . . .	[m·s <sup>-3</sup> ]

<b>Greek symbols</b>	<b>Description</b>	<b>Units</b>
$\alpha$	Rocker angular acceleration . . . . .	[rad·s <sup>-2</sup> ]
$\beta$	Angle of rise period . . . . .	[rad]
$\gamma$	Specific heat ratio . . . . .	[-]
$\theta$	Cam rotation angle . . . . .	[rad]
$\theta_{\text{rev}}$	Torsion spring applied revolutions . . . . .	[rad·s <sup>-1</sup> ]
$\rho_0$	Stagnation density . . . . .	[kg·m <sup>-3</sup> ]
$\rho_j$	Density in cylinder at stage $j$ . . . . .	[kg·m <sup>-3</sup> ]
$\tau$	Torque . . . . .	[N·m]
$\phi$	Harmonic curve incremental angle of rotation .	[rad]
$\omega$	Engine speed . . . . .	[rad·s <sup>-1</sup> ]



<b>Abbreviations</b>	<b>Description</b>
ANU	Australian National University
BDC	Bottom Dead Centre
CMM	Co-ordinate Measuring Machine
CR	Cut-off Ratio
CS	Clearance Space
CSPP	Concentrating Solar Power Plants
DC	Direct Current
EP	Exhaust Port
FEA	Finite Element Analysis
FEM	Finite Element Method
ICE	Internal Combustion Engine
LCOE	Levelized Cost of Electricity
NLPM	Normal Litres per Minute
RPM	Revolutions Per Minute
SEP	Sound Engineering Practice
TDC	Top Dead Centre



# 1 Introduction

## 1.1 Background and Motivation

There is an increasing demand for a renewable alternative to burning fossil fuels as a means to generate electricity. Many countries today have turned to solar-thermal power as a means of supplying additional power to their grid in an attempt to reduce the dependency on fossil fuels. It is estimated that solar thermal energy will contribute 11 % to the total global electricity generation by 2050 (Giovannelli, 2015).

Small-scale solar power plants (< 1 MW) are generally implemented in rural areas where power transmission via power lines is not feasible. Small-scale concentrating solar power plants (CSPP) have the potential for low levelised cost of electricity (LCOE), but still fall short due to the steam turbines being used. Steam turbines are high cost, high maintenance devices which have low efficiencies for power generation below 500 kWe (Bidini, et al., 1998).

Another factor which makes turbines unfavorable for small-scale application is the operating requirements. Steam turbines operate at high rotational speeds and as a result require high ratio gearboxes to reduce the driving speed of the generator. The high-speed operation of turbines also means that expensive lubrication systems are required (Sprouse & Depcik, 2013).

This project investigates the potential of converting an existing internal combustion engine (ICE) into a uniflow, reciprocating piston expander to replace steam turbines in small-scale CSP plants. The simplicity of reciprocating steam engines in comparison to turbines is beneficial for application in rural areas where highly skilled technicians are limited. The converted reciprocating steam engine can be repaired and maintained by a person with an intermediate knowledge of automotive mechanics (Bannister, 1998).

This project stems from the research done by The Australian National University (ANU) on the White Cliffs Solar Project in which a Lister diesel engine was converted into a reciprocating steam engine for use in its solar thermal power station. The system was shown to have a thermal efficiency of 21.9 % at a steam supply of 6.9 MPa and 450 °C (Bannister, 1998). The engine however, like steam turbines in that manner, had an inherently low operating range due to its fixed valve duration.

The undertaken project aimed to develop a reciprocating steam engine with variable valve duration to increase the operating range, a desirable trait for use in small-scale CSP plants.

This research focused on the design of a new and cost-effective system in which valve duration can be varied during operation which will allow the engine to operate over a wide range of power outputs. The motivation behind the conversion of an existing ICE is that the automotive industry is a vast and saturated field which results in engine components being affordable and readily available. This is desirable for small-scale CSP plants which rely on low capital and maintenance costs to be viable and competitive in the renewable energy market.

## **1.2 Objectives**

This project was aimed at developing a proof of concept variable valve duration piston-expander. The objectives of the project were:

- 1.1.1 Develop a thermodynamic model of a reciprocating steam engine cycle.
- 1.1.2 Design and manufacture a proof of concept variable valve duration reciprocating piston expander from an existing ICE.
- 1.1.3 Perform tests on the developed prototype engine at various cut-off ratios to determine the effect on power output and air consumption.
- 1.1.4 Evaluate the performance of the constructed engine and compare to thermodynamic model.

## 2 Literature Review

### 2.1 Uniflow Steam Engine

The uniflow steam engine, invented in 1885, was an attempt to produce a more efficient double-acting steam engine than its predecessors (Tompkins, 2013). Double-acting refers to an engine where steam is used to drive a piston on the forward and reverse stroke. The higher performance and efficiency of the uniflow engine in comparison to previous reciprocating steam engines is due to the temperature gradient along the cylinder which extends from the hot steam inlet to the cold exhaust port. As a result, less condensation of the inlet steam occurs and a better economy is achieved (Tompkins, 2013).

This steam engine was later further developed by Dr J. Stumpf to operate with a valve-gear system which controlled the duration of steam admission (Stumpf, 1922). This allowed the operator to control the steam consumption and power output of the engine.

Figure 2.1 shows the double-acting uniflow steam engine developed by Stumpf. Steam is admitted to alternating sides of the piston via double beat poppet valves. The steam is then exhausted when the piston moves past the exhaust port located in the centre of the cylinder's length.

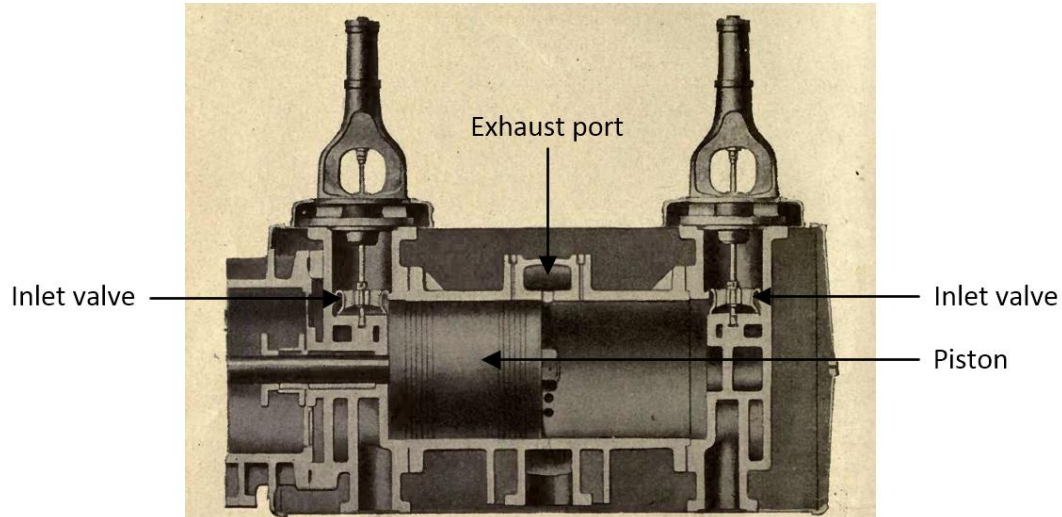
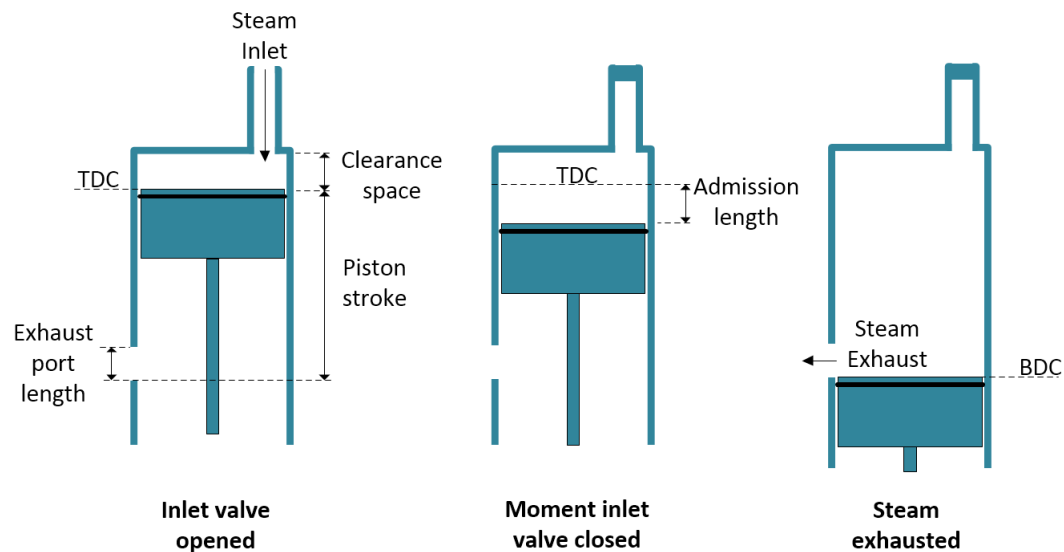


Figure 2.1: Stumpf's uniflow steam engine (Stumpf, 1922)

A generalised schematic of the uniflow steam engine is shown in Figure 2.2. The cut-off ratio (CR) of a steam engine refers to the percentage duration of piston stroke for which the inlet valve is open and is controlled by the valve gear.



**Figure 2.2: Uniflow steam engine schematic**

Cut-off ratios are made large if a high output torque is required at the cost of efficiency. Short cut-off ratios are used to admit small amounts of steam into the working chamber and allowed to expand for lower torque and greater efficiency operation.

For maximum torque outputs, steam is admitted into the cylinder for the entire stroke up until the piston passes and exposes the exhaust ports. The length of the exhaust port (EP) is commonly designed to be 10 % of the piston stroke and the compression length to be 90 % (Tompkins, 2013). The exhaust port is fully open when the piston reaches bottom dead centre (BDC).

An advantage of the exhaust port system on the uniflow steam engine is that its area can easily be made three times larger than that of the exhaust valve used in counter flow engines thus reducing losses due to throttling (Stumpf, 1922). Counter flow engines operate with the inlet and exhaust valve at the head of the cylinder whereas the uniflow engine exhausts at the bottom of the stroke.

A clearance space (CS) is required at the top of the cylinder to account for the compression of the remaining steam on the return stroke. This is the volume in the cylinder when the piston is at top dead centre (TDC). The size of this clearance volume determines the pressure to which the remaining steam will be compressed to on the return stroke.

The remaining steam in the cylinder after the exhaust process is due to the exhaust port arrangement. In counter flow engines the steam is forced out through the exhaust valve by the piston on the exhaust stroke. The exhaust process of the uniflow engine relies on the steam pressure within the cylinder to drive the exhaust flow. Thus, not all the steam is exhausted from the cylinder.

Relief-valves are required at the head of the cylinder to allow the release of steam should the steam in the engine be compressed to a higher pressure than the inlet steam (Tompkins, 2013). This is a safe-guard to prevent excessive pressures forming in the cylinder which could lead to failure of the engine. The pressure which the remaining steam is compressed to is known as the terminal compression pressure (Stumpf, 1922). A larger clearance volume causes an increase in steam consumption and a lower terminal compression pressure which reduces the engine's efficiency (Stumpf, 1922).

Uniflow steam engines can be categorized into two groups; condensing and non-condensing steam engines. Condensing engines refer to steam engines which exhaust the steam to a condenser which then feeds the water to a boiler for reuse. These engines operate with a vacuum pressure at the exhaust which aids the removal of the working steam from the cylinder (Stumpf, 1922). This in turn allows the engine to operate with smaller clearance volumes and therefore better efficiency.

Non-condensing engines simply emit the exhaust steam to the atmosphere and as a result require larger exhaust ports to allow rapid steam exhaustion and larger clearance volumes due to the lack of vacuum at the exhaust. These engines typically have a clearance space of 20 % (Stumpf, 1922).

### **2.1.1 Uniflow Steam Engine Cycle**

Steam power cycles are modelled using an indicator diagram to give a visual representation of the pressure change within the cylinder during the different stages of the engine cycle. An indicator diagram, also known as a P-V diagram, plots the pressure within the cylinder at the different piston displacements. The indicator diagram for a uniflow steam engine is shown in Figure 2.3 with  $P_i$  being the inlet pressure and  $P_b$  the back pressure.

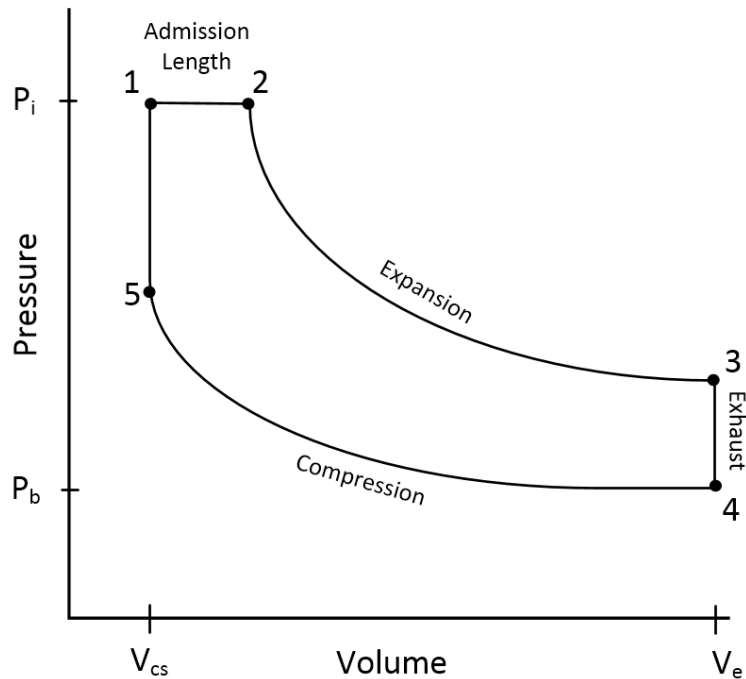


**Figure 2.3: Uniflow steam engine P-V diagram**

The indicator diagram of the uniflow steam engine can be approximated to comprise of 4 stages; steam admission, isentropic expansion, constant volume steam exhaust and isentropic compression during the return stroke.

The steam admission process comprises of a constant-volume pressure rise and a constant pressure volume change stage. Steam is admitted into the cylinder from point 5 to 2. At point 2 the inlet valve is closed and the steam expands during the piston down stroke until the exhaust port is reached at point 3. The volume just before the exhaust port is exposed is denoted  $V_e$ . The expansion is assumed to follow an isentropic process.

The cycle assumes that complete exhaustion occurs at a fixed piston position and neglects the work done during the piston motion when the exhaust port is exposed. This is seen by the constant volume exhaust line between point 3 and 4. Once the exhaust ports are covered again by the piston on the return stroke, isentropic compression of the remaining steam occurs until TDC is reached at point 5.

At this point the inlet valve is opened once again which results in a pressure rise between point 5 and 1. This process, like the exhaust, is assumed to occur instantaneously.



The ratio of admission length to piston stroke is defined as the cut-off ratio. The work output of a reciprocating engine for a single cycle is equal to the enclosed area within the P-V diagram.

The power output is determined by the work performed in a single cycle multiplied by the speed in Hertz at which the engine is operating. The larger the internal area of the P-V diagram, the larger the work done for a single cycle of the engine (Cengel & Boles, 2011). Figure 2.4 shows the effect that the cut-off ratio has on the P-V diagram of a uniflow steam engine.

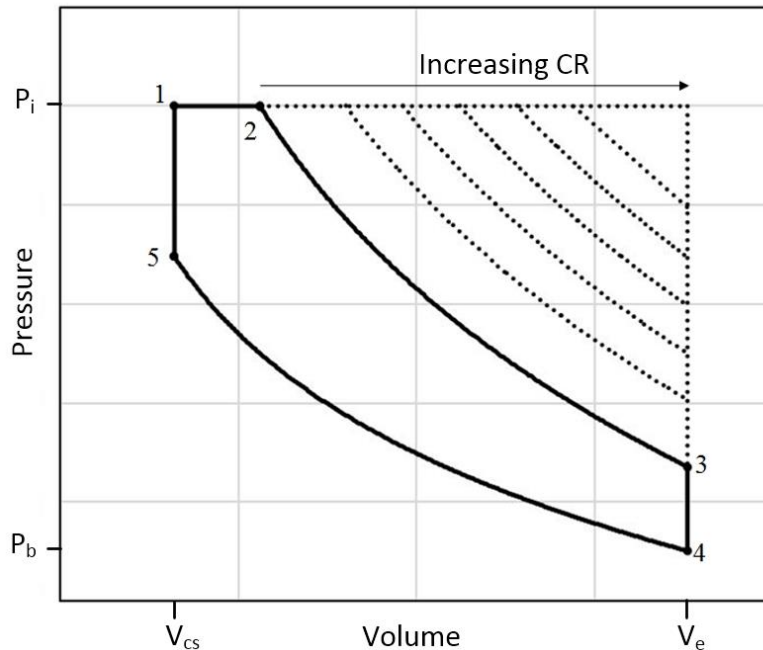


**Figure 2.4: Cut-off ratio effect on indicator diagram**

The maximum work the engine can perform is when the steam valve remains open for the entire stroke in which case the piston will be driven down by a constant pressure. A smaller CR results in a smaller internal area of the P-V diagram and thus less work performed in the cycle.

### 2.1.2 Uniflow Piston Expander

A uniflow piston expander is a piston-cylinder system which operates on the same principle as a uniflow steam engine. These are generally single acting piston devices which only experience a power stroke in one direction.

Piston expanders are expansion devices used in small-scale organic Rankine cycles to transfer the fluid's expansive energy into mechanical rotational energy. Piston expanders can also be used in steam Rankine cycles. These consist of a water

pump which pumps the water into a boiler where it is converted to steam. The high-pressure steam is then fed to the piston expander which extracts useable power from the expanding steam. The exhaust steam from the piston expander is then condensed before returning as water to the pump inlet (Bouvier, et al., 2016).

Steam piston expanders are commonly used in steam Rankine cycles for vehicle waste heat recovery. In 2016, Latz et al. developed a reciprocating piston expander in a water-based Rankine cycle for heat recovery from a heavy-duty diesel engine (Latz, et al., 2016). The piston expander operated in the same uniflow manner as shown previously in Figure 2.2.

The steam Rankine cycle boiler was supplied heat from the hot exhaust gases of the diesel engine. The generated steam was used to drive a twin cylinder piston expander to recover the waste energy (Latz, et al., 2016). Tests on the expander were performed at 600 rpm. It was found that operating at higher speeds had no positive influence on the expander's output power.

The thermal efficiency of the system was in the range of 5 % to 10 %. This low cycle efficiency was attributed to the design of the piston expander which experienced over-expansion at lower steam supply pressures (Latz, et al., 2016). Over expansion occurs when the steam in the cylinder is expanded below the exhaust back pressure. This creates a vacuum within the cylinder which opposes the piston's motion, thus reducing efficiency.

A way in which over expansion can be avoided is to either increase the cylinder's clearance space or to increase the cut-off ratio (Latz, et al., 2016). It is evident that a piston expander with a variable cut-off ratio would be more adaptive to varying steam supply pressures.

## 2.2 Variable Valve Duration

### 2.2.1 Valve Gear Principles

The cut-off ratio previously discussed is often a chosen fixed value for stationary steam engines. Some engines however offer the ability to vary the cut-off ratio during operation. These engines rely on a system referred to as a valve gear. A valve gear is a linkage system which controls the actuation of the inlet valves and is powered by the engine output shaft.

The most common valve gear is the Walschaerts valve gear used in locomotive steam engines. This valve gear consists of multiple linkages driven by an eccentric which controls the motion of a piston valve which feeds steam to the engine's cylinder (Osborne, 2010). The operator controls the cut-off ratio by moving the reach rod, as seen in Figure 2.5, which in turn leads or retards the motion of the piston valve. Many variations of this valve gear exist which all rely on a complex arrangement of linkages, push rods and eccentrics.

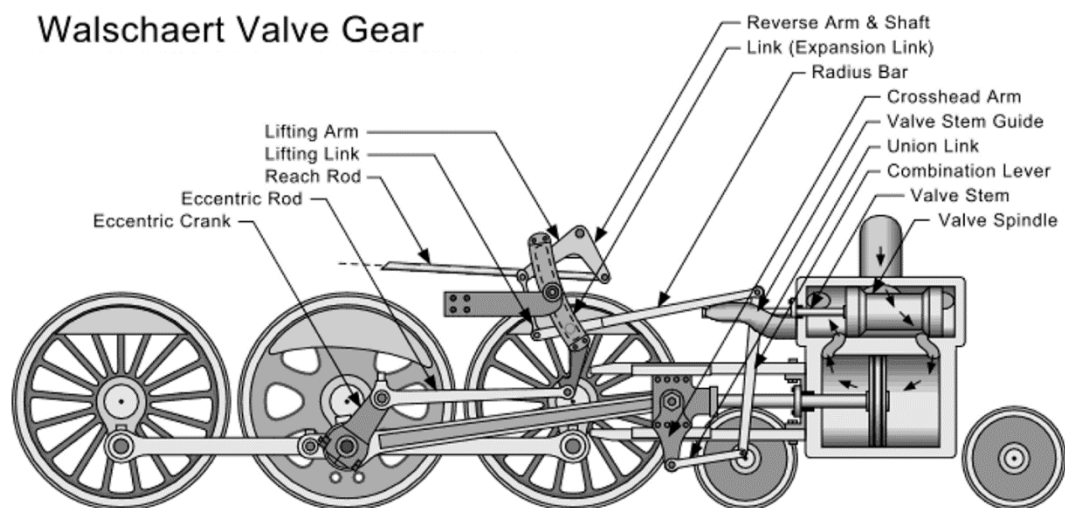


**Figure 2.5: Schematic of a Walschaert valve gear (Osborne, 2010)**

In steam locomotives, the valve gear serves the same purpose as a gearbox in an automotive engine. Large cut-off ratios are used to supply greater torque to get the locomotive up to speed. As the locomotive gains momentum, the cut-off ratio is reduced to increase efficiency. At full operating speed of the engine, the minimum cut-off ratio is used to admit small amounts of steam into the cylinder as at higher travelling speeds less torque is required from the engine (Osborne, 2010). The valve gear also gives the operator the ability to reverse the engine's direction.

## 2.2.2 The Caprotti Valve Gear

A lesser known valve gear, the Caprotti, was developed in 1921 by Arturo Caprotti to increase the efficiency of the steam locomotives at the time. The slide valves previously used in steam engines had the drawback that the inlet port and exhaust port were the same size. This caused inefficiencies as the volume of steam after expansion is far greater and thus needs a larger exhaust port than inlet (King, 2017).

The Caprotti valve gear utilises poppet valves for the inlet and exhaust of steam in the cylinder. This allows different size valves to be used to increase efficiency. The inlet valve is actuated by cams much like those in automotive engines. Automotive cams are fixed on the camshaft which give fixed valve events whereas the Caprotti valve gear uses two inlet cams which can be moved relative to one another. The single inlet valve is actuated by the two cams and by shifting their relative phase, the valve duration/cut-off ratio is changed. The exhaust valve is actuated by a separate cam which allows the exhaust activation to be uninfluenced by the change in cut-off, a common downfall of the existing slide valve gears at the time (Caprotti, 1925).

Figure 2.6 shows a Caprotti valve gear for a double-acting cylinder. The two cams rotate on a common spindle in close proximity to one another. The spindle has a helical gear mechanism to shift the relative phase of the cams. The follower system only actuates the inlet valve when both cams are lifting their follower wheel. By shifting the cams' phase with one another, the valve duration could be varied.

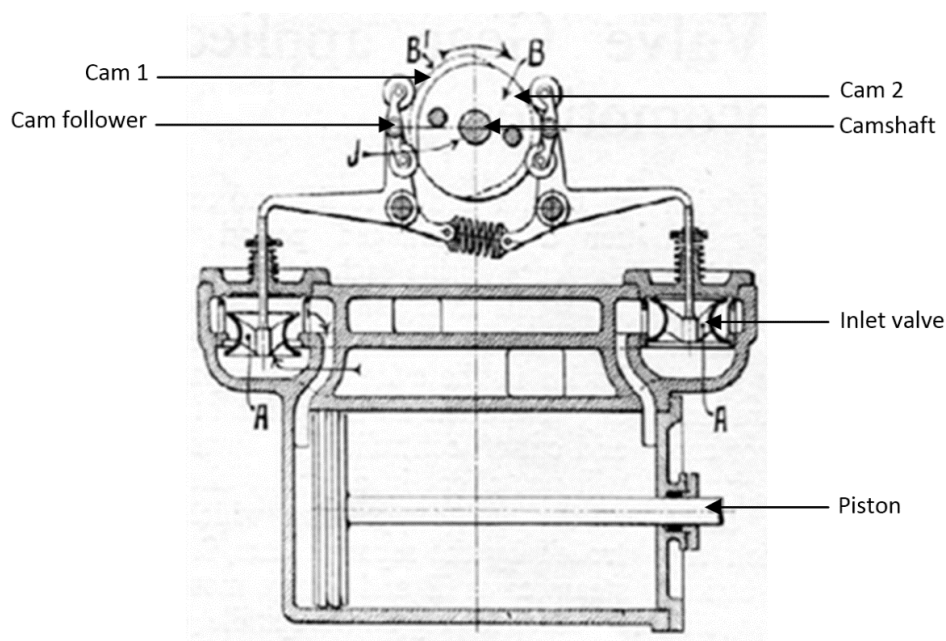


Figure 2.6: Caprotti valve gear (Caprotti, 1925)

## 2.3 Valve Geometry

### 2.3.1 Bash Valves

The use of reciprocating steam engines in solar thermal plants has previously been investigated by the White Cliffs Solar Thermal Power Plant project in Australia. The ANU have been developing uniflow steam engines for use in solar thermal plants since 1980 (Kaneff, 1991). The uniflow steam engine at White Cliffs was manufactured by using an existing diesel engine and converting it to operate on steam. The motivation behind this was to develop a rugged and easily maintained engine for use in rural areas. The design aimed to use as many existing diesel engine parts as possible to ensure an affordable and easily maintained system.

The ANU uniflow steam engine is a three cylinder Lister Model HR3 diesel engine which has been converted to operate as a reciprocating steam engine. The engine controls the inlet of steam into the working chamber by utilizing a bash valve system.

A bash valve is an inlet valve which is actuated by push pins on the piston head as shown in Figure 2.7. As the piston reaches TDC the valve pin lifts the ball in the ball valve off its seat and allows steam to be admitted into the cylinder. As the piston moves down the valve pin loses contact with the spring-loaded ball and the valve is closed. These valves are prone to wear and do not allow for variable valve duration.

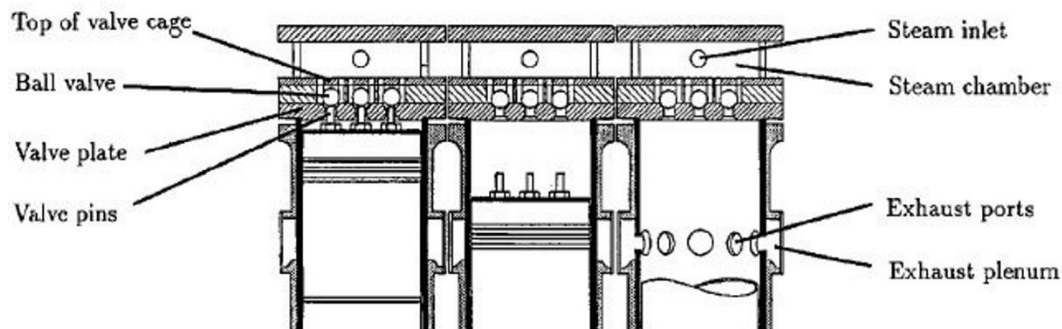


**Figure 2.7: The ANU reciprocating steam engine bash valve (Bannister, 1998)**

### 2.3.2 Slide Valves

The inlet valve of a steam engine is a crucial component which admits steam into the working cylinder at the correct time and duration. The largest flow restriction in the steam engine is the flow through the inlet valve and should thus be designed to minimise this effect (Stumpf, 1922).

A common inlet valve used in steam engines is the slide valve which is shown in Figure 2.8. The valve consists of a linear sliding block which is actuated by the engine's valve gear. The sliding block moves within the steam filled steam chest and exposes the inlet port to the engine cylinder at certain positions.

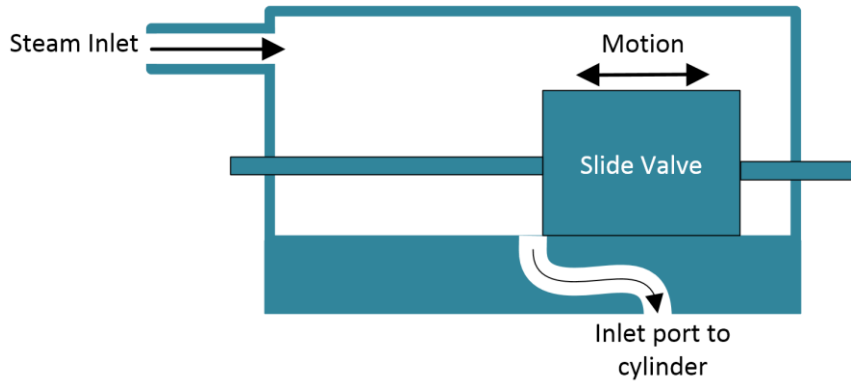


**Figure 2.8: Slide valve schematic**

Slide valves have the advantage of having few components which as a result requires less manufacturing. These valves however are prone to leakage during operation which reduces the overall efficiency of the engine. The tight tolerances required on the sliding surface for sealing makes these valves difficult to lubricate which results in wear between these surfaces and increases leakage. Slide valves are also often bent during operation due to over compression in the cylinder (Stumpf, 1922).

### 2.3.3 Piston Valves

A piston valve is similar to the slide valve as it is linearly actuated. A schematic of a piston valve is shown in Figure 2.9.

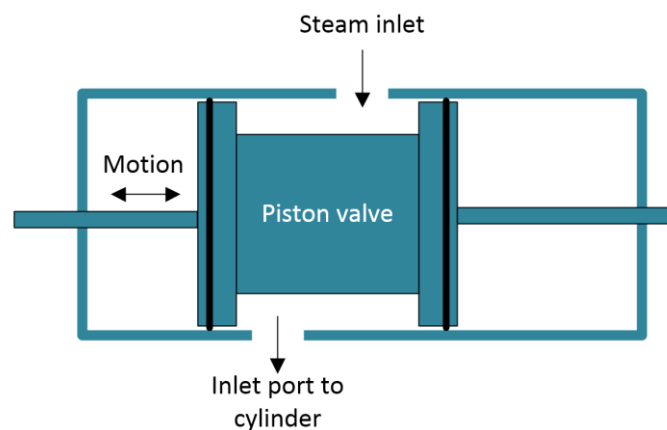


**Figure 2.9: Piston valve schematic**

The valve consists of a piston which moves linearly in a cylindrical steam chest. The piston has seals which slide along the inner surface of the steam chest. The piston valve schematic shows the position for which the valve is open. The valve is closed when the piston is moved to the right until the bottom outlet is no longer exposed to the steam filled chamber between the piston seals (Marks, 1854).

A piston valve experiences less wear in comparison to its predecessor, the slide valve. This is because the slide valve experiences different pressures from the steam on different portions of the valve whereas the piston valve does not. This leads to excessive wear of the slide valve and seating surface (Marks, 1854).

### 2.3.4 Poppet Valves

Poppet valves, also known as mushroom valves, are commonly found in internal combustion engines to control the intake and exhaust gases of the cylinder. The valve consists of a stem and cupped end shown in Figure 2.10. The valve slides in a linear guide which is concentric to the inlet port of the cylinder.

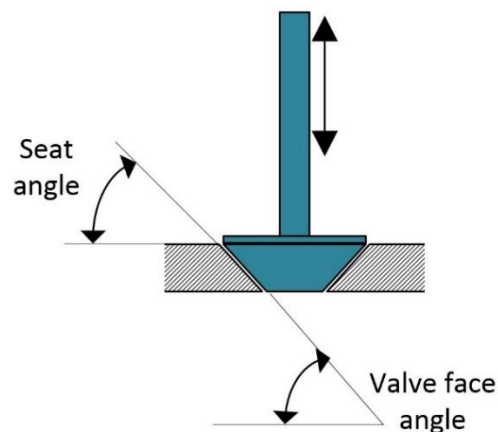


**Figure 2.10: Poppet valve diagram**

The valve cup has a chamfered edge (valve face) which acts as the sealing surface on the chamfered valve seat seen in Figure 2.10. The valve face angle should be designed as to maximise the valve opening whilst still ensuring sealing. A valve face angle of 0 degrees gives the maximum flow area. As the valve face angle is increased, the sealing force increases and the valve flow area decreases. A valve face angle of 45 degrees is commonly used in automotive engines as a balance between flow area and sealing force (Ferguson & Kirkpatrick, 2001). The valve face angle is designed to be 0.5 to 1 degrees less than the valve seat angle to create a sharp sealing edge between these surfaces. (Anonymous, 2017).





### 3 Thermodynamic Models

The first stage of the design process was the development of thermodynamic models which could determine the conditions within the cylinder during the engine cycle. Two thermodynamic models were developed in the undertaken project. One was developed for the proof of concept testing on a 10 bar air supply. The other was developed for potential future tests on a 10 bar, 180 °C saturated steam supply at John Thompson Boilers.

#### 3.1 Air Thermodynamic Model

The air model required the following parameters; supply pressure,  $P_i$ , exhaust back pressure,  $P_b$ , operating speed,  $\omega$ , cylinder stroke volume, CS [%], CR [%], and EP [%]. From these input parameters, the theoretical air consumption and power output of the engine was calculated.

Figure 3.1 shows the order in which the model calculated the varying pressures within the cylinder for a single engine cycle where each stage was previously defined in Figure 2.3.

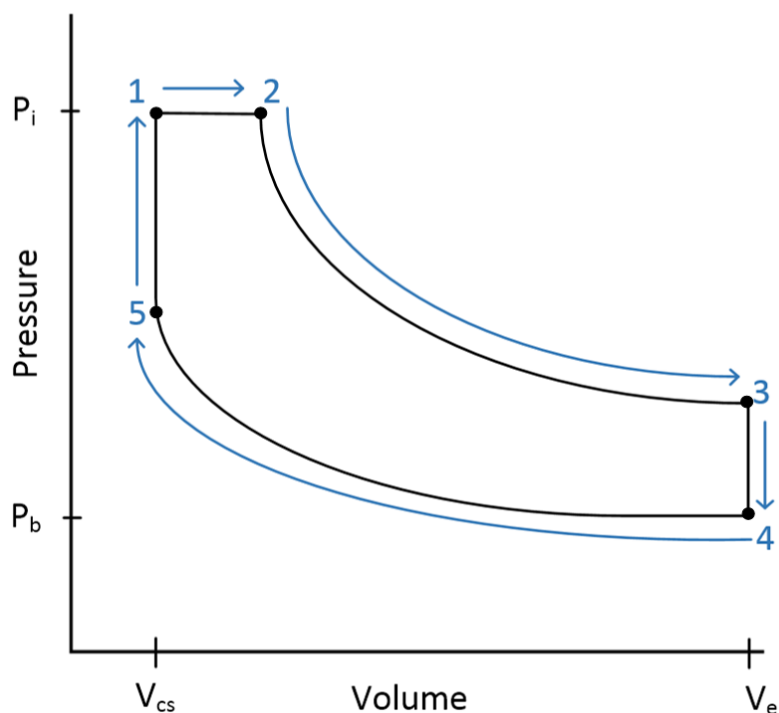


Figure 3.1: Thermodynamic model solving order

Point 1 has a volume,  $V_{cs}$ , and pressure equal to the user specified supply pressure,  $P_i$ . Here,  $V_{cs}$ , is the clearance space volume at TDC.

Point 2 was determined by assuming constant pressure air admission while the inlet valve is open so that  $P_1 = P_2$ . The volume at point 2,  $V_2$ , was determined using

$$V_2 = V_{cs} + \left( V_s * \frac{CR}{100} \right) \quad (3.1)$$

where,  $V_s$ , is the engine's stroke volume and CR is the specified cut-off ratio.

The isentropic expansion process between point 2 and 3 was modelled using

$$P_{exp}(V_x) = P_2 \left( \frac{V_2}{V_x} \right)^\gamma \quad (3.2)$$

for  $V_2 \leq V_x \leq V_3$  where  $V_x$  is the cylinder volume at any given point during expansion. The specific heat ratio,  $\gamma$ , was taken to be 1.4 for air at 300 K and assumed to remain constant (Cengel & Boles, 2011). The volume at point 3 was determined from

$$V_3 = V_{cs} + V_s \left( 1 - \frac{EP}{100} \right) \quad (3.3)$$

where EP is the specified exhaust port length as a percentage of stroke length.

The pressure at point 3 was determined using Equation (3.2) at  $V_x = V_3$ . Constant volume exhaustion was assumed from point 3 to 4, therefore  $V_4 = V_3$ . The pressure at point 4 was assumed to be equal to the specified back pressure. The outlet temperature of air from the exhaust was determined from

$$T_4 = T_3 \left( \frac{P_4}{P_3} \right)^{\frac{\gamma-1}{\gamma}} \quad (3.4)$$

which assumed an isentropic expansion process. The exhaust temperature of the engine,  $T_{exh}$ , was assumed to be equal to the temperature of air remaining in the cylinder  $T_4$ .

The isentropic compression process was given by

$$P_{comp}(V_x) = P_4 \left( \frac{V_4}{V_x} \right)^\gamma \quad (3.5)$$

for  $V_5 \leq V_x \leq V_4$  where  $V_5 = V_1$  as the piston returns to TDC. The pressure at point 5 was determined from Equation (3.5) with  $V_x = V_5$ .

The work performed in a single cycle is the enclosed area within the P-V diagram which was calculated by

$$W = P_1(V_2 - V_1) + \int_{V_2}^{V_3} P_{\text{exp}}(V_x)dx - \int_{V_5}^{V_4} P_{\text{comp}}(V_x)dx \quad (3.6)$$

which assumed no work is performed while the exhaust port is exposed. The power produced by the engine was then determined using

$$P_{\text{out}} = W_{\text{cycle}} * f \quad (3.7)$$

where  $f$  is the speed of the engine in hertz (Cengel & Boles, 2011). The air consumption for a single cycle of the engine was determined by calculating the mass increase in the cylinder from point 5 to point 2. The temperature at point 5,  $T_5$ , was calculated using the isentropic compression relationship shown by

$$T_5 = T_4 \left( \frac{P_5}{P_4} \right)^{\left(1 - \frac{1}{\gamma}\right)} \quad (3.8)$$

The mass of air in the cylinder at point 5,  $m_5$ , was calculated by assuming ideal gas behaviour and is expressed by

$$m_5 = \frac{P_5 V_5}{RT_5} \quad (3.9)$$

with  $R$  being the specific gas constant of air equal to  $0.287 \text{ kJ} \cdot (\text{kg} \cdot \text{K})^{-1}$ .

The mass of air in the cylinder at point 2,  $m_2$ , was calculated in a similar manner with  $T_2$  assumed to be equal to the temperature of the supply air,  $T_1$ .

$$m_2 = \frac{P_2 V_2}{RT_2} \quad (3.10)$$

The air consumption,  $\dot{m}$ , was determined by taking the mass increase from point 5 to 2 and multiplying by the frequency of engine cycles,  $f$ , for a given operating speed.

$$\dot{m} = (m_2 - m_5) \times f \quad (3.11)$$

## 3.2 Steam Thermodynamic Model

A separate model was created for the case of operation with steam. This model required the following parameters; supply steam pressure, supply steam temperature, supply steam quality, exhaust back pressure, operating speed, cylinder stroke volume, CS [%], CR [%] and EP [%]. The P-V diagram was determined in a similar manner to the air model. However, it required the use of steam tables to take into account the change in steam properties during the engine cycle.

Steam properties at point 1 were determined using the inlet steam pressure, temperature and quality. Again, the volume at point 1 was set equal to the specified  $V_{cs}$ .

The steam properties were assumed to stay constant during the steam admission from point 1 to 2. The volume at point 2 was determined using Equation (3.1). The specific volume at point 2,  $v_2$ , was obtained using steam tables. From this, the mass of steam in the cylinder at point 2,  $m_2$ , could be calculated using

$$m_2 = \frac{V_2}{v_2} \quad (3.12)$$

The expansion process from point 2 to 3 was assumed to be an isentropic process therefore  $s_3 = s_2$ . The volume in the cylinder at point 3,  $V_3$ , was calculated using Equation (3.3). The mass of steam in the cylinder at point 3,  $m_3$ , was set equal to  $m_2$  assuming no leakage of steam past the piston. The specific volume at point 3 was then calculated by

$$v_3 = \frac{V_3}{m_3} \quad (3.13)$$

The enthalpy,  $h_3$ , internal energy,  $u_3$ , and pressure,  $P_3$ , at point 3 were obtained from steam tables using  $s_3$  and  $v_3$ . Point 3 represented the conditions in the cylinder just before the exhaust port was exposed. The exhaust process from point 3 to 4 is shown in Figure 3.2. Here  $m_e$  and  $h_e$  represent the mass and enthalpy of the steam exhausted to the atmosphere from the cylinder.

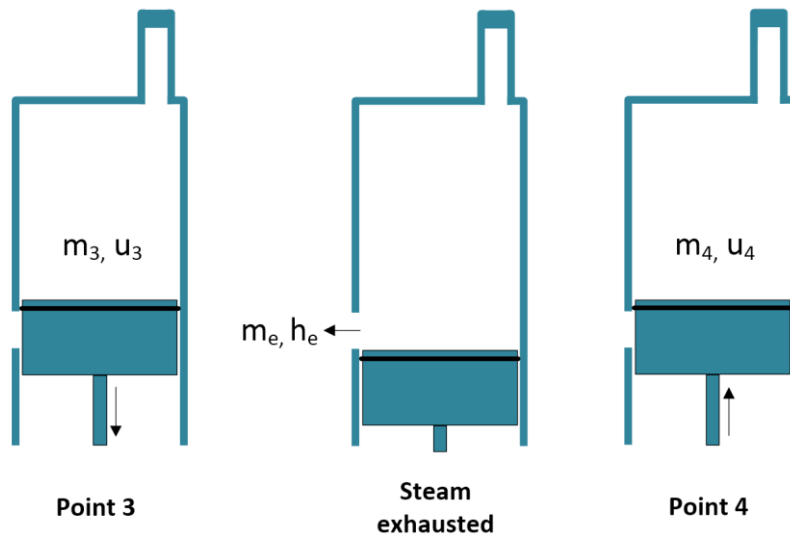


**Figure 3.2: Exhaust process schematic**

The mass and properties of steam left in the cylinder at point 4 after exhaustion were calculated using the conservation of energy equation for an open system (Cengel & Boles, 2011).

$$\Delta E_{\text{system}} = Q_{\text{in}} - Q_{\text{out}} + W_{\text{in}} - W_{\text{out}} + E_{\text{mass,in}} - E_{\text{mass,out}} \quad (3.14)$$

The steam inside the cylinder was modelled as the system. Here  $E_{\text{mass,in}}$  and  $E_{\text{mass,out}}$  represent the energy transfer associated with mass flow into and out of the system respectively. The terms  $Q$  and  $W$  represent the heat transfer and work transfer respectively.

Equation (3.14) was reduced to

$$m_4 u_4 - m_3 u_3 = -m_e \overbrace{(u_e + P_b v_e)}^{h_e} \quad (3.15)$$

for the case of negligible potential and kinetic energy changes in the system. It was assumed that no work was performed during this process therefore  $W_{\text{in}}$  and  $W_{\text{out}}$  are set to zero. The process was assumed to be adiabatic such that  $Q_{\text{in}} = 0$  and  $Q_{\text{out}} = 0$ . There is no mass flow into the system therefore  $E_{\text{mass,in}} = 0$ . Here the subscript  $e$  terms refer to the properties of steam leaving the system.

The mass leaving the cylinder,  $m_e$ , is equal to  $m_3 - m_4$ . Equation (3.15) was further reduced to

$$m_4 u_4 - m_3 u_3 = -(m_3 - m_4)(h_e) \quad (3.16)$$

Rearranging gave

$$m_4 = \frac{m_3 h_e + m_4 u_4 - m_3 u_3}{h_e} \quad (3.17)$$

which required iterative solving for  $m_4$ . The exhaust steam enthalpy,  $h_e$ , was taken to be the average between  $h_3$  and  $h_4$ . The steam remaining at point 4 was assumed to be in the wet steam region at atmospheric pressure. The mass of steam at point 4 is given by Equation (3.18).

$$m_4 = \rho_4 V_4 \quad (3.18)$$

Here  $\rho_4$  is the density at point 4 and  $V_4 = V_3$ .

The enthalpy of the steam at point 4,  $h_4$ , was acquired from the saturated steam tables using atmospheric pressure and  $\rho_4$ . The internal energy,  $u_4$ , was then acquired from the saturated steam tables using atmospheric pressure and the previously acquired  $h_4$ . The mass calculated in Equation (3.18), the enthalpy,  $h_4$ , and the internal energy,  $u_4$ , were then substituted into Equation (3.17).

Since  $\rho_4$  was unknown, the above process was performed for density values from  $\rho_4 = \rho_{\text{liquid}}$  to  $\rho_4 = \rho_{\text{vapor}}$  of saturated steam at 101.325 kPa. The density and correlating enthalpy and internal energy which resulted in the minimum difference between the LHS and RHS of Equation (3.17) was taken to be the solution.

The compression stage from point 4 to 5 was assumed to be an isentropic process therefore  $s_5 = s_4$ . At point 5 the piston is back at TDC such that  $V_5 = V_1$ . Assuming no leakage during compression, the specific volume at point 5 could be calculated using

$$v_5 = \frac{V_5}{m_4} \quad (3.19)$$

The enthalpy, internal energy and pressure at point 5 were obtained from the steam tables using the known entropy,  $s_5$ , and the calculated specific volume,  $v_5$ . A constant volume pressure rise was assumed to occur from point 5 to 1 as the inlet valve opened. The steam consumption was determined using Equation (3.11).

The work performed in a single engine cycle was calculated by determining the work output during each stage and summing them. The work during steam admission was calculated using Equation (3.20). This simplified to Equation (3.21) with the cylinder pressure  $P$  assumed constant during steam admission.

$$W_{1-2} = \int_{V_1}^{V_2} P dV \quad (3.20)$$

$$W_{1-2} = P_1(V_2 - V_1) \quad (3.21)$$

The work output during the expansion stage 2-3 was obtained by simplifying Equation (3.14) with the assumption that no leakage occurs from the cylinder during the expansion stage such that  $m_3 = m_2$ . This gave

$$\overbrace{Q_{\text{in}} - Q_{\text{out}}}^0 + W_{2-3} = \Delta U + \overbrace{\Delta KE + \Delta PE}^0 \quad (3.22)$$

for the case of negligible changes in kinetic and potential energy. The process was assumed to be adiabatic such that  $Q_{\text{in}} = 0$  and  $Q_{\text{out}} = 0$ . The process was modelled as a closed system therefore  $E_{\text{mass,in}}$  and  $E_{\text{mass,out}}$  are zero. Here  $\Delta U$  is the internal energy change from point 2-3. The work performed during the expansion process,  $W_{2-3}$ , was determined from

$$W_{2-3} = m_3(u_2 - u_3) \quad (3.23)$$

with  $u_2$  and  $u_3$  being the previously obtained specific internal energies at point 2 and 3 respectively. Again, it was assumed that no work is performed during the process from point 3 to 4 while the exhaust port is exposed. The work performed during the compression stage,  $W_{4-5}$ , was determined using

$$W_{4-5} = m_4(u_4 - u_5) \quad (3.24)$$

This results in a negative value as work is required to compress the remaining steam from point 4-5. The constant volume pressure rise from point 5-1 was assumed to perform no work. The total work performed during a single engine cycle,  $W_{\text{cycle}}$ , was then calculated using

$$W_{\text{cycle}} = \Delta W_{1-2} + \Delta W_{2-3} + \Delta W_{4-5} \quad (3.25)$$

The power output,  $P_{\text{out}}$ , could then be calculated using

$$P_{\text{out}} = W_{\text{cycle}} \times f \quad (3.26)$$

with  $f$  being the frequency of engine cycles per second.





## 4 Design Process

The following chapter presents the design process for the conversion of an existing ICE into a prototype reciprocating steam engine with variable valve duration.

### 4.1 Engine Conversion

#### 4.1.1 Engine Modifications

A single cylinder 319 cc 4-stroke Briggs and Stratton engine was acquired to be converted into a prototype steam engine. This engine was chosen for its simplicity in design. The engine had a 76.2 mm bore and 69.85 mm stroke. Figure 4.1 shows the engine before the conversion took place.



Figure 4.1: Briggs and Stratton 319 cc ICE

The engine was disassembled and a co-ordinate measuring machine (CMM), Figure 4.2 – left, used to measure the engine's geometry to an accuracy of 30 microns. These 3D co-ordinates were then imported into Autodesk Inventor 2016 so that a 3D model of the engine, Figure 4.2 – right, could be rendered.

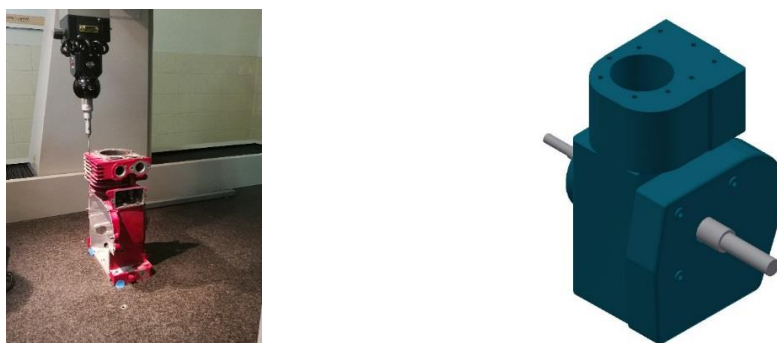
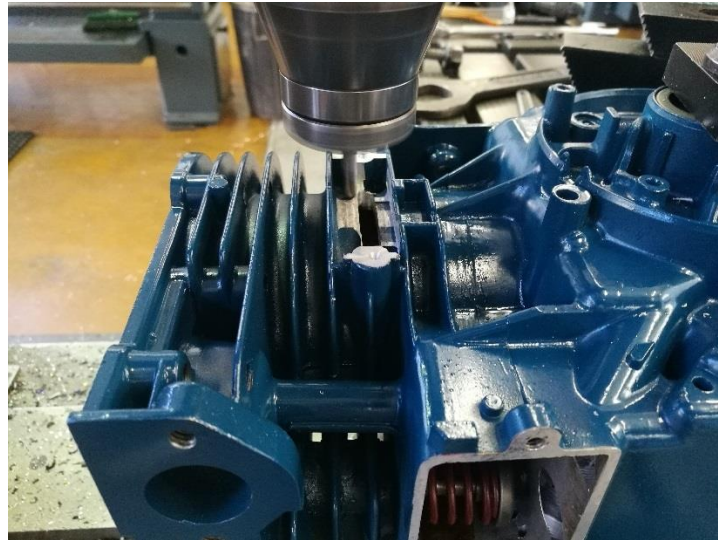


Figure 4.2: CMM engine scan (left), engine CAD model (right)

The 3D model was then used for designing the new cylinder head and variable valve duration system.

An exhaust port was machined into the engine cylinder show in Figure 4.3. The exhaust port was machined for the last 10 % of the piston stroke. The inside edge of the port was chamfered to prevent the piston ring catching as it passed the port.



**Figure 4.3: Machining of the exhaust port**

The existing engine had 3 piston rings on its piston; two compression rings and an oil control ring. These rings seal against the cylinder surface to prevent leakage past the piston during combustion, otherwise known as blow-by (Heywood, 1988).

The top compression ring is the main sealing ring. This ring is exposed to the highest temperatures and pressures during engine operation. The main purpose of the second compression ring is to minimise the pressure difference across the top compression ring (Heywood, 1988).

The oil ring serves the purpose of metering and distributing oil to the cylinder surface. This ring consists of two steel ring scrapers which scrape excess oil off the cylinder surface. The oil ring is made from a thin steel whereas the compression rings are made from cast iron (Heywood, 1988). For this reason, the oil ring is more prone to damage due to its flexibility.

For the conversion to a prototype steam engine, the second compression ring and oil ring were removed from the piston. This was done to minimise the chance of a piston ring catching on the exhaust port as well as reduce the friction on the piston motion.

All piston rings have a gap for ease of assembly as well as to allow room for expansion during exposure to high temperatures. The part of the piston ring with a gap is more prone to catching on the edge of the exhaust port.

The exhaust process on the developed engine is comparable to that of a 2 stroke ICE. Both processes rely on the piston to pass and expose the exhaust port on the down stroke.

A 2-stroke engine's piston has a locating pin in the piston ring groove which prevents the piston ring from rotating during operation. This is done to ensure the piston ring gap is always kept away from the exhaust port side of the cylinder. Figure 4.4 shows a schematic of a 2-stroke piston ring with a locating pin which is press fit into the piston body.

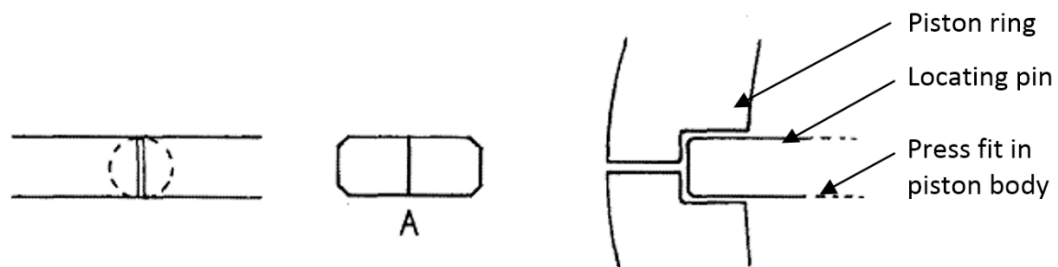
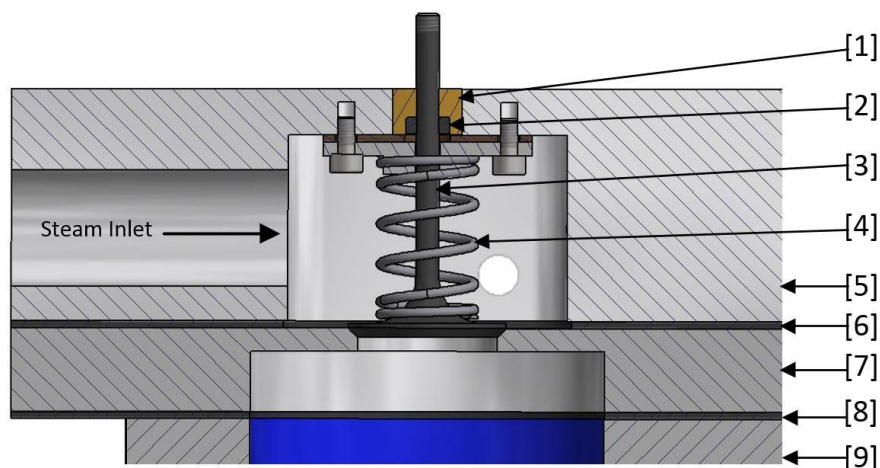


**Figure 4.4: Piston ring locating pin schematic (Jennings, 1987)**

The piston of the existing engine was modified to have a pin mounted in the piston ring groove like that in a 2-stroke piston. This pin was placed on the side of the piston opposite to the exhaust port side. A small cut out was machined on the inner diameter of the piston ring gap in which the pin would sit. This was done to prevent the gap rotating in line with the exhaust port and potentially causing damage to the piston ring.

#### **4.1.2 Steam Chest**

A steam chest was designed which would replace the cylinder head of the ICE. The steam chest assembly shown in Figure 4.5 was designed to accommodate a poppet valve, valve guide and valve seal. An inlet poppet valve with a 45 degree face angle was designed for reasons discussed in Section 2.3.4.



[1]: Valve guide	[5] Steam chest
[2]: Valve seal	[6]: JMP6000 gasket
[3]: Valve	[7]: Cylinder spacer
[4]: Valve spring	[8]: Head gasket
	[9] Engine cylinder

**Figure 4.5: Steam chest assembly**

A cylinder spacer, Figure 4.5 [7], was mounted between the steam chest and cylinder. The cylinder spacer had a cavity machined on the bottom which added a clearance space above the piston at TDC. The cavity had a diameter equal to the cylinder bore and a depth equal to 20 % of the engine's stroke for reasons discussed in Section 2.1.

The top of the cylinder spacer had a 44 degree valve seat, see Section 2.3.2, on which the poppet valve would seal. A JMP6000 fibre gasket was used between the steam chest and the cylinder spacer to withstand the temperature and pressure of potential tests on steam. See Appendix A.9 for the JMP6000 gasket datasheet. The steam chest and cylinder spacer were fastened to the engine using the existing cylinder head bolt holes.

The steam chest and cylinder spacer were manufactured from aluminium 6082 for ease and speed of manufacturing for the prototype tests. For operation on steam, it is recommended to manufacture these two components from a material with a lower thermal expansion coefficient than aluminium. This was determined from finite element method (FEM) analysis.

Initial FEM analyses were performed on the steam chest and cylinder spacer with a temperature of 180°C applied to the whole part. This was done as a worst-case

scenario. The steam chest experienced excessive forces at the bolting points due to the aluminium expanding from the applied temperature.

For safety purposes, a pressure relief valve was fitted to the steam chest. The engine was designed to operate with a 10 bar absolute air or steam supply. The safety valve was set to release if the pressure within in the cylinder exceeded 12 bar absolute, see Appendix A.1. The steam chest shown in Appendix A.1 had ports machined for the supply line, safety valve, a pressure gauge and a thermocouple.

A pressure vessel analysis was conducted on the designed steam chest and cylinder spacer according to the SANS 347 regulations (7). The operating point fell within the Sound Engineering Practice region of 7, A-4. FEM analyses were performed on the designed steam chest and cylinder spacer to determine the operating safety factor (Appendix A.3). The steam chest assembly was found to have an operating safety factor of 2 for air operation. The first component to fail would be the SKF S19-F rod seal which has a maximum operating pressure of 20 bar (Appendix A.8).

#### 4.1.3 Inlet Valve Design

The existing inlet and exhaust valves on the ICE were blocked up by the cylinder spacer and replaced with an inlet poppet valve from the steam chest and a machined exhaust port at the last 10 % of the piston stroke. A poppet valve which sealed on the high-pressure face was chosen for this application as depicted in Figure 4.6. This design allowed the valve to be self-sealing as the higher pressure in the steam chest kept the valve seated.

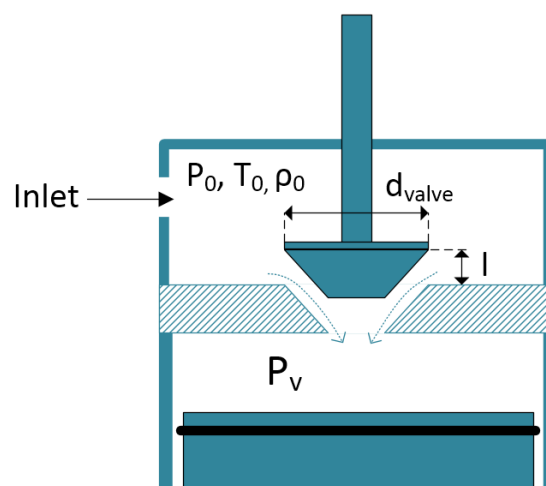


Figure 4.6: Inlet valve diagram

An important design consideration is the flow restriction through the inlet valve. If the restriction is too high, the cylinder would not be sufficiently filled during admission. This would result in a pressure far lower than the supply pressure and thus lower performance. The following model was developed for use during the design of the inlet valve to ensure sufficient filling during low cut-off ratio operation.

The mass flow rate through an ICE intake valve is shown by

$$\dot{m}_{in} = \rho_0 C_f A_v c_0 \left[ \frac{2}{\gamma - 1} \left( \left( \frac{P_v}{P_0} \right)^{\frac{2}{\gamma}} - \left( \frac{P_v}{P_0} \right)^{\gamma + \frac{1}{\gamma}} \right) \right]^{\frac{1}{2}} \quad (4.1)$$

where  $\rho_0$  is the stagnation density,  $C_f$  is the valve flow coefficient,  $A_v$  is the flow cross sectional area at the valve,  $c_0$  is the stagnation speed of sound,  $P_v$  is the valve static pressure,  $P_0$  is the stagnation pressure and  $\gamma$  is the specific heat ratio of the fluid (Ferguson & Kirkpatrick, 2001).

For an ICE intake valve flow the stagnation conditions refer to the conditions upstream to the valve and for exhaust valve flow it refers to the conditions within the cylinder. The stagnation conditions for the designed valve refer to the conditions in the steam chest and the valve pressure,  $P_v$ , is taken as the pressure in the cylinder shown in Figure 4.6 (Ferguson & Kirkpatrick, 2001).

The valve flow area,  $A_v$ , can be determined by either calculating it as the curtain area,  $A = \pi d_{valve} l$ , or the valve seat area,  $A = \frac{\pi d_{valve}^2}{4}$ . Here,  $d_{valve}$  is the valve diameter and  $l$  is the valve lift. For valves with low lift, the curtain area is used as  $A_v$  and the flow coefficient,  $C_f$ , is denoted as,  $C_d$ , the discharge coefficient (Ferguson & Kirkpatrick, 2001). The stagnation speed of sound is determined using

$$c_o = \sqrt{p_o R T_o} \quad (4.2)$$

where  $R$  is the specific gas constant of steam and  $T_0$  is the stagnation temperature.

An existing motorcycle poppet valve was modified for use as the inlet valve. The valve was designed to have a diameter of  $d_{valve} = 34$  mm. For the following valve flow model, the valve was assumed to open instantly, thus  $A_v$  is constant during steam admission.

The geometry of the designed steam valve in Figure 4.6 is comparable to an ICE exhaust valve as both valves lift against the flow direction. Thus, the discharge coefficient for the designed valve was taken to be 0.7 from data obtained for a

sharp-cornered exhaust poppet valve with a 45° seat angle for  $\frac{l}{d_{\text{valve}}} = 0.067$  (Ferguson & Kirkpatrick, 2001).

The supply pressure,  $P_0$ , was taken to be 10 bar saturated steam at 180 °C and the stagnation density determined at these conditions. The specific heat ratio,  $\gamma$ , was taken to be 1.327 at 300K and assumed to remain constant with temperature and pressure (Cengel & Boles, 2011).

The engine operating pressures were chosen as to prevent choked flow which occurs at the valve throat if the pressure ratio across the valve exceeds a critical value shown by

$$\left(\frac{P_{\text{up}}}{P_{\text{down}}}\right)_{\text{critical}} = \left(\frac{\gamma + 1}{2}\right)^{\frac{\gamma}{\gamma - 1}} \quad (4.3)$$

For non-choked flow, the upstream pressure can be taken as the supply pressure and the throat pressure as the cylinder pressure. The critical pressure ratio was determined to be 1.832 which meant for non-choked flow the cylinder terminal compression pressure must be greater than 5.457 bar which was determined using Equation (4.3) for a supply pressure of  $P_{\text{up}} = 10 \text{ bar}$ .

The mass flow rate into the cylinder is dependent on the pressure within the cylinder which too is changing with time. As a result, an equation for the varying mass flow rate was derived in the following manner assuming the case of an ideal gas. The change in internal energy within the cylinder can be written as

$$\Delta U = \dot{m}_{\text{in}} h_{\text{in}} - P_v \Delta V \quad (4.4)$$

Here  $h_{\text{in}}$  is the specific enthalpy of steam with mass flow rate,  $\dot{m}_{\text{in}}$ , entering the cylinder,  $P_v$  is the time varying cylinder pressure and  $\Delta V$  is the change in cylinder volume with respect to time.

The internal energy can be written as the specific internal energy multiplied by the mass of steam in the cylinder,  $m_{\text{cyl}}$ , as shown in Equation (4.5). The time derivative was then performed to attain Equation (4.6) through the chain rule.

$$U = m_{\text{cyl}} u \quad (4.5)$$

$$\Delta U = m_{\text{cyl}} \frac{du}{dt} + u \frac{dm_{\text{cyl}}}{dt} \quad (4.6)$$

Combining Equation (4.4) with (4.6) and noting that  $\frac{dm_{\text{cyl}}}{dt} = \dot{m}_{\text{in}}$ , yields

$$m_{\text{cyl}} \frac{du}{dt} = \dot{m}_{\text{in}}(h_{\text{in}} - u) - P_v \Delta V \quad (4.7)$$

The change in volume,  $\Delta V$ , of the cylinder is the piston velocity,  $\dot{x}$ , multiplied by the piston area,  $A$ . For a reciprocating engine, the piston displacement versus time is given by Equation (4.8) (Bateman, 2011).

$$x = (l_{\text{conrod}} + r) - r \cos(\omega t) + \sqrt{l_{\text{conrod}}^2 - r^2 \sin^2(\omega t)} \quad (4.8)$$

Here  $l_{\text{conrod}}$  is the conrod length,  $r$  is the crank arm radius and  $\omega$  is the angular velocity of the engine in radians per second. The velocity of the piston was derived by performing the time derivative of Equation (4.8) giving

$$\dot{x} = \left( r \sin(\omega t) + \frac{r^2 \sin(2\omega t)}{2l_{\text{conrod}}} \right) * \omega \quad (4.9)$$

Solving Equation (4.8) for time  $t$  with  $x$  being a known length dependent on the cut-off ratio, gave the amount of time the valve is open for,  $t_f$ .

The left-hand side of Equation (4.7) can be rewritten as  $m_{\text{cyl}} c_v \Delta T$  where  $c_v$  is the constant volume specific heat of steam and  $\Delta T$  is the change in temperature within the cylinder. Rearranging and rewriting the change in volume in terms of the piston velocity and area gives

$$\Delta T = \frac{\dot{m}_{\text{in}}}{m_{\text{cyl}} c_v} (h_{\text{in}} - u) - \frac{P_v \dot{x} A}{m_{\text{cyl}} c_v} \quad (4.10)$$

The following three ordinary differential equations were developed from Equations (4.1), (4.9) and (4.10). These were solved using the *ode45* MATLAB function from  $t = 0$  at TDC to  $t = t_f$  (Appendix B). This determined the dynamic flow of the steam admitted into the cylinder during the period when the valve is open. The initial cylinder temperature, volume and mass were obtained from the conditions at point 5 in the steam thermodynamic model. The pressure in the cylinder,  $P_v$ , was calculated using Equation (4.14) for each time step within the *ode45* solver.

$$\frac{dV}{dt} = \dot{x} A \quad (4.11)$$

$$\frac{dm_{\text{cyl}}}{dt} = \rho_0 C_f A_v c_0 \left[ \frac{2}{\gamma - 1} \left( \left( \frac{P_v}{P_0} \right)^{\frac{2}{\gamma}} - \left( \frac{P_v}{P_0} \right)^{\gamma + \frac{1}{\gamma}} \right) \right]^{\frac{1}{2}} \quad (4.12)$$



$$\frac{dT}{dt} = \frac{\dot{m}_{in}}{m_{cyl}c_v} (h_{in} - u) - \frac{P_v \dot{x}A}{m_{cyl}c_v} \quad (4.13)$$

$$P_v = \frac{mRT}{V} \quad (4.14)$$

The plotted lines in Figure 4.7 show the change in pressure within the cylinder during filling for various operating speeds. This was for the case of a valve lift equal to 2 mm. Figure 4.8 and Figure 4.9 are for the cases of 3 mm and 4 mm valve lift respectively. These were plotted for the minimum operating CR of 15 % since this is the CR most likely to result in underfilling of the cylinder.

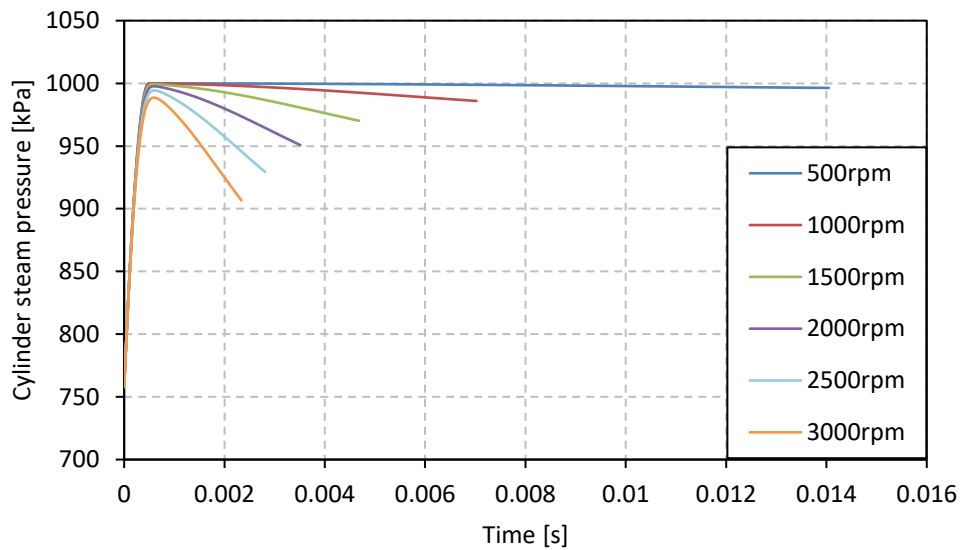


**Figure 4.7: Pressure change within cylinder during filling for various engine speeds, 15 % CR, 2 mm valve lift**

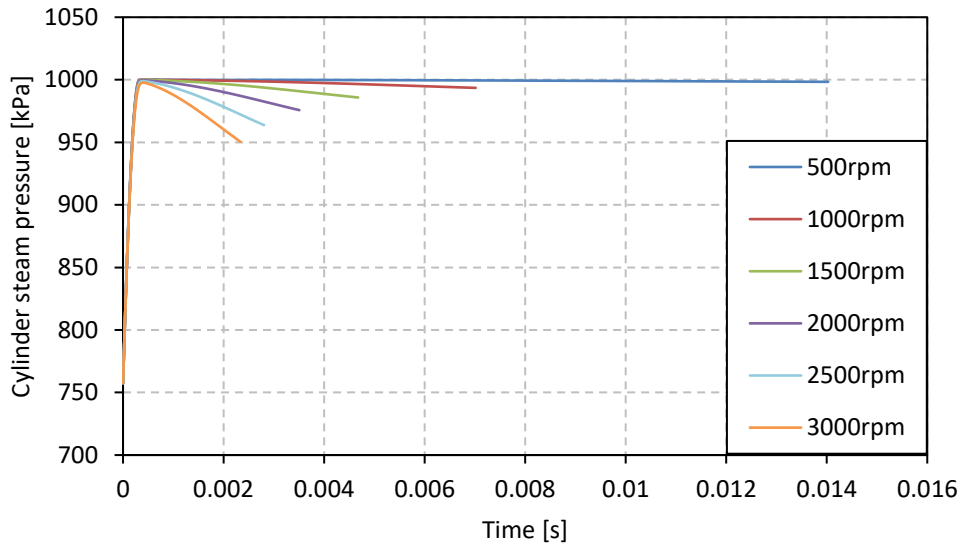


**Figure 4.8: Pressure change within cylinder during filling for various engine speeds, 15 % CR, 3 mm valve lift**

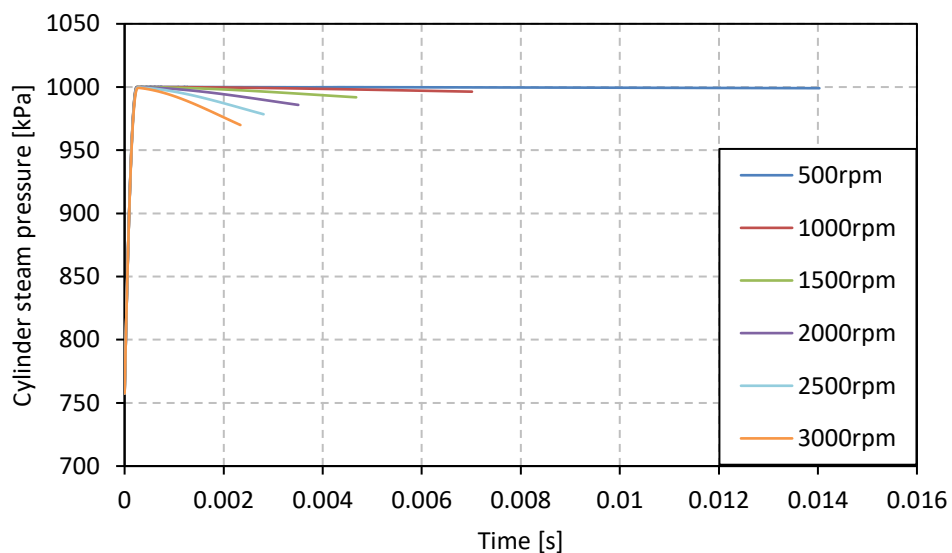


**Figure 4.9: Pressure change within cylinder during filling for various engine speeds, 15 % CR, 4 mm valve lift**

Increasing the engine speed decreases the time for which the valve is open and increases the piston velocity. At higher engine speeds, the cylinder volume increases at a faster rate. The inlet flow is unable to fill the cylinder fast enough which results in lower final filling pressures as seen by Figure 4.7, Figure 4.8 and Figure 4.9.

The end of each curve shows the pressure in the cylinder as the valve is closed. A lower pressure here will result in less work being performed during the expansion stage of the engine cycle. By comparing Figure 4.7, Figure 4.8 and Figure 4.9, it is evident that an increase in valve lift increases the final filling pressure and thus power output of the engine. This effect is seen to increase with higher engine speeds and have little influence at lower speeds.

An operating speed of 500 rpm and valve lift of 2 mm was chosen for the designed engine. These operating conditions were chosen based on the limitations involved in the cam design later discussed in Section 4.2.1.

Figure 4.10 shows the mass of steam within the cylinder during filling for a valve lift of 2 mm. This was plotted for a 15 % CR at 500 rpm. The gradient at any given point is the mass flow rate of steam into the cylinder. Initially the mass flow rate is high since there is a large pressure difference between the cylinder pressure and supply pressure.

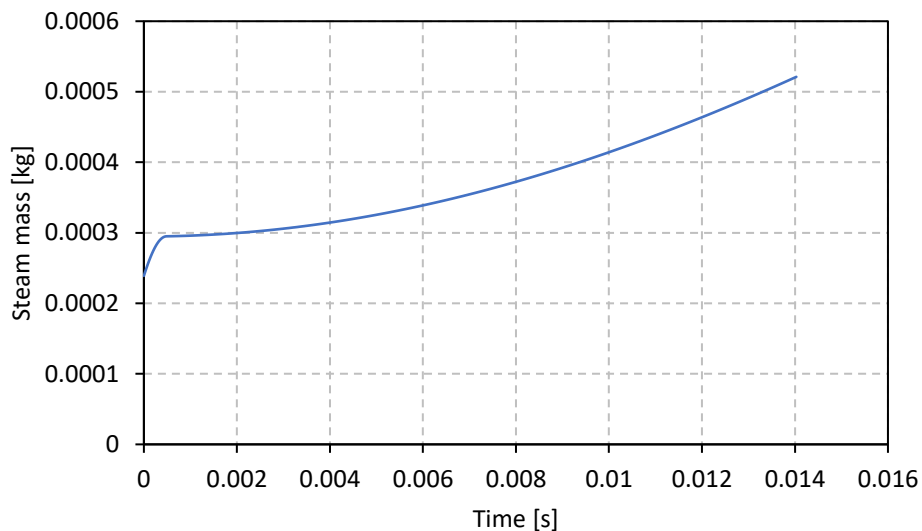


**Figure 4.10: Mass of steam in cylinder during filling, 15 % CR, 500 rpm, 2 mm valve lift**

As the cylinder pressure increases, the mass flow rate decreases until the inflection point near  $t = 3 \times 10^{-4}$  s is reached. From this point on the mass flow rate is seen to increase again.

This can be attributed to the change in volume versus time profile shown in Figure 4.11. Initially the rate of volume change is small as the piston is still near TDC where the piston velocity is the lowest. The rate of volume change then exponentially increases as time progresses. This higher rate of volume change causes a lower cylinder pressure which in turn causes a larger mass flow rate.

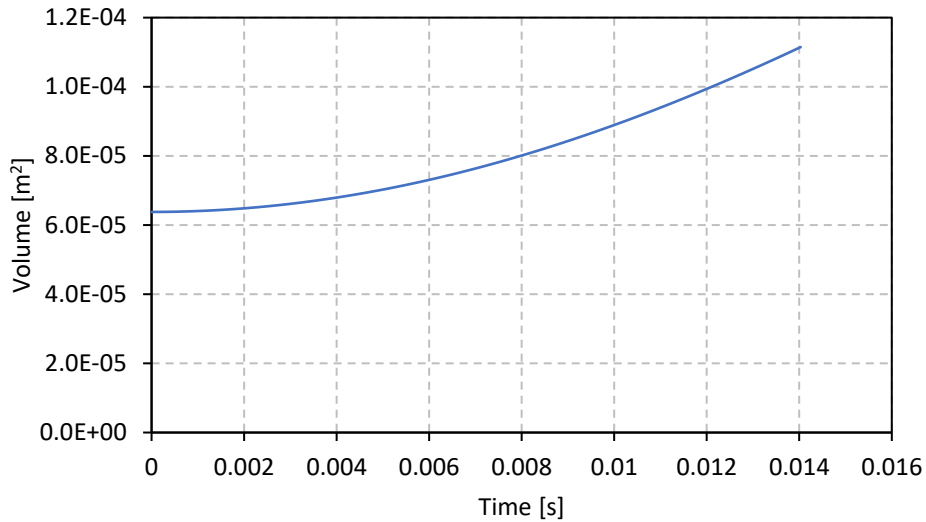


**Figure 4.11: Change in cylinder volume during filling, 15 % CR, 500 rpm, 2 mm valve lift**

The developed model calculated the change in temperature within the cylinder during filling. This is shown by the plot in Figure 4.12. The temperature is seen to reach a maximum at the same maximum cylinder pressure point. From here on a gradual decline in temperature is seen as the piston moves down.

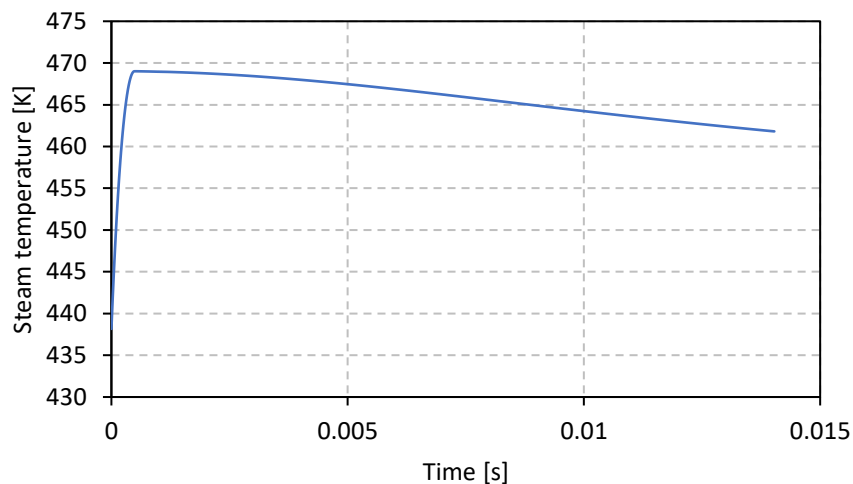


**Figure 4.12: Steam temperature in cylinder during filling, 15 % CR, 500 rpm, 2 mm valve lift**

#### 4.1.4 Valve Spring Design

The main purpose of the spring in a cam-follower system is to keep the follower in contact with the cam throughout the entire cam profile motion. In automotive cam systems, this is performed by the valve spring. This spring serves the purpose of keeping the valve securely seated as well as keeping the follower in contact with the cam. Helical compression springs are generally used for this application (Elkon, 1987).

Helical compression springs are designed to resist compressive forces for various applications. This is the most common type of spring configuration. A helical compression spring is shown in Figure 4.13 with dimensional terminology  $O.D.$ , the outer diameter,  $I.D.$ , the inner diameter,  $D$ , the mean diameter,  $d$ , the wire diameter,  $p$ , the coil pitch and  $L_f$ , the spring's free length (Elkon, 1987).

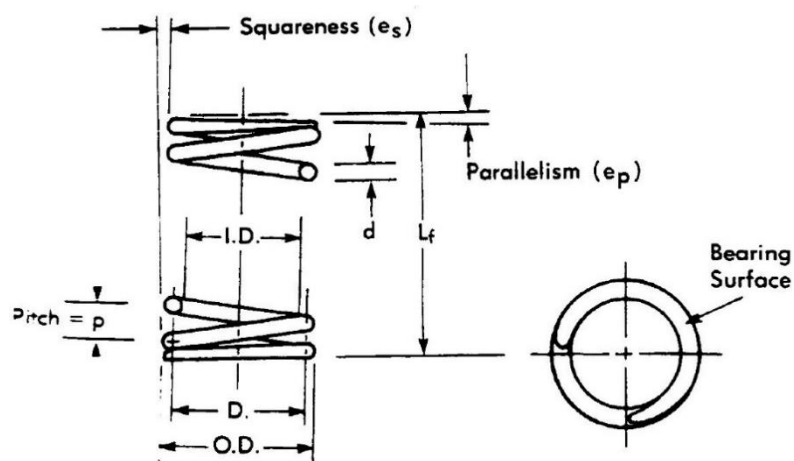


Figure 4.13: Helical coil spring dimensional terminology (Elkon, 1987)

The diameter of the spring increases when the spring is compressed. This increase in diameter is usually small however should still be considered when designing assembly systems to avoid interference with other components. Equation (4.15) gives the outer diameter of a helical spring which has been compressed to its solid length,  $L_s$ , which is the spring length at complete compression (Elkon, 1987).

$$O.D. @solid = \sqrt{D^2 + \frac{p^2 - d^2}{\pi^2}} + d \quad (4.15)$$

The spring index is the ratio of mean diameter,  $D$ , to the wire diameter,  $d$ , and should be kept in the range of 4 to 12 (Elkon, 1987). Helical compression springs are available in various types of ends such as plain ends, ground plain ends, square ends and ground square ends shown in Figure 4.14. Plain end springs require the

least manufacturing however are prone to cause buckling in the spring. Squared springs with ground ends are the most labour intensive however give the most even end support for the spring, thus reducing the possibility of spring buckling (Elkon, 1987).

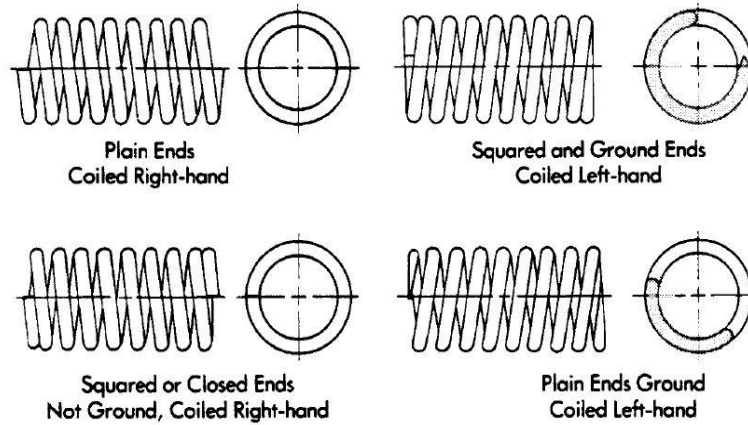


Figure 4.14: Helical coil end types (Elkon, 1987)

Table 1 gives standard equations used to determine dimensional characteristics of a helical compression springs for different type of ends.

Table 1: Compression spring dimensional characteristic equations (Elkon, 1987)

Dimensional characteristics	Type of Ends			
	Plain (Not ground)	Plain (ground)	Squared only	Squared and Ground
Solid Height ( $L_s$ )	$(N_t + 1)d$	$N_t d$	$(N_t + 1)d$	$N_t d$
Pitch ( $p$ )	$\frac{L_f - d}{N_a}$	$\frac{L_f}{N_t}$	$\frac{L_f - 3d}{N_a}$	$\frac{L_f - 2d}{N_a}$
Active Coils ( $N_a$ )	$\frac{L_f - d}{p}$	$\frac{L_f}{p} - 1$	$\frac{L_f - 3d}{p}$	$\frac{L_f - 2d}{p}$
Total Coils ( $N_t$ )	$N_a$	$N_a + 1$	$N_a + 2$	$N_a + 2$
Free Length ( $L_f$ )	$pN_t + d$	$pN_t$	$pN_a + 3d$	$pN_a + 2d$

The number of active coils,  $N_a$ , refers to the number of coils that deflect during compression. This will later be used to determine the spring rate,  $k$ . The total number of coils,  $N_t$ , refers to the total number of coil winds which is the active

coils plus the number of windings at the end depending on the type of end as shown in Table 1.

For a helical compression spring, the spring rate,  $k$ , is determined by

$$k = \frac{F_{\text{spring}}}{l_{\text{def}}} = \frac{Gd^4}{8D^3N_a} \quad (4.16)$$

and is defined as the spring force for a given deflection,  $l_{\text{def}}$ . This equation holds true for springs with a pitch angle less than 15 degrees (Elkon, 1987). Here  $D$  is the mean spring diameter,  $d$ , the wire diameter,  $G$ , the wire material's Modulus of rigidity and  $N_a$ , the number of active coils of the spring.  $F_{\text{spring}}$  is the force required to deflect the spring by a distance  $l_{\text{def}}$  (Elkon, 1987).

The stress,  $S$ , experienced by a helical is given by

$$S = \frac{8F_{\text{spring}}D}{\pi d^3} K_w \quad (4.17)$$

The torsional stress of a helical compression spring having a mean diameter,  $D$ , wire diameter,  $d$ , and applied load,  $F_{\text{spring}}$ . The  $K_w$  term is a correction factor to account for the stress not being uniformly distributed across the wire's cross section. The maximum stress occurs at the inner surface and is accounted for by this Wahl stress correction factor,  $K_w$  (Elkon, 1987). This can be calculated using

$$K_w = \frac{4C - 1}{4C - 4} + \frac{0.615}{C} \quad (4.18)$$

where the index,  $C = \frac{D}{d}$ .

Another factor which is of great concern when designing spring systems for dynamic loading is resonance. A spring experiences resonance when the cyclic loading frequency is near the natural frequency of the spring. Resonance can cause excessive stresses and deflections in the spring resulting in lower spring rates and could lead to failure of the spring. A guideline is to design the spring system to have a natural frequency at least 13 times greater than the loading frequency (Elkon, 1987). The natural frequency of a helical spring between two parallel plates is given by Equation (4.19) (Budynas & Nisbett, 2008).

$$n = \frac{1}{4} \sqrt{\frac{kg}{W_{\text{spring}}}} \quad (4.19)$$

Here,  $k$  is the spring stiffness,  $g$  is gravitational acceleration and  $W_{\text{spring}}$  is the weight of the spring.

A valve spring with dimensions shown in Figure 4.15 was designed and manufactured from stainless spring steel.

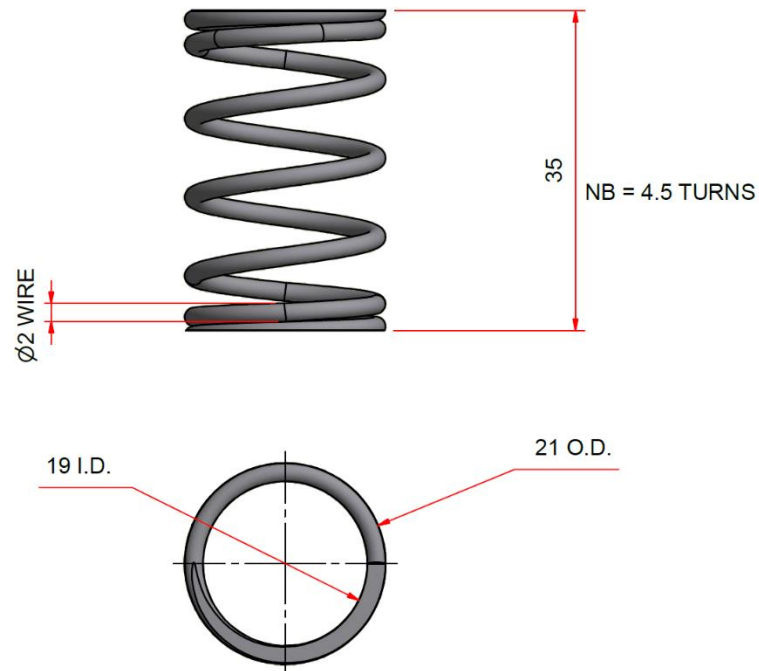


**Figure 4.15: Stainless steel helical compression spring**

The spring was designed to have a spring stiffness of  $3311.37 \text{ N}\cdot\text{m}^{-1}$ . The spring was preloaded by 5 mm such that the sealing force is 16.55 N (Appendix C.1). The spring was designed with squared ground ends for reasons previously discussed.

The maximum stress in the spring is when the valve is fully opened by the specified lift of 2 mm. This was found to be 176.25 MPa. This calculated stress is lower than the 240 MPa yield strength of stainless 302 spring steel.

The first natural frequency of the spring was calculated using Equation (4.19). This was found to be 287.723 Hz (Appendix C.1). The operating speed of 500 rpm results in the spring operating at 0.873 Hz. This value is sufficiently below the first natural frequency which ensures clear avoidance of resonance.



## 4.2 Variable Valve Duration

The following chapter contains the design process of the variable valve duration system for the prototype engine. This design was modified from the Caprotti valve gear presented in Section 2.2.2.

### 4.2.1 Cam Design

A cam is a component of a cam-follower mechanism which converts rotary motion into linear motion. The cam moves the follower by direct contact with a desired motion. Cams are classified by their shape, follower motion and follower constraint. Cams are most commonly seen in automotive engines to actuate the inlet and exhaust valves (Rothbart, 2004). These cams are classified as radial cams and consist of a risen lobe region as seen in Figure 4.16.

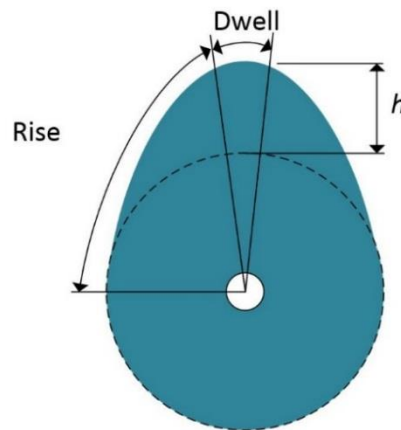


Figure 4.16: Cam diagram

The follower runs on the outer profile of the cam and moves according to the change in radius of the cam. Automotive cams consist of rise and dwell regions as depicted in Figure 4.16. The dwell is the duration for which the valve is completely open and is defined as a percentage of a full revolution of the cam. The lift of the cam is denoted,  $h$ , and is the difference between the base radius and lobe radius (Rothbart, 2004).

The displacement curve of the follower,  $y$ , is shown by

$$y = f(\theta) \quad (4.20)$$

where  $\theta$  is the cam rotation angle in radians. The cam angle,  $\theta$ , can be rewritten as

$$\theta = \omega t \quad (4.21)$$

with  $\omega$  being the cam angular velocity and  $t$  being the time taken to rotate by the angle  $\theta$ . For a constant angular velocity, Equation (4.20) can be rewritten as

$$y = g(t) \quad (4.22)$$

The instantaneous angular rate of change of displacement can be determined by deriving Equation (4.20) with respect to the cam rotation angle. This is shown by

$$y' = \frac{dy}{d\theta} \quad (4.23)$$

The instantaneous angular rate of change of velocity is determined by taking the angular derivative of Equation (4.23) and is given by

$$y'' = \frac{d^2y}{d\theta^2} \quad (4.24)$$

The follower velocity  $\dot{y}$  can then be determined as shown by

$$\dot{y} = \frac{dy}{dt} = \left(\frac{d\theta}{dt}\right) \left(\frac{dy}{d\theta}\right) = \omega \left(\frac{dy}{d\theta}\right) = \omega y' \quad (4.25)$$

The acceleration experienced by the follower can be determined using

$$\ddot{y} = \frac{d^2y}{dt^2} = \frac{d}{dt} \left(\frac{\omega dy}{d\theta}\right) = \frac{\omega d}{d\theta} \left(\frac{dy}{d\theta}\right) \left(\frac{d\theta}{dt}\right) = \omega^2 \left(\frac{d^2y}{d\theta^2}\right) = \omega^2 y'' \quad (4.26)$$

Equations (4.21) to (4.26) are used to convert from the cam profile equation to the displacement, velocity and acceleration curves of the follower.

Various profiles exist for the cam rise and return region and are chosen depending on the required application. The simplest cam displacement curve is the constant velocity curve which has a linear displacement curve given by

$$y = C_0 + C_1\theta \quad (4.27)$$

$$\text{at } \theta = 0, y = 0, \therefore C_0 = 0$$

$$\text{at } \theta = \beta, y = h, \therefore C_1 = \frac{h}{\beta}$$

with  $\beta$  being the angle of rotation of the rise,  $h$ . This profile has the shortest rise region of all cam curves.

The follower velocity is constant during the rise and thus the acceleration is zero. This curve however has excessive acceleration spikes at the beginning and end of the rise region where the follower has an instantaneous velocity change as seen in Figure 4.17. This infinite acceleration causes shocks in the cam-follower system and can result in component failure. As a result, this curve is not commonly used in practice (Rothbart, 2004).

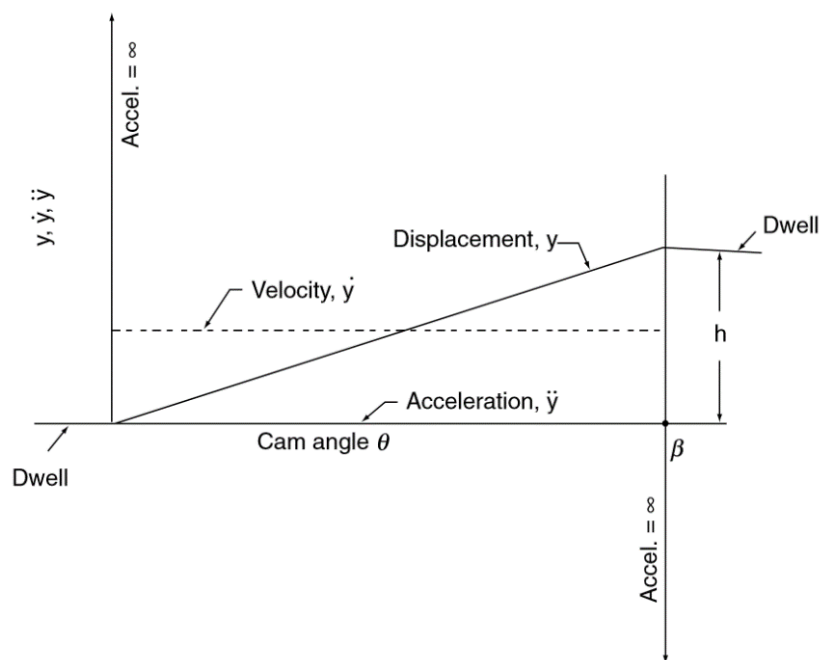


**Figure 4.17: Constant velocity cam rise curve (Rothbart, 2004)**

The curve with the smallest maximum follower acceleration is the constant acceleration curve otherwise known as the parabolic curve. The first half of the rise curve is given by

$$y = C\theta^2 \quad (4.28)$$

$$\text{For } 0 \leq \theta \leq \frac{\beta}{2}$$

$$\text{at } \theta = \frac{\beta}{2} \quad y = \frac{h}{2}$$

with  $C$  being a constant. The second half of the curve is described by Equation (4.29) (Rothbart, 2004).

$$y = C_0 + C_1\theta + C_2\theta^2 \quad (4.29)$$

$$\text{For } \frac{\beta}{2} \leq \theta \leq \beta$$

This curve, although having the lowest acceleration, experiences large acceleration changes at the beginning and end of the rise as well as at the transition point. Sudden changes in acceleration,  $\ddot{y}$ , also known as jerk, should be kept to a minimum in cam-follower design (Rothbart, 2004).

The most commonly used cam profile is the simple harmonic curve which has a cosine acceleration curve (Rothbart, 2004). The ease of construction is one of the reasons as to why the simple harmonic is so widely used. The harmonic motion displacement has the following function

$$y = \frac{h}{2}(1 - \cos\phi) \quad (4.30)$$

with  $h$  being cam lift and  $\phi$  being incremental angle rotations of radius  $\frac{h}{2}$ .

The process begins with drawing a semi-circle with radius =  $\frac{h}{2}$  as seen in Figure 4.18.

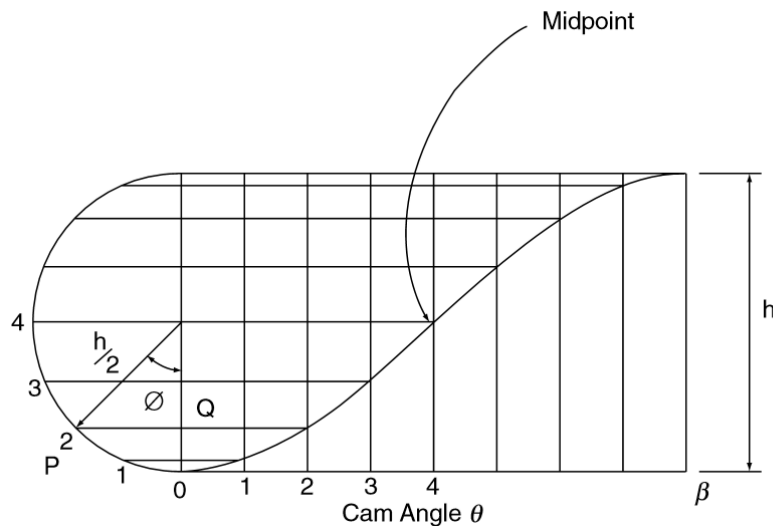


**Figure 4.18: Simple harmonic cam rise curve (Rothbart, 2004)**

This is drawn against the y axis and the cam angle  $\theta$  along the x axis. The x axis is divided into  $i$  number of increments and lines drawn vertically from their x position. The semi-circle is divided into  $i$  number of sections each with angle  $\phi = \frac{\pi}{i}$ . Lines are then drawn horizontally from these points along the arc.

The relationship between the generating circle and the cam angle,  $\theta$  is shown by

$$\frac{\phi}{\theta} = \frac{\pi}{\beta} \quad (4.31)$$

The intersecting points of the horizontal lines and corresponding vertical cam angle lines are marked. These intersecting points are connected to make the follower displacement curve shown in Figure 4.18.

Substituting Equation (4.31) into Equation (4.30) gives the follower displacement curve

$$y = \frac{h}{2} \left( 1 - \cos \left( \frac{\pi\theta}{\beta} \right) \right) \quad (4.32)$$

Equation (4.32) can be converted to displacement versus time using the relationship

$$\theta(t) = \omega t \quad (4.33)$$

Here  $\omega$  is the rotational speed of the cam in radians per second. Substituting Equation (4.33) into (4.32) gives

$$y(t) = \frac{h}{2} \left( 1 - \cos \left( \frac{\pi\omega t}{\beta} \right) \right) \quad (4.34)$$

The follower velocity and acceleration curves were derived from Equation (4.34) and are shown in Equation (4.35) and (4.36).

$$y'(t) = \frac{\pi\omega h}{2\beta} \sin \left( \frac{\pi\omega t}{\beta} \right) \quad (4.35)$$

$$y''(t) = \frac{\pi^2\omega^2 h}{2\beta^2} \cos \left( \frac{\pi\omega t}{\beta} \right) \quad (4.36)$$

The use of a simple harmonic curve enables the use of smaller cams and has a reduced follower jerk in comparison to the linear and parabolic curves (Rothbart, 2004).

The first step in designing cam systems is to determine the desired operating speed. This influences the choice of the cam profile and type of follower used.

It is recommended to keep the cam design as small as possible to reduce the sliding speed between the cam and follower. A larger cam has a larger outer tangential velocity in comparison to that of a smaller cam for the same rotational speed (Rothbart, 2004).

The cam and follower contact point experiences high forces during operation and as a result both components should be designed from materials capable of withstanding these forces. The forces experienced by the cam include impact forces and surface abrasion forces. To prolong the life of the cam, materials are used which can be hardened after the cam profile is machined (Rothbart, 2004).

The phenomena known as wear occurs between two surfaces in contact with one another. Wear causes removal of material from a component's surface. Cam-follower systems experience four kinds of wear during operation; adhesive wear, abrasive wear, corrosive wear and surface fatigue wear (Rothbart, 2004).

Adhesive wear, otherwise known as galling, occurs during the sliding between two solid surfaces. It is a result of attraction between the material's surface atoms and leads to material transfer from the one surface to the other. In a cam-follower mechanism this can lead to irregularities in the cam profile causing undesirable bounce of the follower.

The amount of adhesive wear is directly influenced by the surface condition and the material combinations. For instance, cast iron and phosphor bronze are a good combination whereas hardened steel and hardened bronze are not (Rothbart, 2004).

Abrasive wear occurs between two surfaces if they have considerably different hardness's. Small particles of the harder material grind along the surface of the softer material which causes material removal. This can also occur from hard particles found within the cam-follower surroundings such as dust and other contaminants. Therefore, lubrication in cam-follower systems is imperative as it removes these abrasive particles from the contacting surfaces (Rothbart, 2004).

Lubricant oils used in cam-follower systems also prevent surface corrosion of the parts. Oxidising of the material's surface loosens particles and these particles contribute to the abrasive wear between the two surfaces.

Surface fatigue is commonly found in rolling elements exposed to repetitive loading. Variables such as speed, temperature, load, material and surface geometry all influence the degree of fatigue in the component. Rolling element fatigue differs from previously discussed mechanisms as it can originate from below the material's surface (Rothbart, 2004).

#### 4.2.2 Cam Follower Designs

Cam followers are classified according to their motion and contacting surface with the cam. Follower motion types include translation, oscillation and indexing. Follower surface types include knife-edge, curved, flat or roller and are chosen depending on the required application. The way in which the follower is constrained to the cam surface is either positive driven in which rollers move within a cam groove, spring-loaded to the surface or held to the cam surface by gravity (Rothbart, 2004). Again, these can be chosen depending on the desired application.

A knife edge follower, as the name suggests, is a follower with a sharp point in contact with the cam surface. This follower is seen in Figure 4.19 (a). These followers are the simplest to manufacture, however are impractical as the sharp point results in high contact stresses and excessive wear between the follower point and cam.

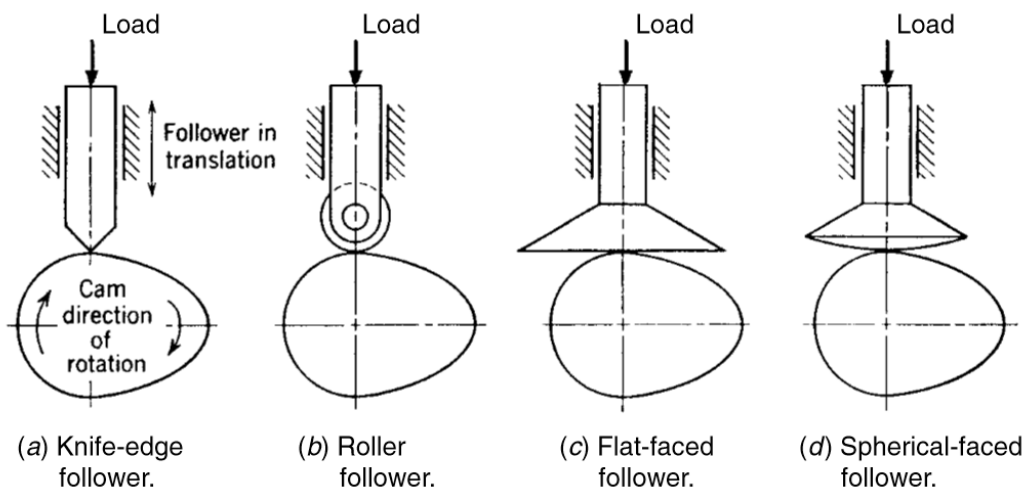


**Figure 4.19: Cam follower types (Rothbart, 2004)**

A more practical follower is the roller follower presented in Figure 4.19 (b), which utilises a ball or needle bearing that rolls along the cam surface and transfers the profile motion to the follower arm. This type of follower has the lowest friction coefficient of all follower designs as it relies on rolling motion in place of sliding motion (Rothbart, 2004).

Figure 4.19 (c) and (d) show lesser used follower geometries which like the knife-edge follower rely solely on sliding along the cam surface. These have been found to have less wear than the knife-edge follower but suffer in accurately translating the cam profile motion to the follower (Rothbart, 2004).

Another design consideration is the maximum angle between the cam profile normal and the follower motion during the rise period. This is known as the pressure angle and is shown in Figure 4.20.

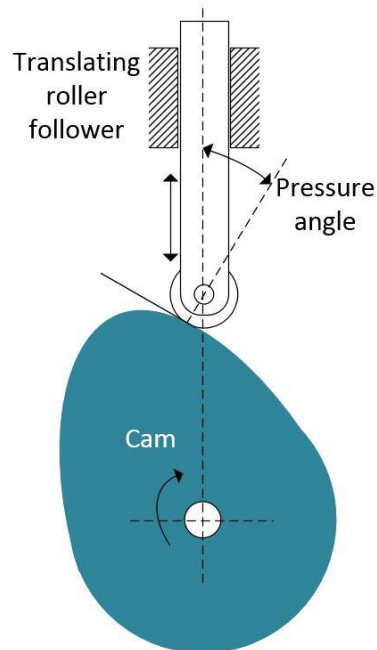


**Figure 4.20: Cam follower pressure angle**

This angle is dependent on the type of cam profile curve used and required lift  $h$ . For larger pressure angles the tangential force experienced by the follower increases. This can reduce the smoothness of the follower operation and cause excessive wear and fatigue of the cam-follower mechanism. As a result, when designing cam follower systems, the pressure angle should be kept to a minimum to reduce cam power consumption and wear.

A general guideline for pressure angle design gives a safety limit of 30 degrees (Rothbart, 2004). Pressure angles as high as 48 degrees have been successfully used for light load application with low friction roller followers (Rothbart, 2004). Jamming occurs when pressure angles are too large and the translating follower locks in its guide due to excessive frictional forces. For applications requiring steep cam profiles an oscillating follower is preferred as it is less prone to jamming.



An oscillating roller follower consists of a needle or ball bearing follower and an oscillating arm as shown in Figure 4.21. The oscillating arm, more commonly known as rocker, pivots about an axially located support. Oscillating followers can operate at higher pressure angles than translating followers which allows the use of smaller cams (Rothbart, 2004).

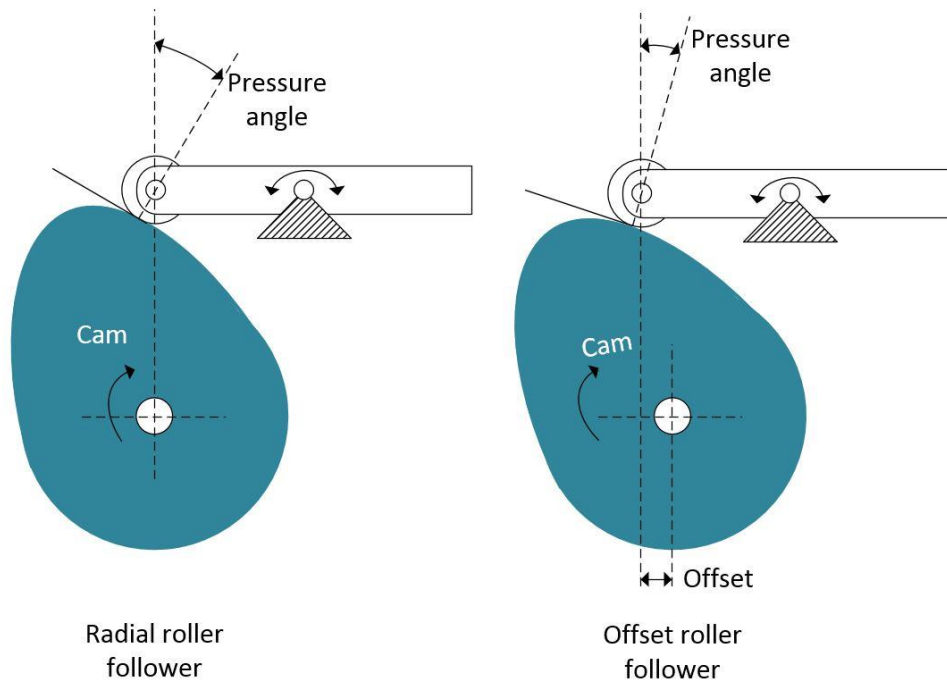


**Figure 4.21: Radial vs offset oscillating roller follower**

A way to reduce the apparent pressure angle experienced by the follower is to offset the follower position in the direction which opposes the cam rotation (Oberg, et al., 1975). Figure 4.21 shows a radial follower compared to an offset follower for the same cam profile. The radial follower's line of motion passes through the centre of the cam. By offsetting the position of the follower, the pressure angle is significantly reduced. This allows the use of steeper cam profiles without having excessive tangential forces on the follower.

The rocker should be designed as light as possible to reduce its moment of inertia. If the moment of inertia is too large, the follower will ramp off the cam surface at the point where the maximum negative acceleration is experienced (Rothbart, 2004). The torque,  $\tau$ , required to keep an oscillating follower in contact with the cam is given by

$$\tau = I\alpha \quad (4.37)$$

for an angular acceleration,  $\alpha$ , and moment of inertia,  $I$ , about the oscillating follower's pivot point.

### 4.2.3 Torsion Spring Design

Helical torsion springs differ from the previously discussed compression springs by the motion of the force they apply. Compression springs apply a translational force whereas torsion springs are used for applications which require a torsional force.

Torsional springs exist as two main types, single bodied and double bodied springs as seen in Figure 4.22. Torsion springs are often coiled around a shaft and mounted in at least 3 places (Elkon, 1987). They come in a wide variety of end configurations depending on the desired application. All these springs are of the close-wound type which means no gaps exist between the coils. The pitch length then is simply equal to the wire diameter  $d$ .

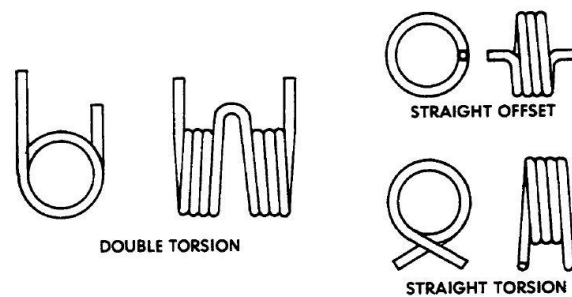


**Figure 4.22: Double vs single bodied torsion springs (Elkon, 1987)**

The number of active coils in a helical torsion spring,  $N_a$ , is a summation of the number of body turns,  $N_b$ , plus an equivalent amount of turns,  $N_e$ , due to the spring ends (Elkon, 1987). This is determined using

$$N_e = \frac{L_1 + L_2}{3\pi D} \quad (4.38)$$

with  $L_1$  and  $L_2$  being the length of the moment arm at the first and second ends respectively. From this,  $N_a$  can be determined from

$$N_a = N_b + N_e \quad (4.39)$$

As torque is applied to a torsion spring the body diameter of the spring decreases. This should be taken into consideration during design to ensure clearance between the spring body and central shaft is maintained. The mean diameter,  $D$ ,

of a torsion spring when deflected by  $\theta_{\text{rev}}$  revolutions with an initial mean diameter,  $D_1$  is given by

$$D = \frac{D_1 N_b}{N_b + \theta_{\text{rev}}} \quad (4.40)$$

The length of a close-wound helical torsion spring is

$$L_{\text{torsion}} = d(N_b + 1 + \theta_{\text{rev}}) \quad (4.41)$$

for a torsional deflection of  $\theta_{\text{rev}}$  revolutions. This equation shows that the length of the spring increases as the angular deflection is increased due to the reduction in coil diameter (Elkon, 1987).

The spring rate,  $k$ , of a torsion spring is defined as the torque,  $\tau$ , per revolution,  $\theta_{\text{rev}}$ , and is given by

$$k = \frac{\tau}{\theta_{\text{rev}}} = \frac{E d^4}{10.8 D N_a} \quad (4.42)$$

for a spring with Modulus of Elasticity,  $E$ , wire diameter,  $d$ , mean coil diameter,  $D$ , and number of active turns,  $N_a$ . The spring rate of a double bodied torsion spring can be determined by summing the rates of its individual components (Elkon, 1987).

Torsion springs, like compression springs, are subject to the phenomena of resonance. The natural frequency  $n$  of a torsion spring for the case of one end being fixed is determined by

$$n = \frac{d}{8\pi D^2 N_a} \sqrt{\frac{Eg}{\rho}} \quad (4.43)$$

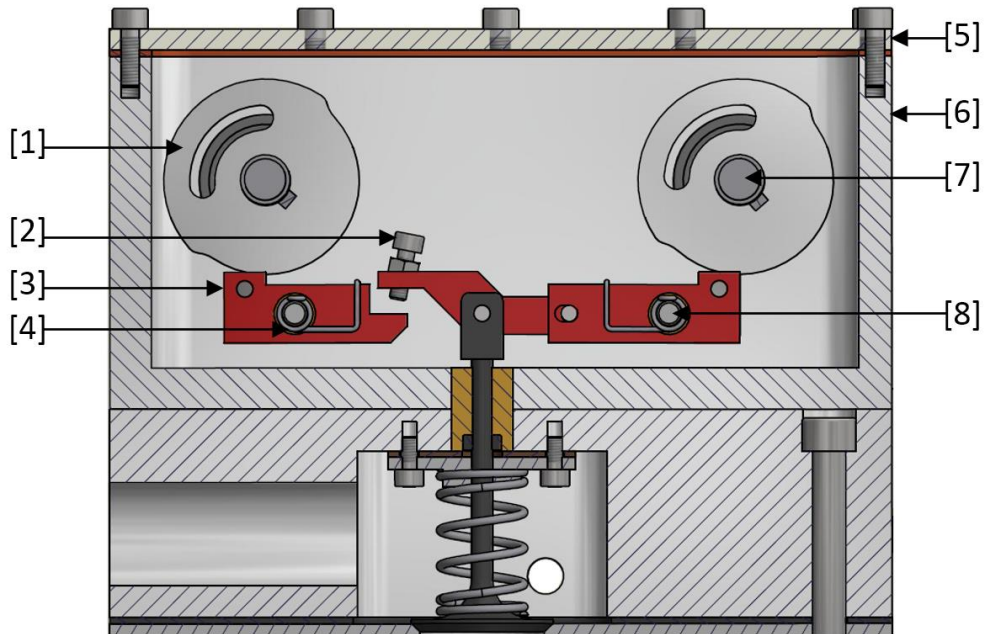
The operating frequency should be kept significantly lower than the spring's natural frequency. Pre-tensioning the spring is one way in which this phenomenon can be minimized (Elkon, 1987).

#### 4.2.4 Modified Caprotti Valve Gear Design

A variable valve duration cam system was designed to have a varying cut-off ratio from 15 % to 90 %. The valve lift was chosen as 2 mm and the engine operating speed as 500 rpm. As seen in Section 4.2.1, the acceleration experienced by the cam follower increases with higher valve lift/cam rise and higher engine speeds.

As such, the valve lift was chosen to minimise the experienced acceleration whilst still allowing sufficient filling of the cylinder.

The cam-follower system shown in Figure 4.23 was designed and manufactured for the developed engine. The followers were offset from the cam's radial line for reasons previously discussed in Section 4.2.2.



[1]: Cam	[5] Tappet cover
[2]: Clearance adjuster screw	[6]: Cam Housing
[3]: Rocker	[7]: Cam shaft
[4]: Rocker Torsion spring	[8]: Rocker pivot support

**Figure 4.23: Cam-follower assembly**

The linkage system shown in Figure 4.23 was designed to only lift the valve when both cams are actuating their respective rocker. This was done by introducing the clearance gap which was adjusted by the adjuster screw as seen in Figure 4.23 [2].

Both cams are powered by the output shaft and have the same rotational speed. The valve actuation is described by Figure 4.24 - Figure 4.27. The first stage is where both cams are in their base radius region. This is shown by Figure 4.24 where the valve is closed.

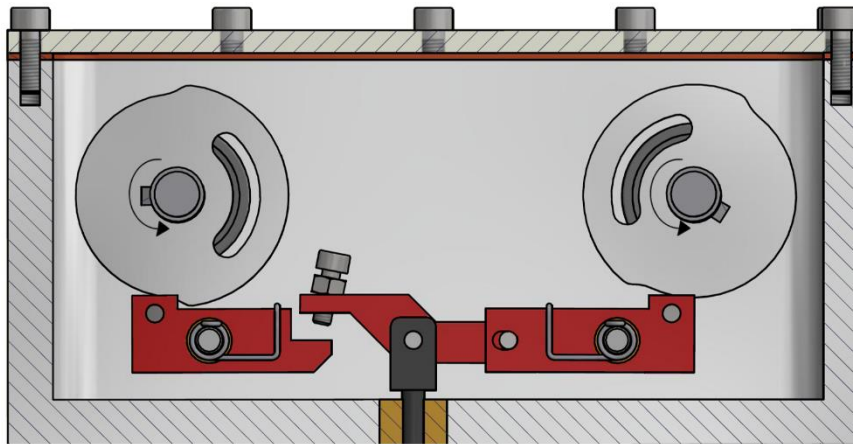


**Figure 4.24: Valve closed, both rockers not actuated**

The next stage is shown by Figure 4.25. The right rocker is actuated which is indicated by the white arrow. This in turn closes the clearance gap between the adjuster screw and the left rocker.

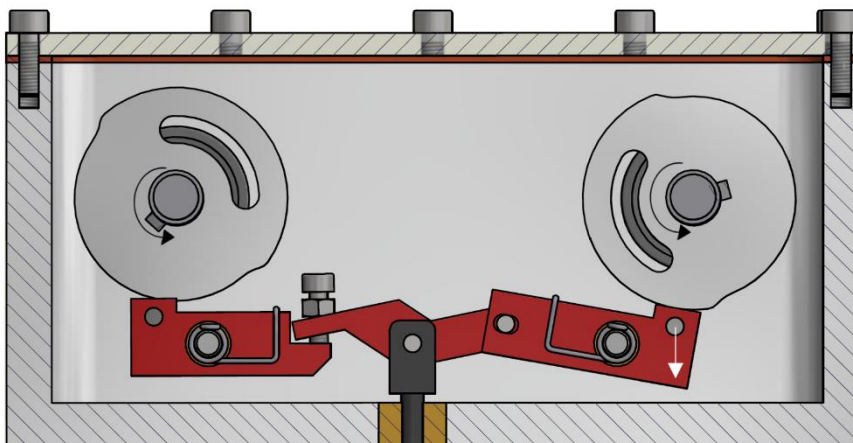


**Figure 4.25: Valve closed, right rocker actuated**

The valve is then opened when the left rocker is actuated as shown in Figure 4.26. The left rocker would have to lift the centre linkage by twice the size of the desired valve lift. To reduce the required cam lift,  $h$ , the rockers were designed with a 1-2 pivot ratio.

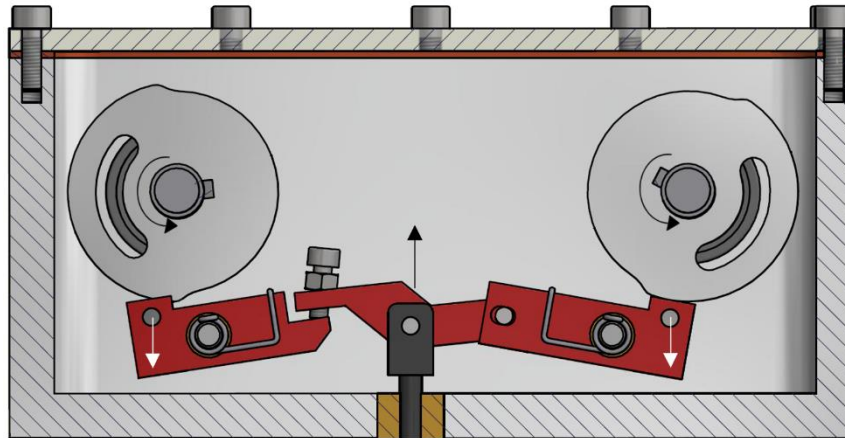


**Figure 4.26: Valve opened, both rockers actuated**

The closing of the valve is shown by Figure 4.27. The right rocker is no longer actuated which closes the valve once again. The valve closes due to it being spring loaded and that there is no longer any lifting force from the rockers.

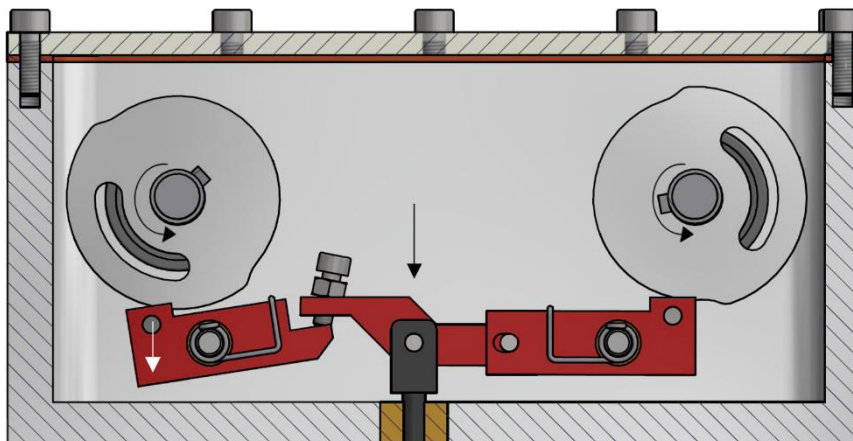


**Figure 4.27: Valve closed, right rocker not actuated**

The valve duration can be increased by shifting the right cam's phase relative to the left cam in the clockwise direction. This results in a longer period for which both cams are in their actuating region. The mechanism used to vary the cam phasing is discussed in Section 4.2.7.

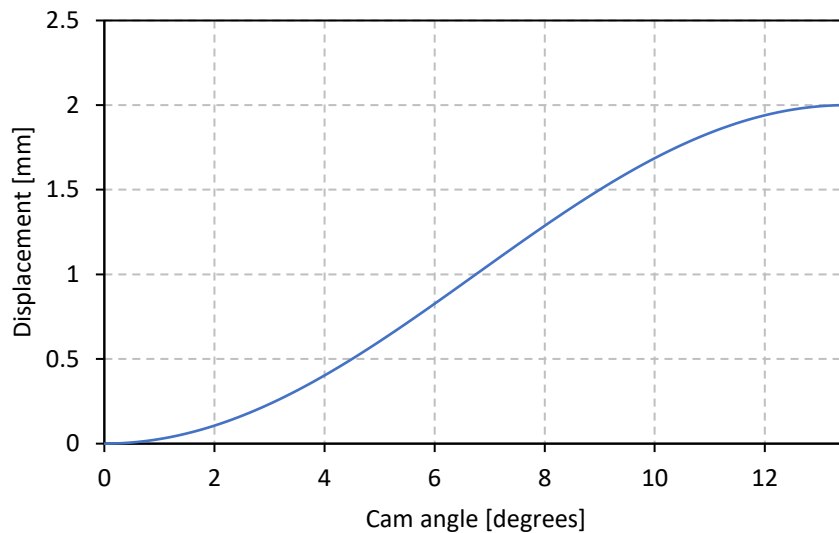
#### 4.2.5 Manufactured Cams

Both cam profiles were designed using the simple harmonic curve presented in Section 4.2.1. The cam lift,  $h$ , was designed to be 2 mm.

The cams were designed to have a dwell period of 45 % of a full revolution. The cams had a 3.75 % rise period and a 3.75 % return period. The size of the rise and return periods were designed according to the minimum required CR of 15 %.

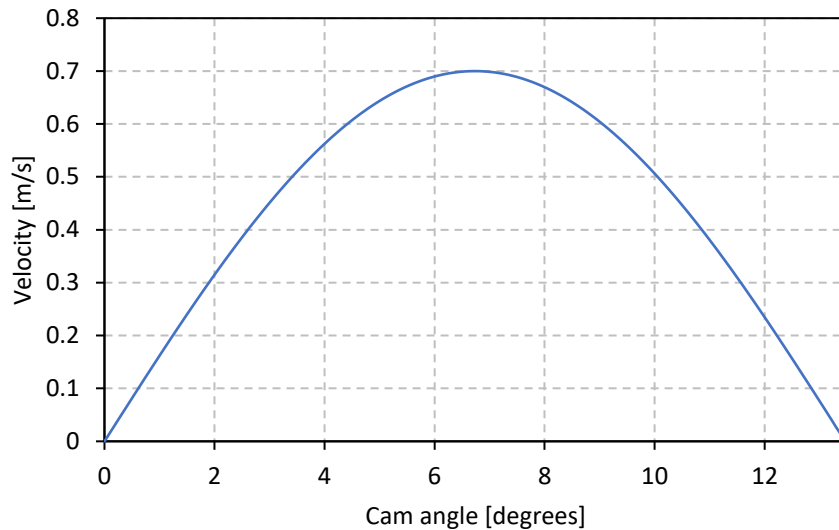
Both cams were water cut from K110 tool steel. These parts were then hardened in a vacuum furnace to 61 HRC. To reduce vibration during operation, the cams were designed with a slot on the lobed side for balancing.

Figure 4.28 shows the follower displacement curve of the cam rise period. The rise period  $\beta$  is 13.5 degrees.



**Figure 4.28: Follower displacement curve during rise period**

The follower velocity curve versus cam angle is shown in Figure 4.29. The maximum velocity is experienced half way during the rise period at  $\theta = 6.75^\circ$ . The velocity here is equal to  $0.7 \text{ m}\cdot\text{s}^{-1}$ . This maximum velocity was used for valve seal selection in Appendix A.1.



**Figure 4.29: Follower velocity during rise period**

The follower acceleration versus cam angle is shown in Figure 4.30. The maximum positive acceleration is experienced at the start of the rise period and is equal to  $489.94 \text{ m}\cdot\text{s}^{-2}$ . The maximum negative follower acceleration occurs at the end of the rise period and is equal to  $-489.94 \text{ m}\cdot\text{s}^{-2}$ . The maximum acceleration points were later used in Section 4.2.6 for the rocker spring design and rocker force calculations.

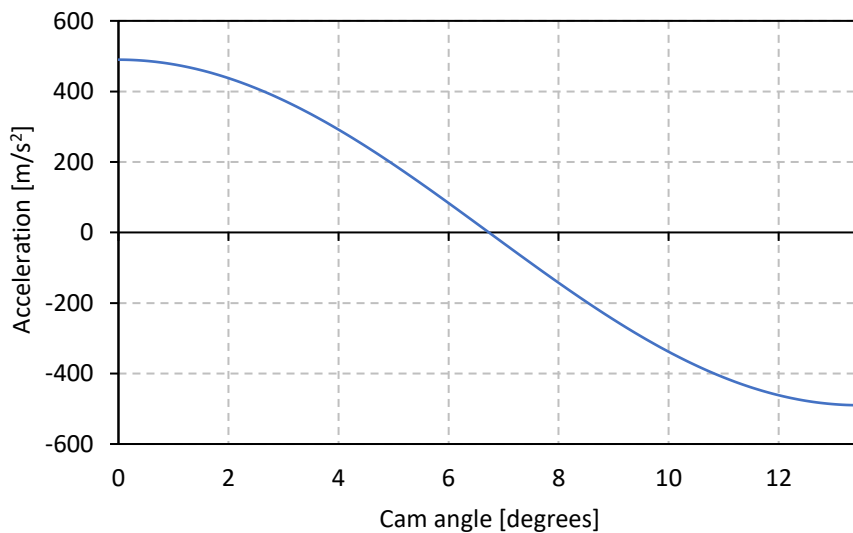
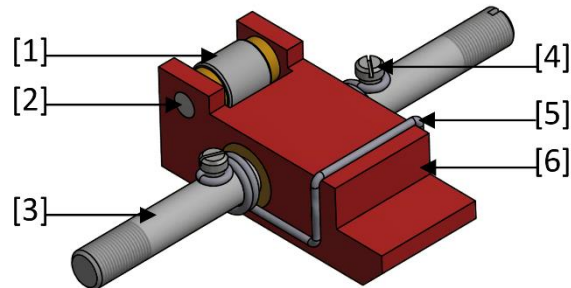


**Figure 4.30: Follower acceleration during rise period**



#### 4.2.6 Manufactured Rockers

Two rockers were manufactured from grade 7 aluminium. This material was chosen to reduce the components mass while still maintaining sufficient strength. The rocker assembly is shown in Figure 4.31.



[1]: Drawn cup needle bearing	[4] M3 screws
[2]: 4mm Dowel Pin	[5]: Rocker Torsion Spring
[3]: Rod support	[6]: Rocker Body

**Figure 4.31: Rocker assembly**

The rocker assembly comprised of an aluminium 7075 rocker body which pivoted about a silver steel rod support. A drawn cup needle bearing was used as the roller follower which ran along the cam surface. A torsional spring was used to ensure the roller follower was kept in contact with the cam during operation. The torsional spring was held onto the rod support by two M3 screws.

The moment of inertia of the rocker assembly about the pivot point was 11.014 kg·mm<sup>2</sup> which was attained from the CAD geometry in Autodesk Inventor 2016. The maximum negative acceleration experienced by the roller was determined as explained in Section 4.2.5. This was converted into angular acceleration,  $\alpha$ , of the rocker using the moment arm distance from the roller to the pivot support.

The angular acceleration and moment of inertia of the rocker were used in Equation (4.37) to determine the required torque from the torsional spring to keep the roller from leaving the cam surface. The required spring torsion was calculated to be 0.49 Nm.

The torsion springs were designed with a spring stiffness of 1.89 N·m per revolution. The rockers were preloaded against the cams with a torque of 0.5 N.m.

The maximum force experienced by the needle bearing occurs at the start of the cam rise. Here the valve is completely closed and requires a force to lift against the higher pressure within the steam chest.

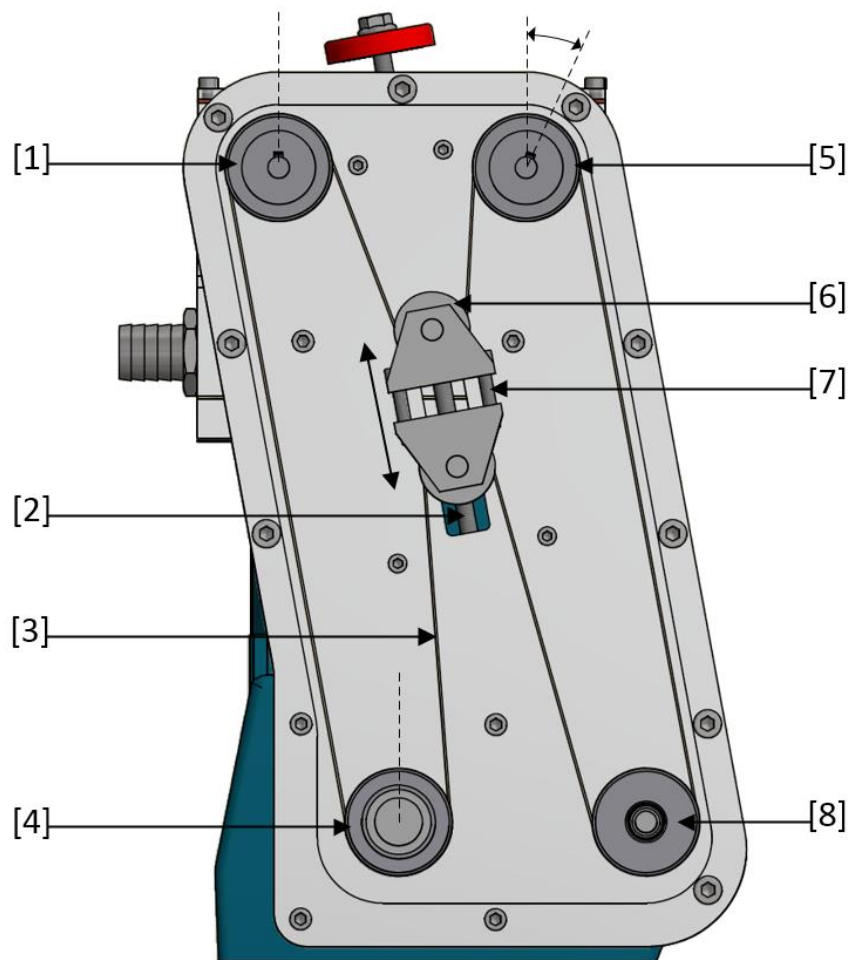
The maximum acceleration is experienced during the start of the rise period which also adds a force component on the needle bearing. The preloading of the torsional spring and valve spring also adds to the force experienced. The combination of the static and dynamic forces resulted in a force of 317.88 N on the bearing (Appendix C.2). The HK0408 needle bearing used had a dynamic load rating of 1.76 kN (Appendix C.2, C-1). This resulted in a safety factor of 5.38.

The maximum stress in the silver steel support rod was calculated to be 203.62 MPa. This resulted in a safety factor of 3.68 (Appendix C.2).

#### **4.2.7 Cam Phasing System**

As previously discussed, the valve duration can be varied by shifting the right cam's phase relative to the left's. This was performed by the belt system shown in Figure 4.32.

The belt system shown consists of two cam pulleys, Figure 4.32 [1 and 5], which are driven by a pulley on the engine's output shaft, Figure 4.32 [4]. The phase of the right cam was controlled by shifting the roller assembly up or down as indicated by the arrows in Figure 4.32. This allowed the phasing to be changed without affecting the belt tension or the valve timing. The belt was tensioned by tightening the tensioner bolts, Figure 4.32 [7], which pulled the two rollers, Figure 4.32 [6], closer to one another.



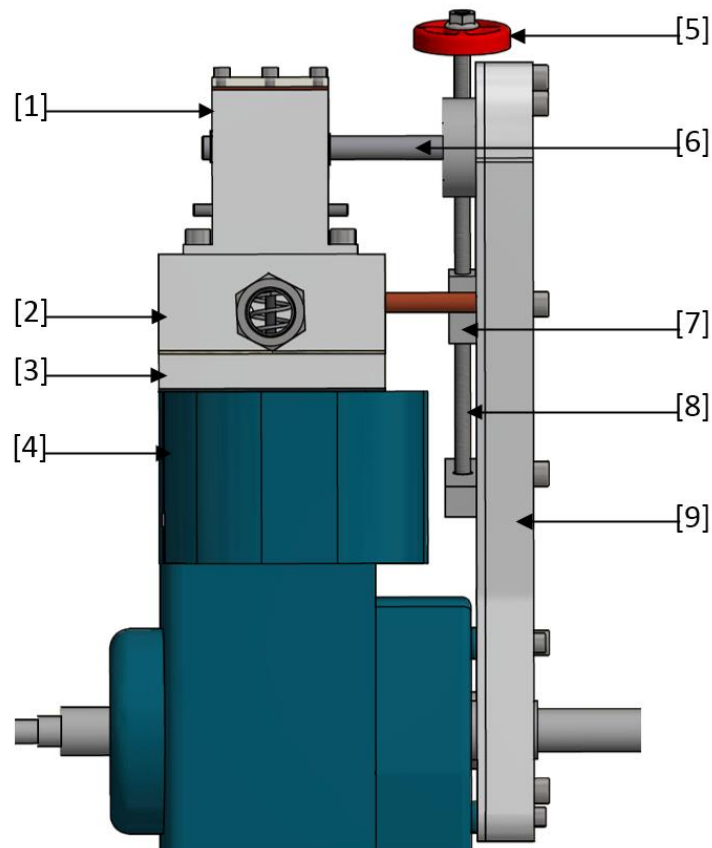
[1]: Left camshaft pulley	[5]: Right camshaft pulley
[2]: Threaded rod	[6]: Rollers
[3]: T5x10 Timing belt	[7]: Belt tensioner bolts
[4]: Output shaft pulley	[8]: Free spinning pulley

**Figure 4.32: Cam phasing system**

A timing belt was used to prevent a shift in valve timing. Valve timing refers to the precise time at which the valve is opened and not the duration it is open for. The left cam is always kept in phase with the output shaft such that the valve is opened at TDC. The duration for which the valve stays open is controlled by the phase of the right cam.

The maximum force experienced by the belt was calculated to be 298 N (Appendix C.3). A T5x10mm polyurethane belt was used which could withstand a tension of 480 N.

Figure 4.33 shows a side view of the belt system attached to the engine. The top roller bracket was machined with a threaded hole in its back extrusion, Figure 4.33 [7]. By turning the adjuster handle, Figure 4.33 [5], the bracket moved up and down the threaded rod, Figure 4.33 [8], which varied the cam phasing and thus valve duration.



[1]: Cam housing	[5]: Adjuster handle
[2]: Steam chest	[6]: Camshaft
[3]: Cylinder spacer	[7]: Top roller bracket
[4]: Engine	[8]: Threaded rod
	[9]: Belt housing

**Figure 4.33: Cam phasing system side view**

### 4.3 Engine Flywheel Redesign

Preliminary test runs were performed on the engine to ensure correct operation of the engine and test equipment. The findings of these tests were that the engine was not able to operate at speeds lower than approximately 1500 rpm. This was due to the engine's flywheel which did not have sufficient inertia to keep the engine self-sustaining at lower engine speeds.

The flywheel used was the engine's original flywheel which had a mass of 4.6 kg and diameter of 206 mm. This correlated to a moment of inertia of 25507 kg·mm<sup>2</sup> obtained from Autodesk Inventor. The kinetic energy of a flywheel can be calculated using

$$E_{\text{flywheel}} = \frac{1}{2}I\omega^2 \quad (4.44)$$

with a moment of inertia,  $I$ , and rotational speed of  $\omega$  in radians per second (Budynas & Nisbett, 2008).

The existing flywheel would have a momentum energy of 34.97 Joules when operating at 500 rpm. From tests it was found that the flywheel did not have sufficient energy to compress the remaining air in the cylinder on the piston upstroke. This resulted in the engine abruptly stopping when speeds were reduced below approximately 1500 rpm.

The energy required on the piston's upstroke was determined from the developed air thermodynamic calculations in Section 3.1. This was found to be 85.76 Joules for a single cycle. This is higher than the momentum energy of the flywheel which validates that the existing flywheel did not offer the inertia required to operate at the desired 500 rpm.

A new flywheel was designed and manufactured for the prototype engine. The designed flywheel was manufactured from 220 mm diameter EN19 steel rod. The flywheel was designed to have a moment of inertia of 65241.51 kg·mm<sup>2</sup>. This resulted in a momentum energy of 89.43 Joules at 500 rpm which is higher than the energy required during the piston's return stroke.

The engine's flywheel was replaced with the manufactured flywheel and formal tests performed following the procedure in Section 5.2.1.



## 5 Engine Testing

The converted engine shown in Figure 5.1 was tested on air for various cut-off ratios to determine the effect on the engine's output power and air consumption. An indicator sticker was placed on the belt housing which assisted the operator in setting the cut-off ratio.

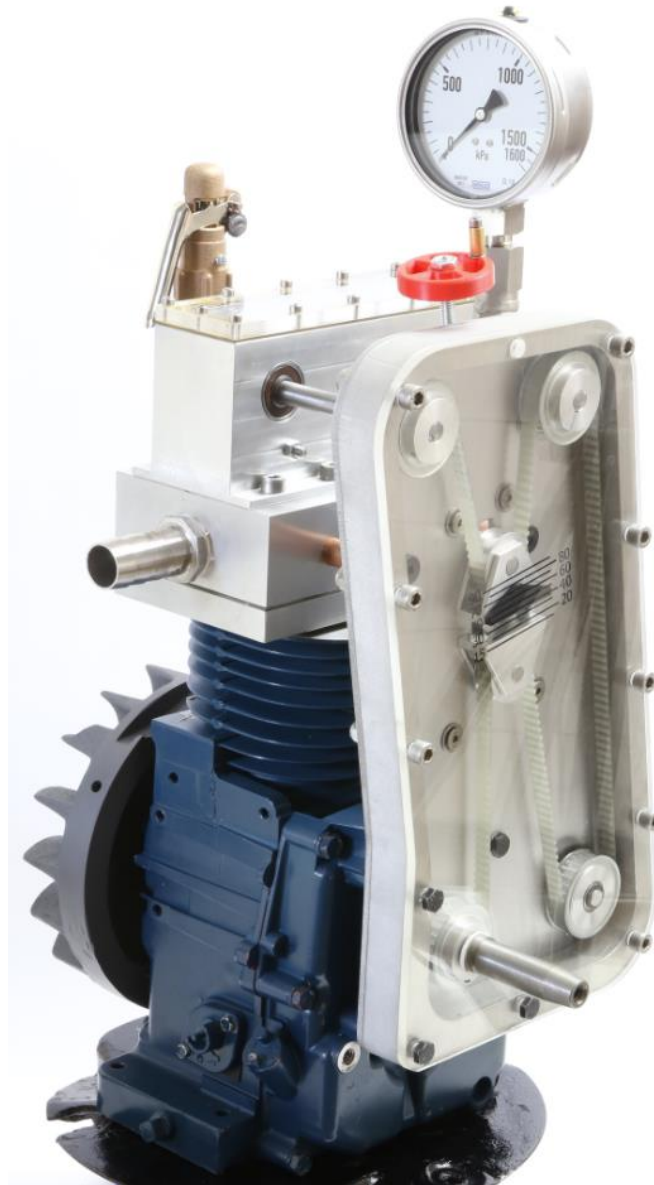
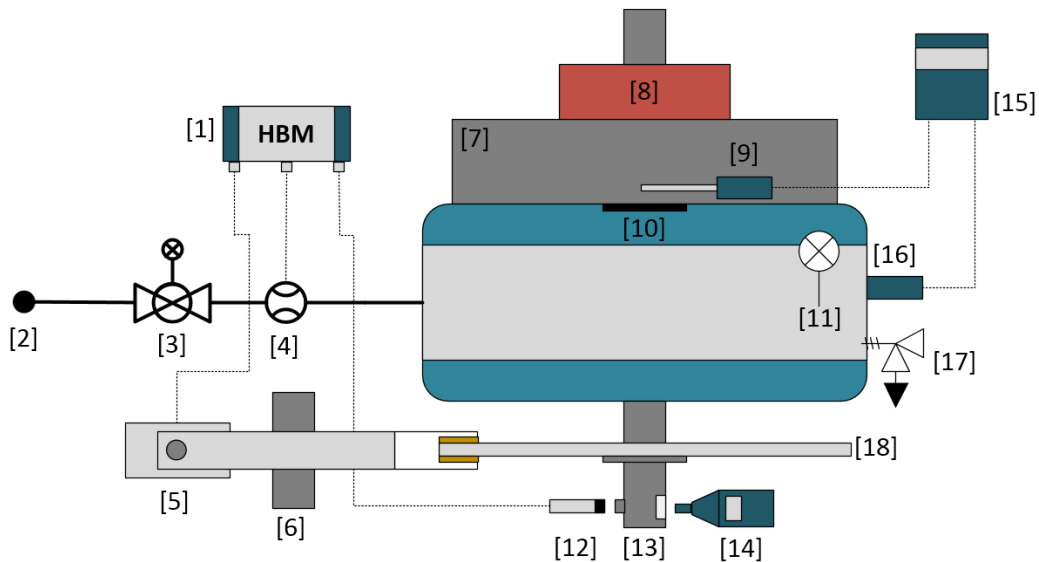


**Figure 5.1: Prototype uniflow steam engine assembly (old flywheel)**

## 5.1 Test Bench Design

A test bench system was designed to test the developed engine's power output at various cut-off ratios. A top view schematic of the test bench is shown in Figure 5.2. A pull start mechanism, Figure 5.2 [8], was implemented to aid in the starting of the engine. A metal housing, Figure 5.2 [7], was manufactured to encase the flywheel as a safe-guard.



[1]: Quantum data logger	[10]: Engine exhaust port
[2]: 10 bar absolute air supply	[11]: Steam chest pressure gauge
[3]: Festo pressure regulator	[12]: Omron inductive sensor
[4]: Festo MS6-SFE digital flow meter	[13]: Engine output shaft
[5]: HBM S2M 200 N load cell	[14]: Handheld tachometer
[6]: Brake pivot arm	[15]: Thermocouple reader
[7]: Flywheel housing	[16]: Inlet T-type thermocouple
[8]: Engine pull start	[17]: Pressure relief valve
[9]: Exhaust T-type thermocouple	[18]: Disk brake

**Figure 5.2: Prototype engine test setup top view schematic**

The output torque of the engine was measured using a disk brake system connected to a load cell. A disk brake was mounted to the output shaft of the engine and a brake calliper used to vary the braking force on the disk. The brake calliper was mounted on a pivot arm which had a load cell attached on the other end as presented in Figure 5.3.



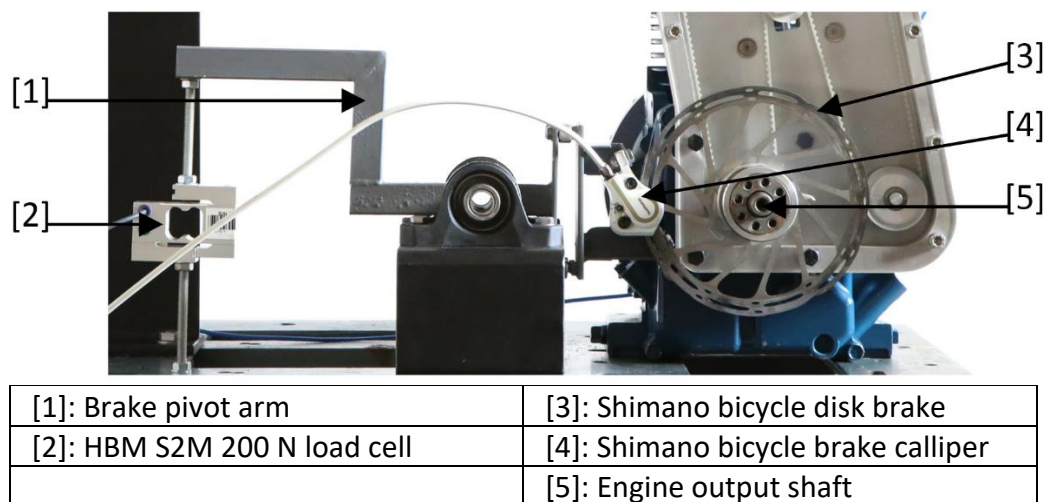


**Figure 5.3: Torque measuring system**

The braking torque on the engine was determined by taking the load cell reading and pivot arm moment length to determine the force experienced at the brake calliper. This force was then multiplied by the disk brake radius to calculate the torque experienced by the engine's output shaft.

The operating speed of the developed engine was measured using an Omron PNP inductive proximity sensor, Figure 5.2 [12]. A bolt head was mounted to the outer surface of the output shaft which would trigger the proximity sensor when it came in close proximity. Therefore, the frequency of passes could be measured and the shaft speed calculated in postprocessing.

The engine's speed was manually controlled using a cable brake lever attached to the brake calliper. A handheld tachometer was mounted near the output shaft to display the instantaneous shaft speed. Therefore, the engine braking force could be varied until the desired speed was reached.

A T-type thermocouple, Figure 5.2 [16], was mounted in the steam chest to measure the supply air temperature before it enters the engine cylinder. A second T-type thermocouple, Figure 5.2 [9], was mounted at the engine's exhaust port, Figure 5.2 [10], to measure the air temperature after expansion. These temperatures would be compared to the temperatures calculated by the air thermodynamic model.

The thermocouples were connected to a thermocouple reader which displayed the instantaneous temperature readings.

A Festo pressure regulator, Figure 5.2 [3], was used to regulate the air supply pressure to the engine. This was mounted upstream of the the Festo MS6-SFE hot-wire flow meter, Figure 5.2 [4], which was used to record the air flow rate to the engine. A mechanical pressure gauge was mounted to the steam chest to display the pressure within the steam chest during operation.

A HBM Quantum data logger was used to record the data from the load cell, flow meter and proximity sensor. The Quantum data was then stored on a laptop using HBM Catman 5.0 data acquisition software.

The engine's bottom end oil sump was filled with 1.3 litres of oil according to the engines operation manual, Appendix D.1. A TITAN GT1 synthetic 5W-40 oil was chosen for its ability to operate in low temperatures. Cooling of the bottom end was expected during testing as the air in the cylinder would drop in temperature from expansion.

The cam housing was filled with TITAN GT1 synthetic 5W-40 oil such that the contact between the follower needle bearings and cams were submerged. This was to lubricate the cam rolling surface as well as the brass bushings in the rockers.

## 5.2 Air Test

The developed engine was tested at Stellenbosch University on a 10 bar absolute air supply. The speed and torque output of the engine was measured to determine the output power. The engine was tested at cut-off ratios from 15 % to 90 % with each test performed at 500 rpm.

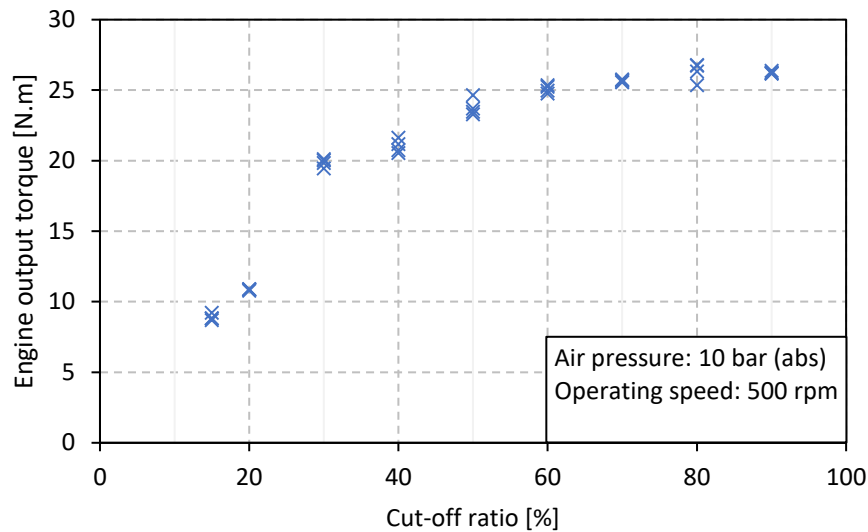
### 5.2.1 Procedure

1. Set the cut-off ratio using the adjuster handle, Figure 4.33 [5], to the desired position as indicated by the cut-off ratio indicator sticker
2. Rotate engine to just before TDC using indicator marks on the output pulley
3. Ensure the load cell, thermocouples, proximity sensor, tachometer and flow meter are operational
4. Ensure all pipe fittings are securely fastened
5. Put on ear and eye protection equipment
6. Open air supply at wall and adjust pressure regulator to 9 bar gauge
7. Start Quantum data logger and begin recording flow meter, load cell and proximity sensor readings
8. Start the engine using the pull start mechanism
9. Adjust the braking force until the handheld tachometer displays an operating speed of 500 rpm.
10. Operate engine at steady state for 20 seconds
11. Manually record thermocouple readings and steam chest pressure
12. Turn off air supply and allow engine to come to a standstill before approaching
13. Save experimental data
14. Repeat steps 1 to 13 for cut-off ratios from 15 % to 90 %

## 5.2.2 Results and Comparison to Model

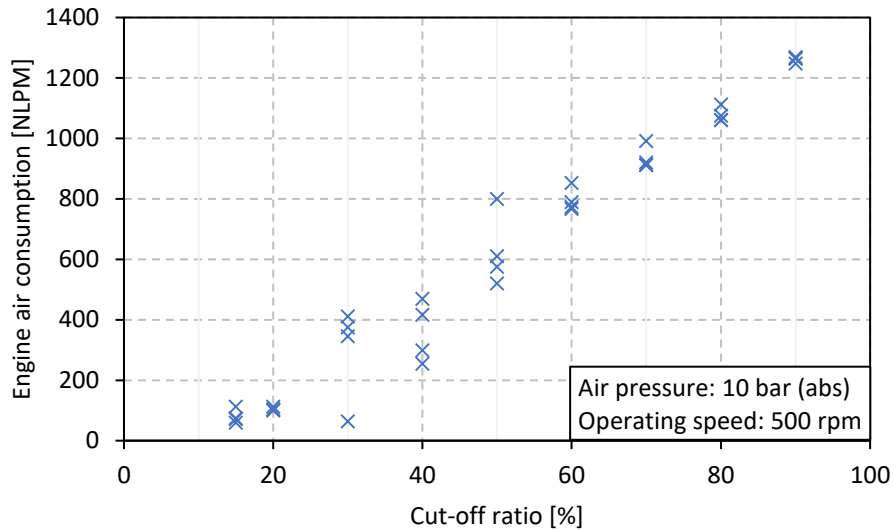
The following data was obtained from recording the steady state operation of the prototype engine. The steady state data was divided into four data points with each point averaged over 5 seconds.

Figure 5.4 presents the torque output obtained from the prototype engine tests at 500 rpm. The plot shows a logarithmic type trend of output torque versus the engine's cut-off ratio. The effect of the cut-off ratio on the output torque decreases as the cut-off ratio is increased. It can be seen that for cut-off ratios higher than 70 % there is a negligible change in output torque.



**Figure 5.4: Prototype engine output torque versus cut-off ratio at 500 rpm**

The air consumption of the engine was measured during testing at various cut-off ratios and is shown in Figure 5.5. The consumption is represented in Normal Litres Per Minute (NLPM) which is the equivalent air consumption at atmospheric conditions with a density of  $1.294 \text{ kg}\cdot\text{m}^{-3}$  according to the Festo flow meter manual, Appendix D.2.



**Figure 5.5: Prototype engine air consumption versus cut-off ratio at 500 rpm**

The largest data point outliers are seen at 30 % and 50 % cut-off ratios. The data shows a linear type relationship between the engine air consumption and cut-off ratio.

The engine speeds for each test are shown in Figure 5.6. These deviations from the desired 500 rpm are a result of the inaccuracies inherent in the engine braking test method.

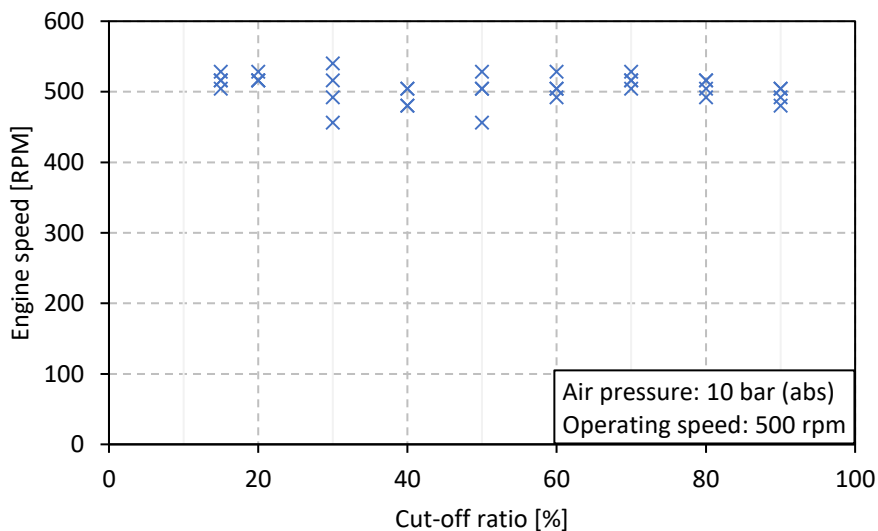


**Figure 5.6: Prototype engine speed versus cut-off ratio**

The temperatures at the inlet and exhaust of the piston expander were measured during the various CR tests. The measured inlet temperatures were input into the thermodynamic model and a theoretical exhaust air temperature determined. These results are shown in Table 2.

**Table 2: Measured exhaust air temperature versus the theoretical exhaust air temperature**

Cut-off ratio [%]	Measured inlet temperature [°C]	Measured exhaust temperature [°C]	Theoretical exhaust temperature [°C]
15	16.3	-27.3	-123.2
20	14.5	-27.4	-124.2
30	17.9	-27.6	-122.4
40	17.5	-26.2	-122.6
50	17.2	-25.8	-122.8
60	16.6	-24.7	-123.1
70	17	-24.5	-122.88
80	16.1	-24.8	-123.3
90	15.7	-23.3	-123.5

The large difference between the theoretical and measured exhaust air temperature comes from the model's assumption of isentropic adiabatic expansion. This assumes that no heat transfer to or from the air occurs during expansion. It is evident from the measured exhaust temperature that there is heat transfer occurring from the engine cylinder to the expanding air, resulting in a higher than expected exhaust temperature.

It is evident that the cut-off ratio has minimal to no influence on the exhaust temperature. The higher than expected exhaust temperature can also be attributed to the exhaust flow not being constant.

The air flow from the exhaust pulsates at the same frequency of engine oscillations. This pulsation allows for atmospheric air to be drawn near the exhaust thermocouple, thus influencing the measured temperature. The piston upstroke could cause a suction within the cylinder below the piston which would draw air at atmospheric conditions through the exhaust port and into the crank casing. This would have a large influence of the accuracy of the exhaust air temperature measurement.

The engine power output was calculated from the measured output torque and associated speed for all data points. This is shown in Figure 5.7.

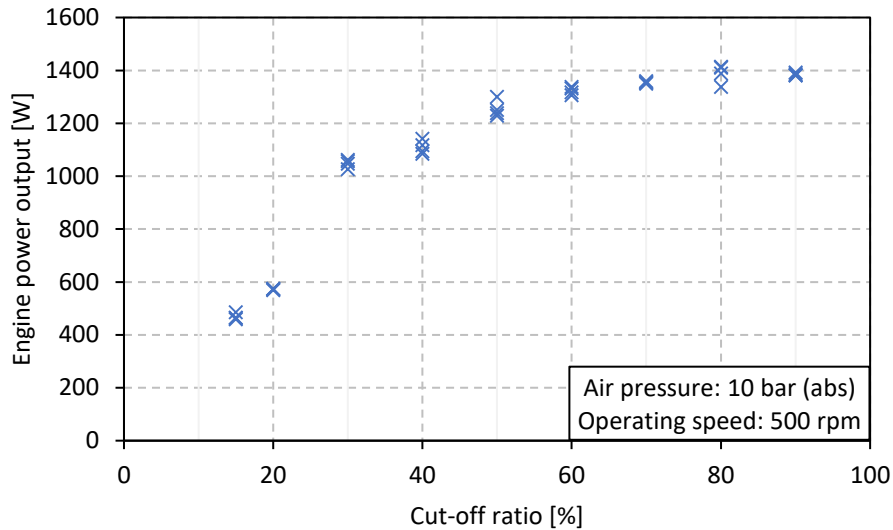


**Figure 5.7: Prototype engine power output versus cut-off ratio**

A logarithmic type trend is seen for the power output versus the cut-off ratio. The mean output power at each cut-off was calculated and plotted against the numerical power output shown in Figure 5.8.

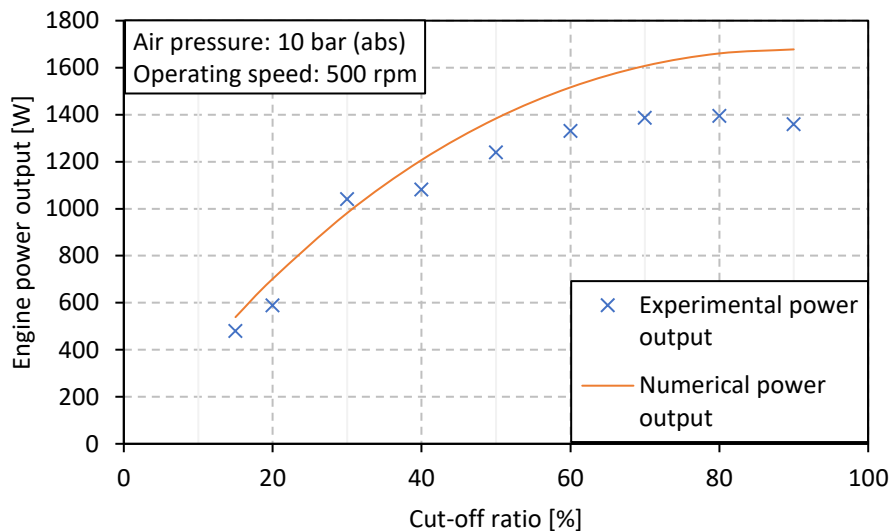


**Figure 5.8: Prototype engine experimental versus numerical power output**

The numerical power output curve was obtained from the air thermodynamic model for an operating speed of 500 rpm. The inlet temperatures measured during testing were used for the inlet air conditions in the thermodynamic model.

The experimental model follows a similar trend to that of the numerical model. The test at 30 % cut-off ratio is an outlier which can be attributed to the unsteady speed during that performed test as seen by Figure 5.8. The prototype engine delivered a maximum power output of 1.396 kW at 80 % cut-off ratio.

At 15 % cut-off ratio the experimental power output is 89 % of the numerically calculated power output. This drops down to 81.1 % at 90 % cut-off ratio. The difference between the experimental and numerical results can be attributed to the mechanical losses in the system which the thermodynamic model neglects.

The error between the experimental and numerical results in Figure 5.8 increases with increase in cut-off ratio. It was hypothesized that at larger cut-off ratios the air in the cylinder is not sufficiently exhausted which would result in a higher terminal compression pressure. This in turn would require more work from the engine during the upstroke of the piston and thus a lower output power is achieved. This effect on power output is seen to increase with larger cut-off ratios as exhaustion of more air is required for the same exhaust period.

The mean experimental air consumption at each cut-off ratio was calculated and plotted against the numerical air consumption shown by Figure 5.9

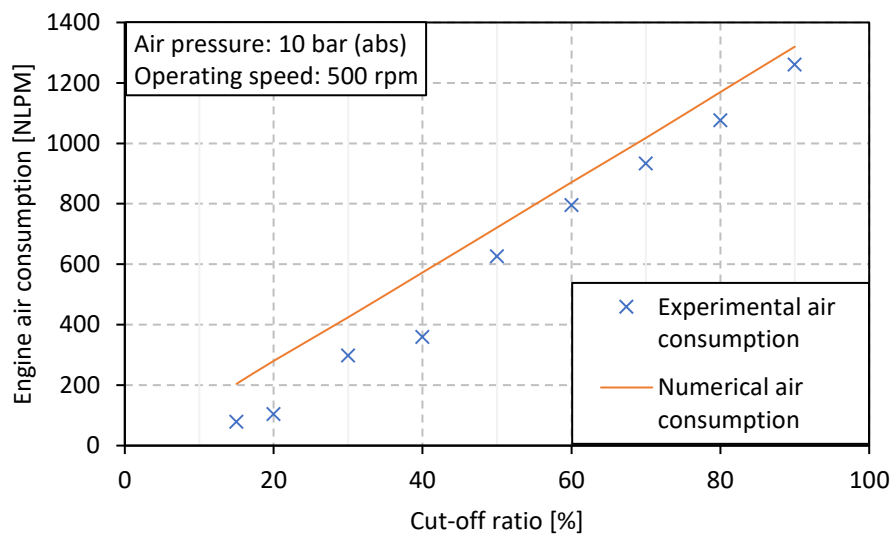


**Figure 5.9: Prototype engine experimental versus numerical air consumption**

The experimental results show a strong correlation with the numerically determined air consumption. The experimental results show a linear increase in air consumption with increase in cut-off ratio as predicted by the thermodynamic model. The numerical results overpredicted the air consumption for all cut-off ratios.



The largest error is at 15 % cut-off ratio where the experimental result deviates from the numerical result by 61 %. This error gradually decreases as the cut-off ratio is increased until a minimum error of 4.43 % is seen at 90 % CR.

The difference between the numerical and experimental air consumption can be attributed to the assumption made in the thermodynamic model that the opening and closing of the inlet valve occurs instantaneously. In reality there is an opening and closing period where the valve is not completely open. This is a fixed period which is dependent on the operating speed and cam profile. Figure 5.10 shows the valve lift versus time curves for smaller and larger cut-off ratios.

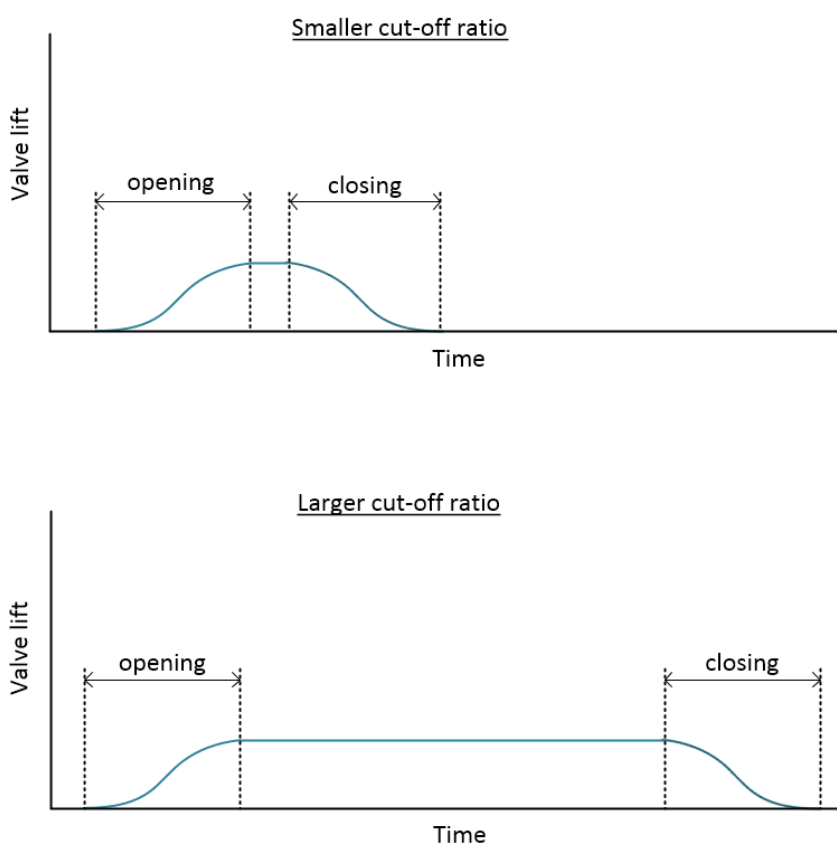


**Figure 5.10: Valve lift schematic showing the effect of cut-off ratio on the overall percentage of opening and closing events**

At lower cut-off ratios, the opening and closing period form a larger percentage of the total valve actuation than at higher cut-off ratios. This could explain the larger errors evident at lower cut-off ratios. At higher cut-off ratios the opening and closing period form a smaller percentage of the total valve actuation as the dwell is longer. Therefore, the experimental results at higher cut-off ratios in Figure 5.9 show a better correlation to the thermodynamic model's assumption of instantaneous opening and closing events.



## 6 Conclusions

The following chapter focusses on the outcomes of the undertaken project. The original objectives are discussed, and their execution evaluated. A section is dedicated to the recommendations for future work on the development of a piston expander for use in small-scale CSP plants.

### 6.1 Objectives

#### **6.1.1 Develop a Thermodynamic Model of a Reciprocating Steam Engine Cycle:**

A thermodynamic model was developed for a uniflow engine cycle for the operation on air as well as steam. The air model was developed for comparison to the prototype engine tests on air. Both models determined the power output and consumption of the engine at various cut-off ratios.

#### **6.1.2 Design and Manufacture a Proof of Concept Variable Valve Duration Reciprocating Piston Expander from an Existing ICE:**

A single cylinder internal combustion engine was acquired for conversion into a proof of concept reciprocating steam engine. The original cylinder head was removed, and an exhaust port machined into the cylinder at the last 10 % of the piston stroke.

An inlet valve was designed and manufactured for the engine. A variable valve duration system was designed and manufactured for the prototype engine. The developed prototype engine operated successfully. A larger flywheel was designed and manufactured to allow for operation at the design speed of 500 rpm.

#### **6.1.3 Perform Tests on the Developed Prototype Engine at Various Cut-Off Ratios to Determine the Effect on Power Output and Air Consumption:**

A test bench was designed and manufactured for the testing of the prototype engine. A disk brake system was implemented to measure the torque on the output shaft of the engine. A proximity sensor was used to measure the speed of the output shaft.

The developed prototype engine was tested on a 9-bar gauge air supply. Tests were performed at cut-off ratios from 15 % to 90 %.

#### **6.1.4 Evaluate the Performance of the Constructed Engine and Compare to Thermodynamic Model:**

The power output and air consumption was measured at each cut-off ratio and compared to the air model's numerical results. The effect of cut-off ratio on output power and air consumption was demonstrated through the test results.

### **6.2 Findings**

A finding of the undertaken project was that an internal combustion engine can be successfully converted into a piston expander. The cut-off ratio was found to have a significant influence on the power output at lower cut-off ratios and less of an effect at higher cut-off ratios. This trend was expected from the developed thermodynamic model.

The thermodynamic model predicted the air consumption to vary linearly with cut-off ratio. This was validated by tests performed on the prototype engine. The thermodynamic model overpredicted the air consumption due to the assumption of instantaneous valve events.

It was found that the developed thermodynamic model accurately predicted the effect of cut-off ratio on power output and air consumption. The thermodynamic model over predicted the power output when compared to the test results. This was attributed to the mechanical losses in the system which the thermodynamic model neglects.

The main finding of the project is that the variable valve duration system allows the engine to vary the power output whilst still having the same operating speed. The valve duration can be varied to match the required flow rates and power requirements.

## 6.3 Recommendations for Future Work

The following section discusses recommendations for further development of the undertaken project. A section is dedicated to the design recommendations for a second iteration of the prototype engine. This is followed by a section which addresses the limitations with the test equipment and suggestions for future tests. The last section discusses the potential of testing the developed engine on a saturated steam supply.

### 6.3.1 Design Recommendations

A recommendation for future work on the developed engine is to rely less on press fittings and rather design fastened joints. The dowel pins on which the cam follower needle bearing ran, Figure 4.31 [2], were press fit into the rocker body. These press fits came loose during testing as the high shock experienced expanded the press fit hole. The dowel pin could be redesigned to have threads on either end and fastened to the rocker body using nuts.

Dowel pins were used for the belt rollers to run on. These were press fit into the roller holders and came loose during testing due to the vibration of the engine. These could be replaced with thread nut fastened pins.

The cam follower needle bearings experienced excessive forces when the engine speed exceeded the design speed. A way to reduce these forces is to design a system with larger cams which will have a lower pressure angle for the same rise angle of rotation,  $\beta$ .

A more in-depth analysis into flywheel design can be performed and a flywheel manufactured for specific operation requirements. This was out of the scope of the undertaken project which focussed on the development of a proof of concept engine to demonstrate the performance of the designed variable valve duration system.

### 6.3.2 Thermodynamic Model Recommendations

The accuracy of the thermodynamic model's prediction of power output could be increased through incorporating the mechanical losses and determining the power lost by driving the cam system.

### 6.3.3 Engine Testing Recommendations

The tests performed on the developed engine had certain limitations which could be improved in future testing. During start up, the engine would accelerate to speeds higher than the design speed. This resulted in excessive forces on the follower needle bearings which required replacing. The tests had a time limitation

due to the disk brake reaching high temperatures for longer runs. Both limitations mentioned above could be eliminated by testing the engine coupled to a direct current (DC) electric dynamometer.

A DC electric dynamometer is a DC motor connected to a load cell which measures the torque experienced during testing. The DC motor is supplied a current which starts the engine it is coupled to. The speed of the DC motor can be kept constant and the output torque of the engine measured by the load cell attached to the floating DC motor's casing (Grobbelaar, 2017). A shaft mounted encoder can be used to measure output shaft speed more accurately than the proximity sensor which only measures one count per revolution.

The accuracy of the piston expander tests could be improved by performing multiple runs at each cut-off ratio. This was a major limitation with the brake system used which eventually failed.

A consideration for future testing is to fit a pressure transducer and thermocouple at the top of the engine cylinder. This could be used to measure the pressure and temperature changes within the cylinder during the engine cycle.

The engine's actual P-V diagram can be measured and used to find the largest deviations from the thermodynamic model's P-V diagram. The thermocouple could be linked to a data logger to get instantaneous temperature readings.

The pressure transducer can be used to measure the pressure within the cylinder after exhaustion. If the pressure is significantly higher than atmospheric pressure, then a larger exhaust port would need to be machined into the cylinder.

The cylinder mounted thermocouple and pressure transducer could also be used to measure the conditions within the cylinder during steam admission through the inlet valve. These results could be compared to the inlet valve flow calculations.

#### **6.3.4 Engine Testing on Steam Recommendations**

The materials used for the steam chest and belt system were chosen for ease and speed of manufacturing. For future testing on steam it is recommended to manufacture the steam chest out of a material with a lower expansion coefficient than the current aluminium.

For testing on steam, the current lubrication used in the bottom end should be replaced with a steam oil or an oil which can withstand a certain water content. If steam leaks past the piston ring it could deposit water into the bottom end oil. This could reduce the lubrication effect of the oil and result in wear of the crankshaft bearings.

After successful testing of the expander on a steam supply, the design could be scaled up to the conversion of an automotive engine into a piston steam expander. This developed expander could be implemented in a direct steam small-scale CSP plant or potentially used in generating off-peak power from a small-scale solar thermal storage system.





## 7 References

- Anonymous, 2017. *Intake and Exhaust Valves and Mechanisms*. [Online]  
Available at: <http://what-when-how.com/automobile/intake-and-exhaust-valves-and-mechanisms-automobile/>  
[Accessed 21 July 2016].
- Bannister, P., 1998. The ANU Solar Thermal Steam Engine: Performance Analysis. *International Journal of Energy Research*, Volume 22, pp. 303-316.
- Bateman, W., 2011. *Velocity and Acceleration of a Piston*. [Online]  
Available at: <http://www.codecogs.com/library/physics/kinematics/velocity-and-acceleration-of-a-piston.php>  
[Accessed 12 February 2016].
- Bidini, G., Manuali, A. & Saetta, S., 1998. Reciprocating steam engine power plants fed by woodwaste. *International Journal of Energy Research*, Volume 22, pp. 237-248.
- Bouvier, J.-L. et al., 2016. Experimental study of an oil-free steam piston expander for micro-combined heat and power systems. *Applied Energy*, Volume 169, pp. 788-798.
- Budynas, R. G. & Nisbett, J. K., 2008. *Shigley's Mechanical Engineering Design*. 8th ed. New York: McGraw-Hill.
- Caprotti, A., 1925. *Valve gear for reversing steam engines*. Italy, Patent No. US1549712 A.
- Cengel, Y. A. & Boles, M. A., 2011. *Thermodynamics An engineering approach*. 7th ed. New York: McGraw-Hill.
- Elkon, D., 1987. *Engineering Guide to Spring Design*. Bristol: Barnes Group Inc.
- Ferguson, C. R. & Kirkpatrick, A. T., 2001. *Internal Combustion Engines*. 2nd ed. Colorado State University: John Wileys & Sons, Inc.
- Festo, 2009. *Festo MS6-SFE*, Esslingen: Festo.
- Giovannelli, A., 2015. State of the art on small-scale concentrated solar power plants. *Energy Procedia*, Volume 82, pp. 607-614.
- Grobbelaar, E., 2017. The Development of a Small Diesel Engine Test Bench Employing an Electric Dynamometer. *Stellenbosch University*.
- Heywood, J. B., 1988. *Internal combustion engine fundamentals*. Massachusetts: McGraw-Hill.
- Jennings, G., 1987. *Two-stroke tuner's handbook*. 1st ed. unknown: HP Trade.
- Kaneff, S., 1991. *The White Cliffs Project: Overview for the period 1979-89*, Sydney: Office of Energy.

- King, A. M., 2017. *British Caprotti Valve Gear*. [Online]  
Available at:  
<http://www.dukeofgloucester.co.uk/?section=locomotive&page=British+Caprotti+Valve+Gear>  
[Accessed 15 July 2016].
- Latz, G. et al., 2016. Performance analysis of a reciprocating piston expander and a plate type exhaust gas recirculation boiler in a water-based Rankine cycle for heat recovery from a heavy duty diesel engine. *MDPI*, Volume 9, pp. 495-513.
- Marks, J., 1854. *PISTON-VALVE AND STEAM-PASSAGE IN CYLINDRICAL STEAM-CHESTS*. United States of America, Patent No. US 10454 A.
- Oberg, E., Jones, F. D. & Horton, H. L., 1975. *Machinery's handbook*. New York: Industrial Press Inc.
- Osborne, R., 2010. *steam4me*. [Online]  
Available at: [http://msts.steam4me.net/tutorials/anim\\_walsch.html](http://msts.steam4me.net/tutorials/anim_walsch.html)  
[Accessed 21 July 2016].
- Rothbart, H. A., 2004. *Cam Design Handbook*. New Jersey: McGraw-Hill.
- SANS, 2012. *SANS 347:2012 Categorization and conformity assessment criteria for all pressure equipment*, Pretoria: SABS.
- SKF, 2015. *SKF Rod Seal*. [Online]  
Available at: [http://www.skf.com/binary/49-293967/Rod-seal-data-sheet-S19-F---11932\\_1-EN.pdf](http://www.skf.com/binary/49-293967/Rod-seal-data-sheet-S19-F---11932_1-EN.pdf)  
[Accessed 10 February 2017].
- SKF, n.d. *SKF Drawn cup needle bearings*. [Online]  
Available at: <http://www.skf.com/group/products/bearings-units-housings/roller-bearings/needle-roller-bearings/drawn-cup-needle-roller-bearings/drawn-cup-pt/index.html?designation=HK%200408>  
[Accessed 10 February 2017].
- Sprouse, C. & Depcik, C., 2013. Review of organic Rankine cycles for internal combustion engine exhaust waste heat recovery. *Applied Thermal Engineering*, pp. 711-722.
- Stratton, B. a., 95. *Operator/Owner Manual Model series 170400*, Milwaukee: Briggs and Stratton Corporation.
- Stumpf, P. J., 1922. *The Una-Flow Steam-Engine*. 2nd ed. Berlin: Forgotten Books.
- Tompkins, A., 2013. *The Uniflow Steam-engine*. 1st ed. Alcester: Read Books.

# Appendix A : Pressure Vessel Report

## A.1 Introduction

This report inspects the structural integrity of a cylinder head for an existing internal combustion engine as part of a master's thesis at the University of Stellenbosch. A finite element analysis (FEA) is performed on the designed component and the locations of maximum stress located.

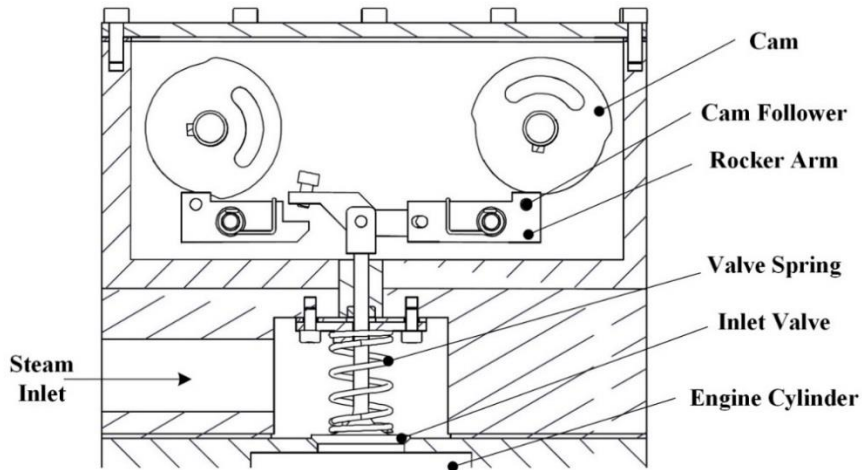
The engine cylinder head has an operating pressure of 10 MPa and volume of 0.157 litres. This falls under the sound engineering practice (SEP) category specified by the SANS 347. The existing internal combustion engine had an operating pressure of 2.2MPa and is omitted from any analysis as it was designed, manufactured and tested by Briggs and Stratton Corporation USA, model number 170400.

The FEA model (A-1) shows a maximum Von Mises stress of 11 MPa resulting in an operating safety factor of 25.45. The maximum deflection was found to be  $4.7 \times 10^3$  mm as seen in A-11. This is the worst-case scenario with the assumption of no load support by the Cam Housing. A safety release valve set to 12 bar is mounted to the cylinder head. Data sheets are included in Sections A.8 and A.9 for the gasket and seal used.

This document serves as proof of sound engineering practice used to design the air components. These parts do not classify as a pressure vessel according to *(Guidance Notes to the Pressure Equipment Regulations 17 July 2009 Department of Labour Occupation Health and Safety Act, Act 85 of 1993 Revision 1)* and thus a less detailed analysis is necessary.

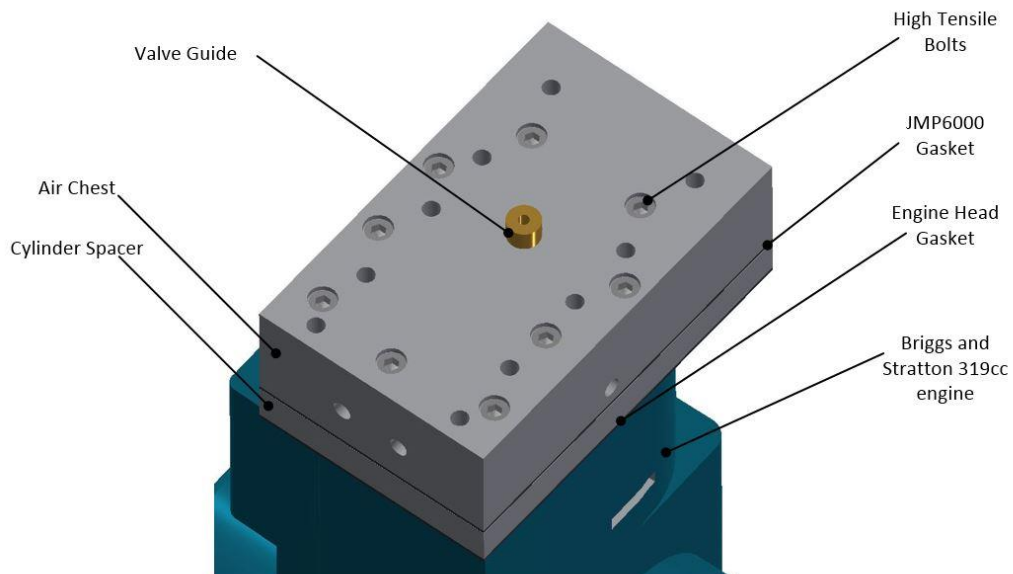
Regulation 2, point 3(d) of *(Guidance Notes to the Pressure Equipment Regulations 17 July 2009)* show that the designed inlet port does not classify as a pressure vessel. This point states that: **“pressure equipment comprising casings or machinery where the dimensioning, choice of material and manufacturing rules are based primarily on requirements for sufficient strength, rigidity and stability to meet the static and dynamic operational effects or other operational characteristics and for which pressure is not a significant design factor, and such pressure equipment may include - (i) engines, including turbines and internal combustion engines: (ii) reciprocating steam engines, gas turbines, steam turbines, turbo-generators, compressor engines, pumps and actuating devices;”** (SANS, 2012).

The uniflow engine will operate by admitting air into the engine cylinder via a poppet valve (A-1) which in turn will drive the piston down. The expanded air is then exhausted through an exhaust port at the bottom of the piston stroke. The component to be analysed is the valve port where air will collect before being admitted into the cylinder.



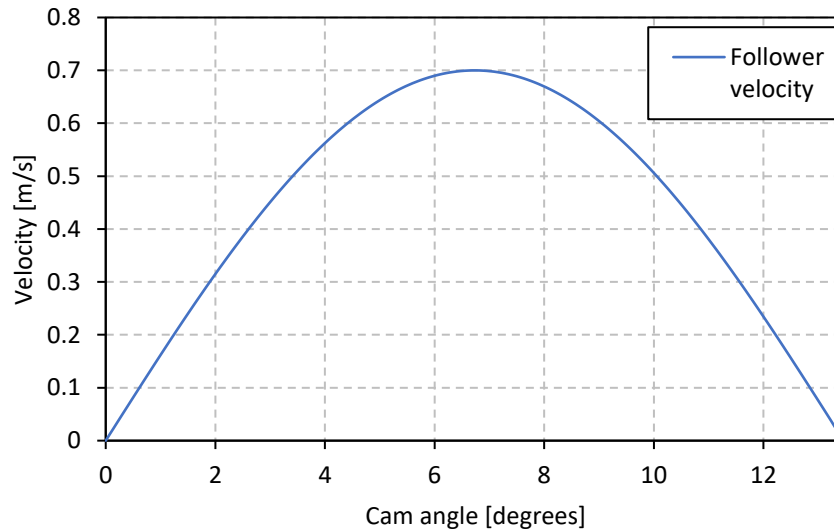
**A-1: Inlet port cross section**

The port section is created by the cylinder spacer and air chest which are torqued down onto the engine via 9 high tensile bolts. A 1.5 mm thick JMP6000 fibre gasket is sandwiched between the two components which has a maximum allowable pressure of 120 bar (Section A.9). The engine's original metal head gasket is used between the cylinder spacer and cylinder head (A-2).



**A-2: Cylinder head assembly**

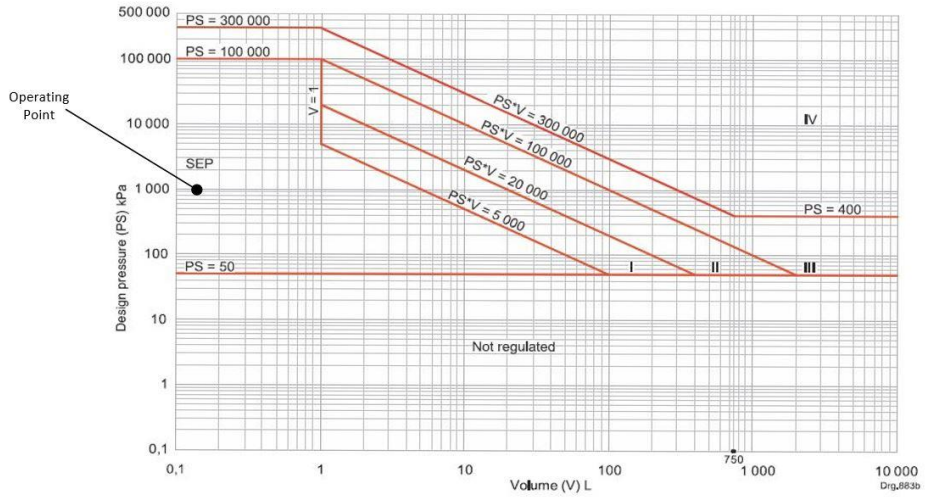
A SKF S19-F rod seal is seated in a machine brass valve guide. The seat was designed according to the SKF design recommendations (Section A.8) for a 5 mm diameter shaft. At the operating speed of 500 rpm, the maximum valve velocity is  $0.7\text{m}\cdot\text{s}^{-1}$  (A-3) which falls under the  $15\text{m}\cdot\text{s}^{-1}$  limit of the rod seal (Section A.8).



**A-3: Valve lift velocity profile at 500rpm**

## A.2 SANS 347 Conformity

The prototype engine will be tested with a 10 bar air supply. The inlet port has a total volume of 0.157 litres obtained from Autodesk Inventor 2016. A-4 below shows the various categories for pressure vessels holding non dangerous gases. The operating point of the inlet port is shown to be in the lower bounds of the SEP category. As stated in the SANS 347, "The equipment shall have instructions for use and shall bear the identification of the manufacturer. SEP equipment is not required to meet any other of the essential statutory requirements listed in the relevant national legislation." (SANS 347:2012).



**A-4: Graph for vessels – non dangerous gas (adapted from SANS 347:2012)**

## A.3 FEM Analysis

A Fem Analysis was performed on the air chest and cylinder spacer separately. No analyses were necessary for the threads as these are part of the existing engine which operated at 22 bar. Both components are manufactured from Aluminium 6082 which have properties shown in A-5.

The screenshot shows the 'Input Options' dialog box with the 'Constitutive Model' set to 'Linear Elastic'. The following table lists the material properties and their values:

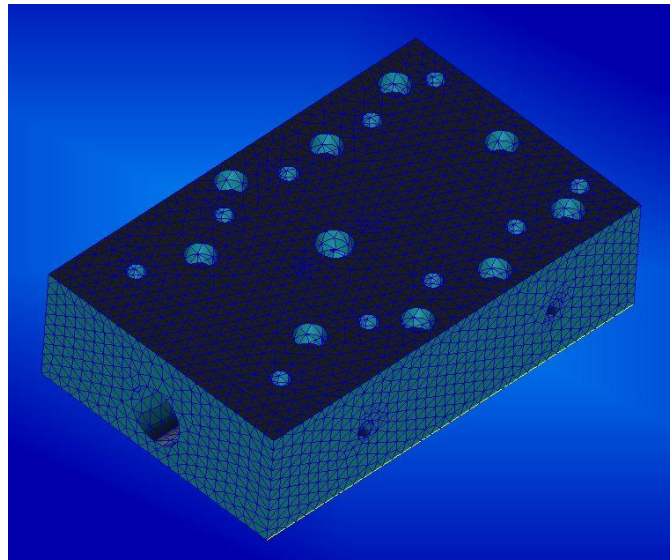
Property Name	Value
Elastic Modulus =	72000.
Poisson Ratio =	0.33000001
Shear Modulus =	
Density =	2.71E-009
Thermal Expan. Coeff =	2.3099999E-005
Structural Damping Coeff =	
Reference Temperature =	293.

**A-5: Aluminium 6082 properties**

A tetrahedral 10 mesh with 5 mm resolution was made on the air chest shown in A-6.

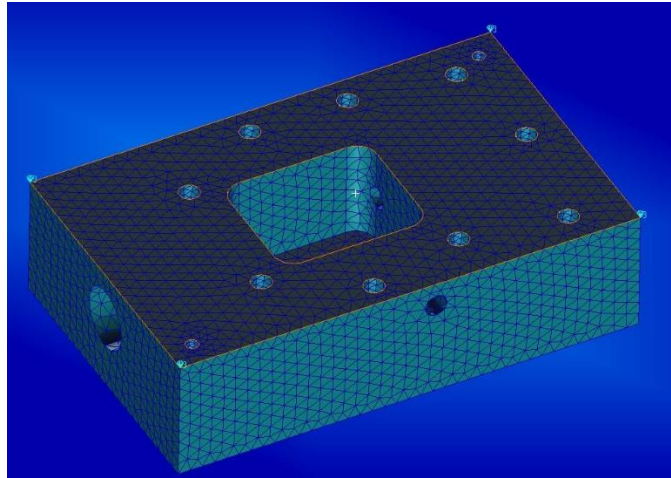
The screenshot shows the 'Finite Elements' dialog box with the following settings:

- Action: Create
- Object: Mesh
- Type: Solid
- Output ID List:
  - Node: 130018
  - Element: 89059
- Elem Shape: Tet
- Mesher: TetMesh
- Topology: Tet10
- Buttons: TetMesh Parameters..., Node Coordinate Frames...
- Input List: Solid 1
- Global Edge Length:
  - Automatic Calculation
  - Value: 5.0



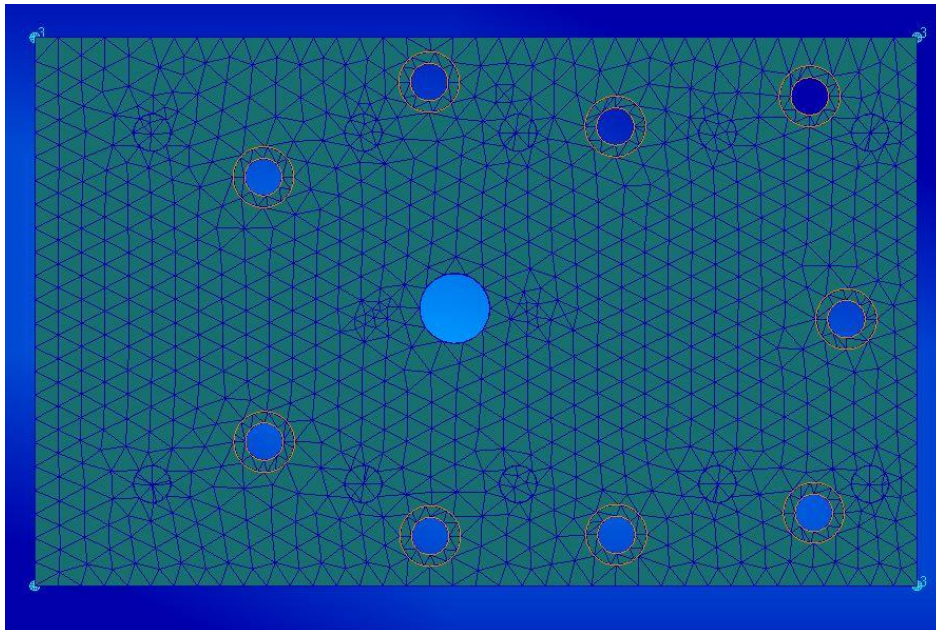
**A-6: Mesh settings (left), Steam chest mesh (right)**

The base of the steam chest was constrained in the z axis and free to expand in the x and y. All rotations of the base were fixed.



**A-7: Base surface constraint**

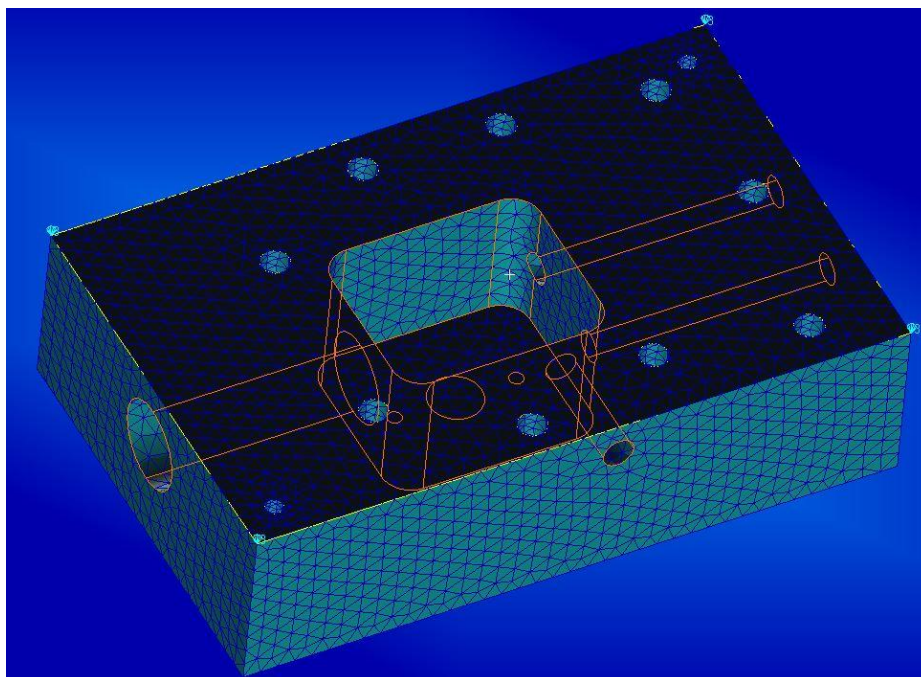
The surfaces where the bolts are torqued down onto the part were constrained in all degrees of freedom as a worst-case scenario. A-8 below shows the surfaces constrained.



**A-8: Bolt surface constraints**

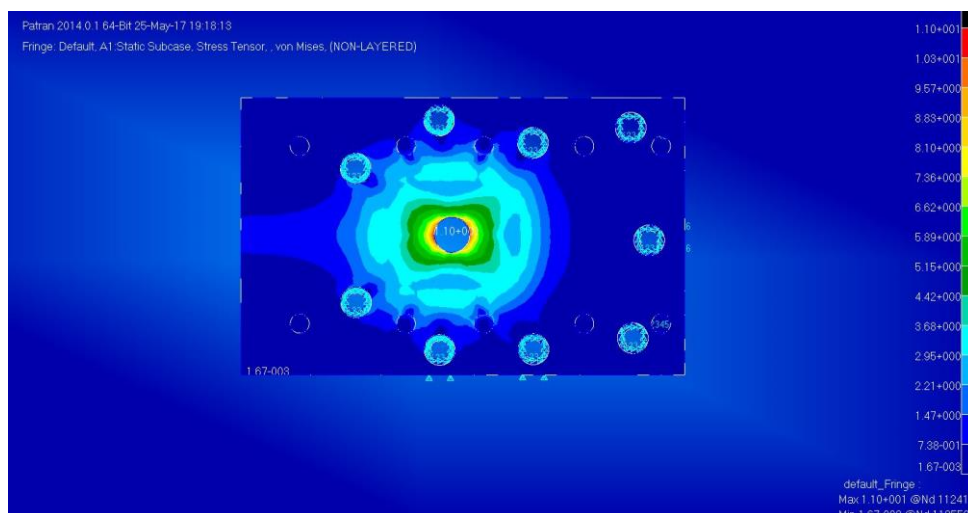
An operating pressure of 10 bar was applied to the inner surfaces of the steam chest and ports. This can be seen in A-9 below.





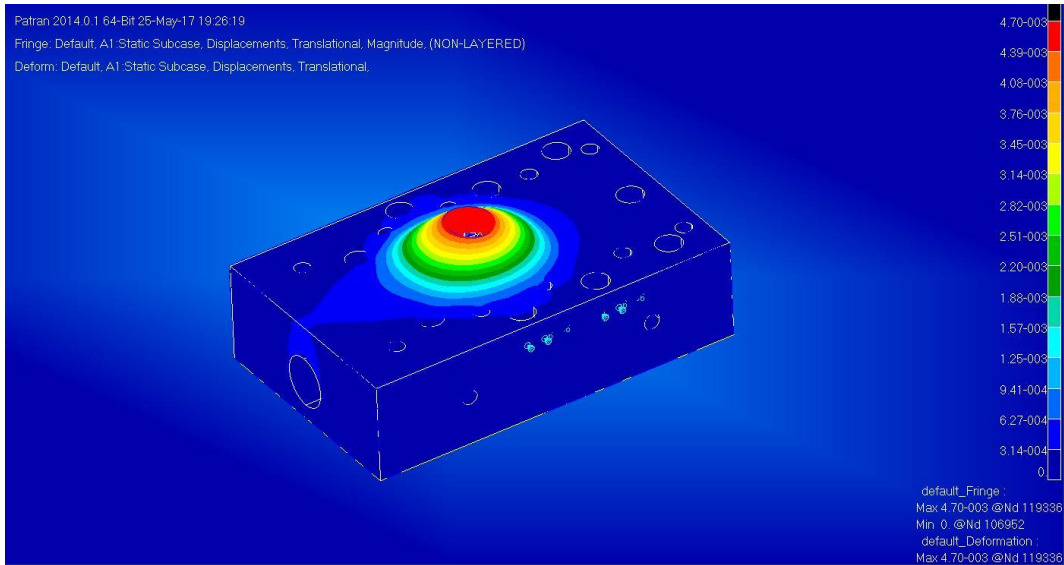
**A-9: Applied surface pressure**

The maximum Von Mises stress was found to be 11 MPa and occurs at the top of the block where the valve bushing is press fit in with hydraulic sealant. This was a 10 micron interference fit performed at The Mechanical Engineering workshop. This maximum stress is shown in A-10. The yield stress of Aluminium 6082 is 280MPa which results in a safety factor of 25.45.



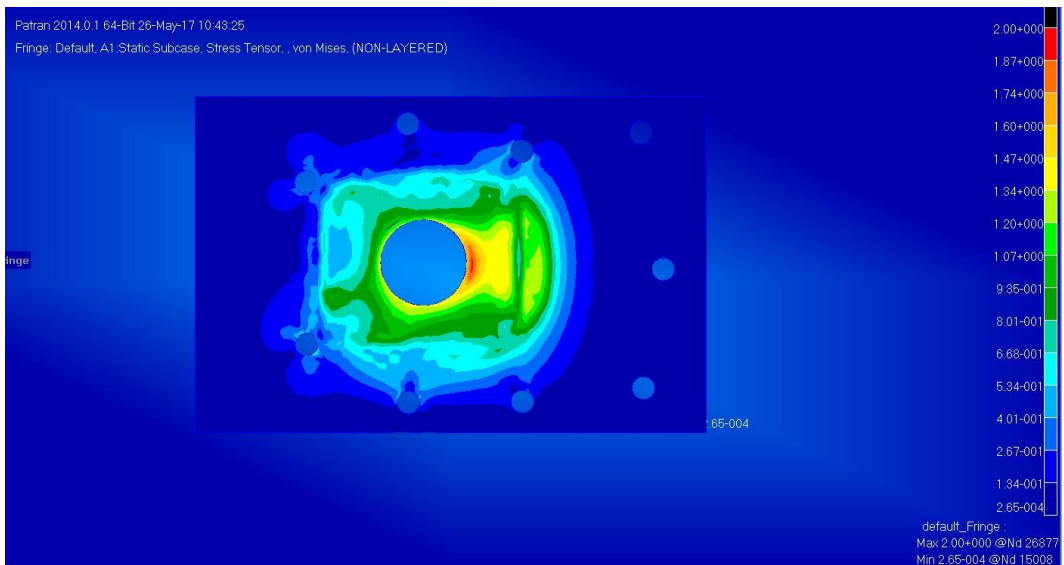
**A-10: Steam chest Von Mises stress distribution**

The maximum deflection was found to occur in the same location as the maximum Von Mises stress and had a value of  $4.7 \times 10^{-3}$  mm. This is seen in A-11 below.



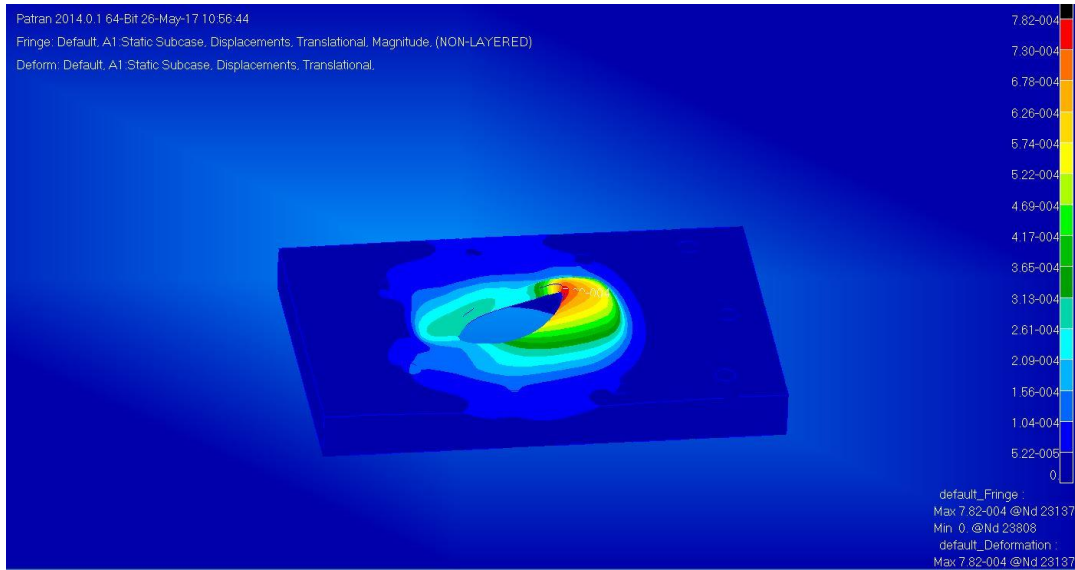
**A-11: Steam chest deformation**

The same FEM analysis procedure was performed on the cylinder spacer and found to have a maximum Von Mises stress of 2 MPa at the location seen in A-12.



**A-12: Cylinder spacer Von Mises stress distribution**

The maximum deflection was found to be  $7.3 \times 10^{-4}$  mm at the location seen in A-13.



**A-13: Cylinder spacer deformation**

## A.4 Bolt Analysis

The inlet port and cylinder spacer are fastened to the engine head with 9 M8 x 100mm high tensile cap screws. These are made of 12.9 grade heat treated high tensile alloy steel with a maximum tensile strength of 1200 MPa (Section A.10).

The forces experienced by the 9 bolts are determined below for an operating pressure of 10 bar. The inlet port will experience a vertical force due to the pressure on the top part of the cavity. The area of this surface is calculated to be  $50\text{mm} \times 60\text{mm} = 3000\text{mm}^2$ . The vertical force on the inlet port is then determined as seen below where  $F$  is the vertical force,  $P$  is the operating pressure and  $A$  is the cavities top surface area.

$$F = P \times A$$

This results in a total force of 3000 N which the 9 bolts must support. Each bolt in turn will experience 333.3 N. The cross sectional areas of the bolts are determined using the thread minor diameter of 7.188 mm. The resulting stress is determined in the equation below.

$$\sigma = \frac{F_{bolt}}{A_{bolt}}$$

The stress in each bolt is determined to be 8.2143 MPa which results in a safety factor of 146. This assumes the total force of 3000 N is evenly distributed to the 9 bolts. If it assumed that the entire load is carried by a single bolt the stress within the bolt is 73.93 MPa, still far below the 1200 MPa maximum tensile strength.

## A.5 Assembly Instructions

The assembly of the engine air chest is performed in the following manner:

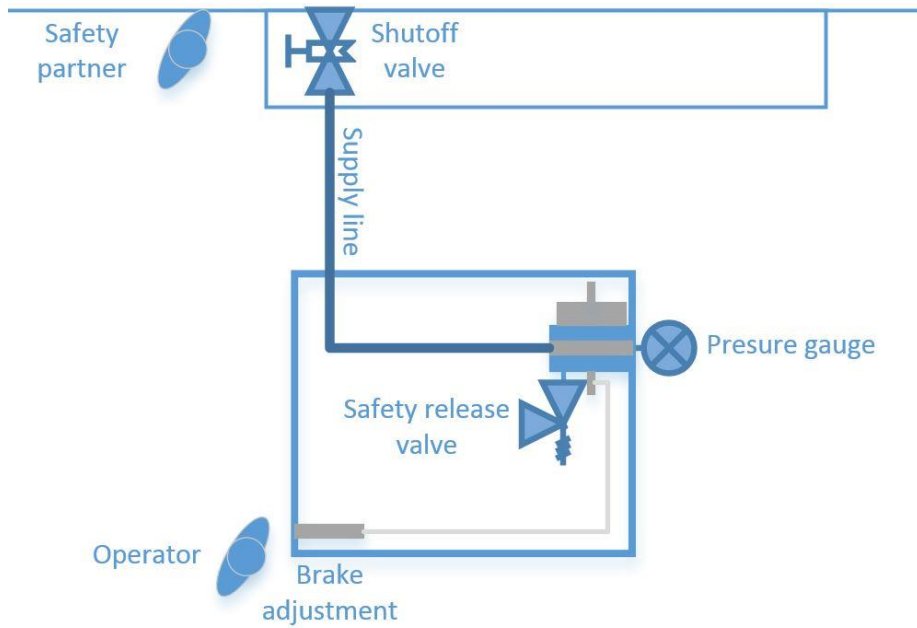
- The engine head surface is first cleaned to ensure proper sealing of the head gasket.
- The metal head gasket is placed on top of the cylinder head in the correct orientation
- The cylinder spacer is cleaned and placed on top of the head gasket.
- The valve seal is seated into its machined seat within the valve guide seen in Figure 2.
- The valve is inserted into its guide and the air chest is placed on top of the cylinder spacer.
- Correct alignment between the cylinder spacer and air chest is aided by two dowel pins on outer corners of the air chest. Location of these dowel pin holes can be seen in Figure 9.
- 9 new M8 x 100mm bolts are placed into the aligned holes of the cylinder spacer and air chest. The bolts are threaded into the existing threads in the engine cylinder head. These are incrementally tightened down in an altering manner to ensure even compression of the gaskets. Loctite was used to ensure the bolts do not come loose during operation.
- The cam housing is then bolted on top of the air chest following the same procedure of using Loctite and tightening in a criss-cross pattern.
- The safety release valve and pressure gauge are threaded onto the air chest via a ½ inch threads. Tapered threads and thread tape ensures a proper sealing.

## A.6 Engine Operation

The engine will be tested on the 10 bar air supply line in the Heat Transfer lab. A pressure regulator at the wall will be used to ensure a constant pressure supply. A shutoff valve before the regulator will be used to cut the air supply to the engine in the case of an emergency. A-14 shows the floor plan of the engine tests.

The following procedure will be followed for each test run:

- Ensure engine is securely fastened to test bench
- Ensure Hose clamps are securely fastened to the barbed fittings
- Put castor wheel brakes on to prevent test bench moving
- Turn engine over to just before TDC position such that the inlet valve is still closed
- Set cut-off ratio to desired value
- Turn on data logger for load cell
- Turn on Thermocouple reader and tachometer
- Set pressure regulator to 10 bar and open the shutoff valve. Always have a colleague manning the shutoff valve for precaution.
- Pull start the motor and adjust braking system until a constant speed of 500 rpm is read on the tachometer
- Record load cell reading
- Record inlet port pressure and temperature reading
- Close shutoff valve and wait for engine to come to a complete standstill.
- Ensure pressure within the inlet port has dropped to atmospheric before proceeding.
- Ensure engine has come to a complete standstill before approaching
- Repeat the entire procedure for various cut-off ratios and record the data



**A-14: Engine test floor plan**






## A.7 Possible Failure Modes





Given the information above, it is assumed that the first components to fail would be the rod seal on the valve stem. This seal has a maximum operating pressure of 20 bar shown in Appendix A.8. The next possible failure is the JMP6000 gasket with a maximum operating pressure of 120 bar.

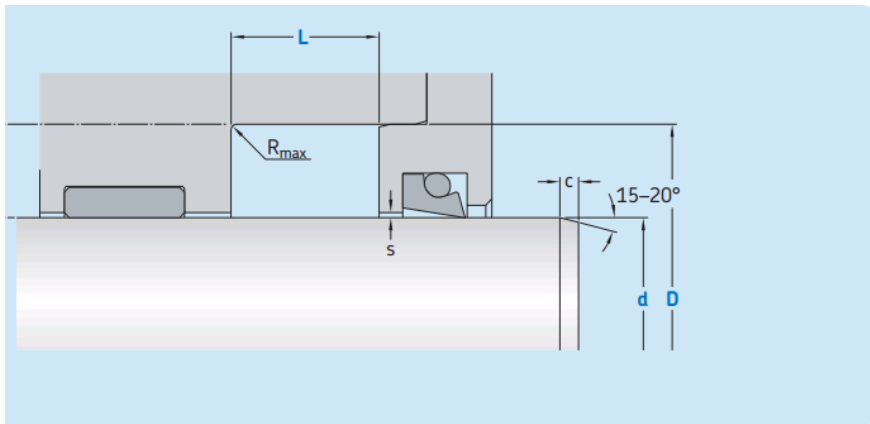
In the unlikely event that one of the high tensile bolts fails, the air will escape through the JMP6000 gasket of head gasket. The user will notice a sudden pressure drop and immediately shut off the air supply.

## A.8 SKF S19-F rod seal

Rod seals

 Linear moving 
  Rotating 
  Oscillating 
  Spiral moving 
  Static  
 Grey symbols: contact SKF for application limitations

Appli- Profile cation	Description	Temperature		Speed max. m/s	Pressure max. bar (psi)	Material	
		min. °C	max.			Seal	Spring
 S19-F   	<b>PTFE rod seal, single-acting</b> Finger spring activated, asymmetrical PTFE rod seal, low friction and good dry running properties, excellent chemical and thermal resistance, mainly used in chemical, pharma and food industry.	-200	+260	15	200 (2 900)	SKF Ecoflon 1	1.4310 <sup>3</sup>
		-200	+260	15	400 (5 800)	SKF Ecoflon 2	1.4310 <sup>3</sup>
		-200	+260	15	400 (5 800)	SKF Ecoflon 3	1.4310 <sup>3</sup>
		-200	+260	15	400 (5 800)	SKF Ecoflon 4	1.4310 <sup>3</sup>
		-200	+90	15	200 (2 900)	SKF ECOWAER 1000	1.4310 <sup>3</sup>



Standard dimensions					Maximal radial extrusion gap					
d	D	L	R <sub>max</sub>	c	s*					
f8	H10	+ 0,2			20 bar	100 bar	200 bar	300 bar	400 bar	
over	incl.				mm					
5	18	d + 4,5	3,6	0,4	2,0	0,25	0,12	0,10	0,08	0,07
18	50	d + 6,2	4,8	0,4	3,0	0,35	0,17	0,12	0,10	0,08
50	120	d + 9,4	7,1	0,4	4,0	0,45	0,22	0,17	0,12	0,10
120	630	d + 12,2	9,5	0,4	5,0	0,60	0,31	0,25	0,15	0,12
630	1 600	d + 19,0	15,0	0,4	6,0	0,87	0,48	0,38	0,28	0,20

\* Extrusion gap values shown above are valid for a temperature of 80 °C, higher temperatures require lower values.

A-15: SKF S19-F rod seal datasheet (SKF, 2015)

## A.9 JMP 6000 gasket

### Technical Data Sheet

### JMP 6000

**Basis** Mineral wool fibres, NBR

**General Properties and Applications:**

Due to its superior resistance to steam and long-term steam sealability JMP 6000 is particularly recommended for all applications where thermal cycling, saturated or overheated steam are applied, e.g. heat exchangers, boilers, radiators, steam supply, power generation, etc.

**Dimensions of standard sheets:**

Sheet size: 1500 x 1500mm, 1500 x 2000mm, 1500 x 4500mm

Thickness: 1.5 and 3.0mm (other thicknesses available on request)

Tolerances: Thickness: <1 mm = ± 0.1mm, 1mm = ± 10 %, Length: ±50mm, Width: ± 50mm

**Surface treatment:** Treatment with anti-stick coating is standard.

Typical values (thickness 2.0mm)

Density	DIN 28090-2	1.7 - 1.9 g/cm <sup>3</sup>	
Compressibility	ASTM F36/J	5 - 9%	
Recovery	ASTM F36/J	> 55%	
Tensile Strength	DIN 52910	≈ 9 Mpa	
Specific Leak rate	DIN 3535/6	≈ 0.05 mg/(s.m)	
Stress resistance	DIN 52913	16h, 300° C, 50 MPa	16h, 175° C, 50 MPa
		≈ 30 MPa	≈ 35 MPa
Thickness increase	ASTM F146	Oil IRM 903, 5h, 150°C	ASTM Fuel B, 5h, 20°C
		≤ 5%	≤ 5%
Maximum operating conditions	Peak temperature	440°C / 824°F	
	Continuous temperature	350°C / 662°F	
	Temperature with steam	300°C / 482°F	
	Pressure	120 bar / 1740 psi	

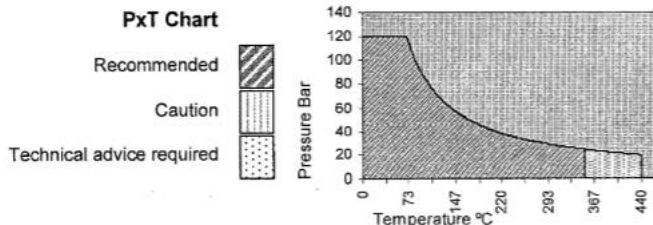
Considerations for gasket material selection.

<b>S</b> ize	Thickness, thinner gaskets are recommended. Gaskets larger than sheets must be dovetailed.
<b>T</b> emperature	Peak and continuous. Refer to the PxT chart for recommended, caution and technical advice values.
<b>A</b> pplication	Factors such as safety, accessibility of joint and installation procedures affect gasket selection.
<b>M</b> edium	Refer to the chemical reference chart paying particular attention to steam, oxidizing agents and purging medium.
<b>P</b> ressure	Operation design and spikes. JMP offers technical assistance on non standard flange bolting and surface finish.

Maximum P x T value

8,400 (Bar x °C)  
240,000 (psi x °F)

At the limits of pressure and temperature refer to JMP for technical advice.



A-16: JMP 6000 head gasket datasheet



## A.10 Cylinder head bolts



Professionally approved products.

EN

### Datasheet

#### High Tensile Steel Black Self-Colour Hexagon Socket Cap Head Screws: Metric Thread

**RS Product No: 281647**



Socket caps have a small cylindrical head with tall vertical sides giving them space saving advantages as well as greater tensile strength and they require less side room for wrenches.

- 12.9 grade heat treated high tensile alloy steel
- Threaded in accordance with Din 912 standard
- 1200 MPa maximum tensile strength\* compared to just 800 MPa for structural grade 8.8 so can be used in high tensile applications
- 1100 yield strength\*\* compared to 640-660 MPa depending on the size of the screw for structural grade 8.8
- 970 MPa proof load\*\*\* compared to just 580-600 depending on the size of the screw for structural grade 8.8
- Used for applications with limited space in high tensile applications
- Suitable for use in many industrial applications and similarly medical, construction, electronic & domestic applications
- Requires a Hex key / Allen key

### A-17: Cylinder head bolts datasheet

# Appendix B : Inlet Valve Matlab code

## B.1 ODE45 script

```

%%%%%%%%% set initial conditions and perform ODE45
%%%%%%%%%%%%%%%%%%%%%%%%%%%%%%%%%%%%%%%%%
close all

rpm = 500;
CR = 15;      % cutoff ratio [%]

V_o =0.0000638;      %TDC cylinder volume [m^3]
m_o =0.000239;      % initial mass in cylinder [kg]
T_o = 165.01+273.15;      % intial cylinder temperature [K]
R=0.4615;
w = rpm*2*pi/60; % angular velocity [rad/s]
L_stroke = 0.06985; %stroke length [m]
L_cutoff = L_stroke*(CR/100) % piston position at valve cutoff
r=0.032; % crank arm radius [m]
l=0.1045; % conrod length [m]

syms t_cr
eqn = L_cutoff == (l+r)-(r*cos(w*t_cr)+sqrt(l^2-
r^2*sin(w*t_cr)^2)); % equation for piston displacement [m]
s = vpasolve(eqn,t_cr,[0 30/rpm]); % calculating time valve is
open [s] 30/rpm = 0.5*60s/rpm
t_f = double(s);
t = linspace(0,t_f,1000);

y_o = [V_o,m_o,T_o];      % setting initial condition vector

[T,y] = ode45(@flowVariables,t,y_o, odeset('Maxstep',t_f/1000)) %
ODE45 calling flowVariables function for t =0 to t = t_f
P = (y(:,2).*R.*y(:,3))./y(:,1)
plot(T,y(:,1))
hold on
title('Piston Volume VS time')
xlabel('Time [s]')
ylabel('Volume [m^3]')
hold off
figure
plot(T,y(:,2))
hold on
title('Steam mass in cylinder VS time')
xlabel('Time [s]')
ylabel('Mass [kg]')
hold off
figure
plot(T,y(:,3)-273.15)
hold on
title('Temperature in cylinder VS time')

```

```

xlabel('Time [s]')
ylabel('Steam temperature [deg C]')
hold off

```

```

figure
plot(T,P)
hold on
title('Steam Pressure VS time')
xlabel('Time [s]')
ylabel('Pressure [kPa]')
hold off

```

```

figure
plot(y(:,1),P)
hold on
title('volume vs pressure')
xlabel('Time [s]')
ylabel('Pressure [kPa]')
hold off

```

## B.2 Flow Variables function

```

function [dy_dt] = flowVariables(t,y)
rpm=500;
r=0.032; % crank arm radius [m]
l=0.1045; % conrod length [m]
A=pi*(0.0381)^2; % piston area [m^2]
R=0.4615; % specific gas constant of steam [KJ/kgK]

P_up = 1000; % supply pressure [KPa]
T_in = 453.15; % supply temperature [K]
gamma = 1.327; % specific heat ratio of steam
p_o = 5.14355; % density of steam at 1000KPa, 180 degrees [kg/m^3]
C_d = 0.7; % discharge coefficient
l_v = 2e-3; % valve lift [m]
A_v = pi*(34e-3)*(l_v); % valve flow area [m^2]
c_o = 1036.61; % stagnation speed of sound [m/s]
cp = 1.8723; % constant pressure specific heat [KJ/kgK]
cv = 1.4108; % constant pressure specific heat [KJ/kgK]

w = rpm*2*pi/60; % speed [rad/s]

V = y(1); % cylinder volume
m = y(2); % mass in cylinder
T = y(3); % temperature in cylinder
P_down = (m*R*T)/V; % cylinder pressure [KPa]
v_dot = (r*sin(w*t)+(r^2*(sin(2*w*t))/(2*l)))*w; % piston velocity
equation [m/s]

```

```
m_dot = p_o*C_d*A_v*c_o*real(sqrt((2/(gamma-1)) * ((P_down/P_up)^(2/gamma) - (P_down/P_up)^((gamma+1)/gamma)))); %  
mass flow into cylinder [m/s]  
dV_dt = v_dot*A; % Volume derivative  
dm_dt = m_dot; % mass derivative  
dT_dt = (1/(m*cv)) * (m_dot*(cp*T_in-cv*T) - (P_down*v_dot*A)); %  
temperature derivative  
  
dy_dt = [dV_dt;dm_dt;dT_dt]; % output vector  
  
end
```

# Appendix C : Calculations

## C.1 Valve Spring Calculations

### Valve spring calculations

$$l_f := 35 \text{ mm}$$

$$d := 2 \text{ mm} \quad (\text{wire diameter})$$

$$N_a := 4.5$$

$$D_i := 19 \text{ mm}$$

$$D := D_i + d$$

$$k := \frac{G \cdot d^4}{8 \cdot D^3 \cdot N_a} \quad k = 3311.3775 \frac{N}{m}$$

$$F := k \cdot l_f$$

$$F = 16.5569 \text{ N} \quad (\text{Valve sealing force})$$

$$P_{\text{diff}} := \left( \frac{F}{A_{\text{valve}}} \right)$$

$$P_{\text{diff}} = 0.1824 \text{ bar}$$

$$C := \frac{D}{d}$$

$$K_w := \frac{4 \cdot C - 1}{4 \cdot C - 4} + \frac{0.615}{C}$$

$$S := \frac{8 \cdot F \cdot D}{\pi \cdot d^3} \cdot K_w$$

$$S = 125.8945 \text{ MPa} \quad (\text{yield strength 302} = 240 \text{ MPa})$$

$$W = 0.01 \cdot 9.81 \text{ N}$$

$$g = 9.81 \frac{m}{s^2}$$

$$\rho = 8 \frac{\text{gram}}{\text{cm}^3}$$

$$n_2 = 0.5 \cdot \sqrt{\frac{k \cdot g}{W}}$$

$$n_2 = 287.7228 \text{ Hz}$$

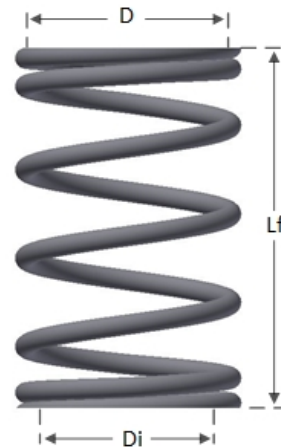
$$n_{\text{operate}} := \frac{500 \text{ rpm}}{60}$$

$$n_{\text{operate}} = 0.8727 \text{ Hz}$$

$$G := 69 \text{ GPa} \quad (\text{stainless steel 302})$$

$$d_{\text{valve}} := 34 \text{ mm}$$

$$A_{\text{valve}} := \pi \cdot \frac{d_{\text{valve}}^2}{4}$$



## C.2 Cam Follower Calculations

### Cam follower calculations

#### Spring Stiffness required

$$J_1 = 11.014 \text{ kg mm}^2 \quad (\text{rocker moment of inertia})$$

$$a_{\max} = 489.94 \frac{\text{m}}{\text{s}^2} \quad (\text{maximum negative acceleration along cam curve})$$

$$r = 11 \text{ mm} \quad (\text{distance from roller to rocker pivot point})$$

$$\alpha = \frac{a_{\max}}{r} \quad \alpha = 44540 \cdot \frac{1}{\text{s}^2}$$

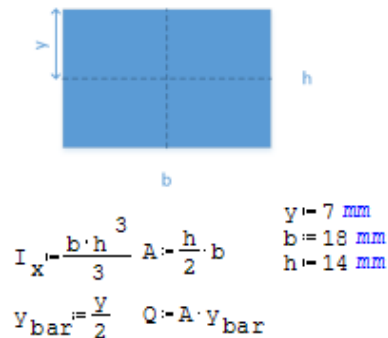
$$T = J_1 \cdot \alpha$$

$$T = 0.4906 \text{ N m} \quad (\text{Torque to keep follower in contact with cam surface})$$

#### Rocker Strength

$$F_{\text{lift}} = (211.28 + 16.55) \text{ N} \quad (\text{Steam pressure force plus valve spring force})$$

$$F_1 = 0.5 \cdot F_{\text{lift}} \quad (\text{valve rocker leverage})$$



$$F_{\text{cam}} = 2 \cdot F_1 + \frac{T}{0.011 \text{ m}} + \frac{0.5 \text{ N m}}{0.011 \text{ m}} \quad F_{\text{cam}} = 317.8812 \text{ N}$$

(lifting force + spring preload + dynamic force)

$$F_2 = F_1 + F_{\text{cam}} \quad +$$

$$M_{\max} = F_{\text{cam}} \cdot 0.011 \text{ m}$$

$$V = F_2 - F_{\text{cam}}$$

$$\sigma_{\max} = \frac{M_{\max} \cdot y}{I_x} \quad \sigma_{\max} = 1.4867 \text{ MPa}$$

$$\tau_{\max} = V \cdot \frac{Q}{I_x \cdot b} \quad \tau_{\max} = 0.1695 \text{ MPa} \quad (\text{Aluminium 7075: 500 MPa yield})$$

**Rocker Rod Strength**

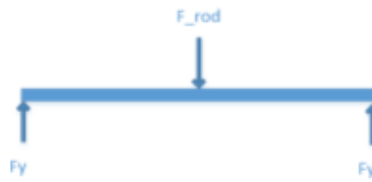
$$F_{rod} = F_2$$

$$F_Y = \frac{F_{rod}}{2}$$

$$l_{rod} = 40 \text{ mm}$$

$$M_{rod} = F_Y \cdot \frac{l_{rod}}{2}$$

$$\sigma_{rod} = \frac{M_{rod} \cdot r_{rod}}{I_{rod}}$$



$$r_{rod} = 3 \text{ mm}$$

$$I_{rod} = \frac{\pi \cdot r_{rod}^4}{4}$$

$$A_{rod} = \frac{\pi \cdot r_{rod}^2}{2}$$

$$V_{rod} = \frac{4 \cdot r_{rod}}{3 \cdot \pi}$$

$$V_{rod} = F_{rod} \cdot F_Y$$

$$\tau_{rod} = \frac{V_{rod} \cdot A_{rod} \cdot V_{rod}}{I_{rod} \cdot 2 \cdot r_{rod}}$$

$$\sigma_{rod} = 203.6222 \text{ MPa} \quad (\text{silver steel: } 750 \text{ MPa yield}) \quad \tau_{rod} = 10.1811 \text{ MPa}$$

**Spring Design Calculations**

$$D_i = 6.3 \text{ mm} \quad d = 1.2 \text{ mm} \quad \theta = \frac{45}{360}$$

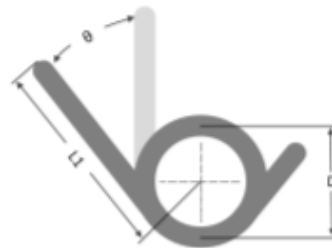
$$L_1 = 15 \text{ mm}$$

$$N_b = 2.5$$

$$D = D_i + d N_e = \frac{L_1}{3 \cdot \pi \cdot D} \quad N_a = (N_b + N_e)$$

$$D = 7.5 \text{ mm}$$

$$N_a = 2.7122$$



$$D_{reduced} = \frac{D \cdot N_b}{N_b + \theta}$$

$$D_{reduced} = 7.1429 \text{ mm}$$

$$L_i = d \cdot (N_b + 1) \quad L_i = 4.2 \text{ mm} \quad (\text{initial body length})$$

$$L_f = d \cdot (N_b + 1 + \theta) \quad L_f = 4.35 \text{ mm} \quad (\text{deflected body length})$$

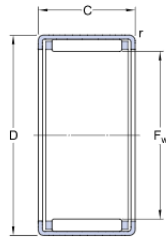
$$E_{302} = 200 \text{ GPa}$$

$$k = \frac{E_{302} \cdot d^4}{10.8 \cdot D \cdot N_a}$$

$$k = 1.8878 \text{ N m} \quad (\text{per revolution})$$

## HK 0408

### Dimensions



$F_w$	4	mm
D	8	mm
C	8	mm
r	min. 0.3	mm

### Calculation data

Basic dynamic load rating	C	1.76	kN
Basic static load rating	$C_0$	1.37	kN
Fatigue load limit	$P_u$	0.14	kN
Reference speed		22000	r/min
Limiting speed		26000	r/min

### Mass

Mass bearing		0.002	kg
Designation		HK 0408	

## C-1: SKF HK0408 drawn cup needle bearing datasheet (SKF, n.d.)



### C.3 Timing Belt Calculations

#### Timing belt calculations

assume worst case scenario,

take cam lifting force as acting tangential to cam surface

$$T_{\text{cam}} = F_{\text{cam}} \cdot 22.5 \text{ mm}$$

torque on the cam is equal to the torque on the camshaft pulley

$$r_{\text{pulley}} = 24 \text{ mm}$$

$$F_{\text{belt}} = \frac{T_{\text{cam}}}{r_{\text{pulley}}}$$

$$F_{\text{belt}} = 298.0137 \text{ N}$$

## Appendix D : Operating Manuals

### D.1 Briggs and Stratton 8HP Engine Manual

# Before Starting

READ THE OPERATING INSTRUCTIONS OF THE EQUIPMENT THIS ENGINE POWERS.

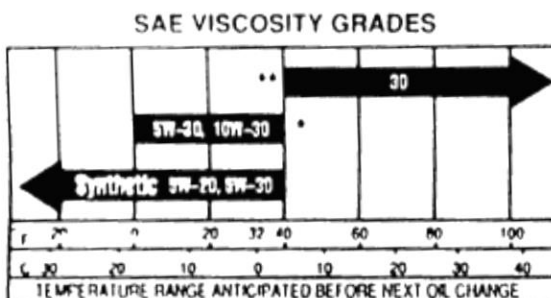
 NOTE: Engine is shipped WITHOUT oil.

#### 4-CYCLE OIL RECOMMENDATIONS

Change and Add Oil According to Chart below.

We recommend the use of a high quality detergent oil classified "For Service SE, SF, SG," such as Briggs & Stratton 30 weight oil, part no. 100005. Detergent oils keep the engine cleaner and retard the formation of gum and varnish deposits. No special additives should be used with recommended oils.

NOTE: DO NOT MIX OIL WITH GASOLINE.



- \* Air cooled engines run hotter than automotive engines. Use of multi-viscosity oils (10W-30, etc.) above 40° F (4° C) will result in high oil consumption and possible engine damage. Check oil level more frequently if using these types of oils.
- \*\* SAE 30 oil, if used below 40° F (4° C), will result in hard starting and possible engine bore damage due to inadequate lubrication.

#### TO FILL CRANKCASE WITH OIL:

Capacity is approximately 1-3/8 quarts (44 ounces or 1.3 liters). Place engine level. Clean area around oil fill. Remove oil fill plug or dipstick. **POUR OIL SLOWLY**. Fill to overflowing for oil fill plug. Fill to **FULL** mark on dipstick. **DO NOT OVER-FILL**. Replace oil fill plug or dipstick.

D-1: Briggs and 170400 engine manual (Stratton, 95)

## D.2 Festo MS6-SFE Hot-wire Flow Meter

MS6-SFE-...

### 6 Operation



#### Warning

Excessive internal heat will damage the MS6-SFE-... .

- Avoid high cycle frequencies with large pressure amplitudes. Otherwise the permitted maximum temperatures of the materials used will be exceeded.

The air mass flow measured and output by the MS6-SFE-... refers to the following standard conditions:

- Temperature: 0 °C
- Pressure: 1013 mbar
- Atmospheric density: 1.294 kg/m<sup>3</sup>

When comparing volume flows:

- Make sure that the volume flows to be compared (e.g. operating volume flow, amount supplied by a compressor, measured values of a flow sensor from another manufacturer) refer to the same basic conditions.

#### Reset the MS6-SFE-... to the factory setting

(also if the security code cannot be found)



#### Please note

All current settings will be lost after a reset to the factory setting. If necessary, make a note of these settings before a reset.

In order to reset the MS6-SFE-... to the factory setting:

1. Switch off the operating voltage.
2. Press all three setting elements simultaneously (UP/DOWN button and Edit button) and switch the operating voltage on again.

### D-2: Festo MS6-SFE-F5-P2U air mass flow standard conditions (Festo, 2009)